Electromagnetic Scattering by Lossy Plasmonic and Non-plasmonic Half-Spaces From Vertically Polarized Incident Waves

by

© Mohsen Eslami Nazari, B.Eng., M.Eng.

A thesis submitted to the
School of Graduate Studies
in partial fulfilment of the
requirements for the degree of
Doctor of Philosophy

Department of Electrical and Computer Engineering
Faculty of Engineering and Applied Science
Memorial University of Newfoundland

February 2023

St. John's Newfoundland

Abstract

In this research, approximate analytical solutions for the scattered electromagnetic (EM) fields radiated by a vertical electric dipole (VED) antenna in the presence of a lossy half-space for ordinary and plasmonic media are investigated. First, an approximate analytical solution for the wave scattering above a lossy half-space with a smooth interface is proposed for frequencies below the very high frequency (VHF) band. The solution to the problem is given in terms of two-dimensional Fourier transforms, which leads to Sommerfeld-type integrals. The solution is decomposed into three terms. Two terms are expressed with hyperbolic functions and the third term is presented using the Gauss error function. A numerical evaluation of the integrals validates the accuracy and efficiency of the proposed solution at various frequencies and distances from the source. Second, an approximate analytical solution of the problem with a smooth interface is proposed for frequencies below 10 GHz. The solution for the intermediate Hertz potential is decomposed into two integrals and a rigorous approximate closed-form solution in the near and far field regions is presented for each term. Then, the scattered electric field (E-field) components are calculated from the intermediate Hertz potential. A numerical evaluation of the solution for different lossy half-spaces, i.e., seawater, wet earth, dry earth and lake water, validates the accuracy of the proposed solution at various frequencies and distances from the antenna. Following this work, a new asymptotic solution for the scattered EM fields above a lossy half-space with a smooth interface for ordinary

and plasmonic media is proposed using the modified saddle point method. The new formulations are applied to calculate radiation patterns of different impedance half-planes for both ordinary media (e.g., seawater, silty clay soil, silty loam soil and lake water) and plasmonic media (e.g., silver and gold). A numerical evaluation of the proposed solution at various frequencies and comparisons with two alternative state-of-the-art solutions show that the proposed solution has higher accuracy for plasmonic and non-plasmonic structures. Lastly, random roughness is added to the interface, and a solution for EM scattering over a two-dimensional random rough surface with large roughness height using the generalized functions approach is proposed. The EM field derivation incorporates an arbitrary rough surface profile with small slope, a radiation source and involves all scattering orders of the scattered E-field for high and moderate contrast media. Subsequently, the first-order scattered E-field is calculated using the Neumann series solution for transverse magnetic (TM) polarization. By considering a pulsed dipole antenna and a two-dimensional Gaussian rough surface distribution with different root mean square heights and correlation lengths, the scattered E-field along with the radar cross-section is calculated. Using the result of the method of moments (MoM) as reference, a numerical evaluation of the solution for different roughness heights and contrast media demonstrates that the proposed solution is better than those of the small perturbation method (SPM), Kirchhoff approximation (KA) and small-slope approximation (SSA).

Acknowledgments

I wish to thank the Faculty of Engineering and Applied Science for offering me the opportunity to conduct this work, particularly the supervision of Dr. Weimin Huang and his help through this work are greatly appreciated. Moreover, I would like to express my gratitude to my supervisory committee members, Dr. Cecilia Moloney and Dr. Peter McGuire, due to their valuable suggestions and comments on my research.

I am grateful for the financial support in the form of the Natural Sciences and Engineering Research Council of Canada Discovery Grants (NRGPIN-2017-04508 and RGPAS-2017-507962).

I would like to thank all members of the Radar Remote Sensing Group for their advice in improving my research. Also, I have to thank my parents for their love and support throughout my life. Thank you both for giving me strength to reach the stars and chase my dreams. Finally, I wish to thank my wife, who has stood by me through all my travails. This work could not be completed without her support.

Contents

List of Tables

List of Figures

Table of Symbols

η :	Complex refractive index (p.6)
ρ :	Horizontal distance between the source and the observation point (p.6)
$\xi(x, y)$:	Surface deviation (p.10)
k :	Wavenumber (p.10)
∇ :	Vector differential operator (p. 11)
$\vec{E}$:	Electric field vector (p.11)
λ :	Wavelength (p.11)
R_c :	Radius of curvature (p.11)
$h(\cdot.)$:	Heaviside function (p.19)
ϵ :	Permittivity (p.20)
μ :	Permeability (p.20)
σ :	Conductivity (p.20)
ρ_v :	Charge density (p.21)
ω :	Angular frequency (p.21)

$\vec{D}$: Electric flux density (p.21)

$\vec{J}_c$: Conduction current (p.21)

$\vec{J}_s$: Source current (p.21)

$\vec{H}$: Magnetic field vector (p.21)

$\vec{B}$: Magnetic flux density (p.21)

z_p : z coordinate of the observation point (p.25)

γ' : Propagation constant (p.25)

$\delta(\cdot)$: Dirac delta function (p.25)

I : Current source (p.25)

Δl : Length of the antenna (p.25)

Π_z : Intermediate Hertz potential (p.27)

$J_0(\cdot)$: Zero order Bessel function (p.29)

$H_0^1(\cdot)$: Hankel function of the first kind (p.30)

$H_0^2(\cdot)$: Hankel function of the second kind (p.30)

erfc : Complementary error function (p.35)

χ : Reference value in the accuracy calculation (p.36)

$\hat{\chi}$: Calculated value in accuracy calculation (p.36)

n : Number of reference or calculated values in the accuracy calculation (p.36)

$\bar{\chi}$: Mean value of the reference values in the accuracy calculation (p.36)

$\tan\delta$: Loss tangent (p.46)

$H_0(\cdot)$: Struve function (p.48)

$Y_0(\cdot)$: Zero order Bessel function of second kind (Neuman function) (p.48)

erf : Gauss error function (p.56)

Δ : Surface impedance (p.102)

F_{xy} : Spatial Fourier transform (p.102)

$\vec{n}$: Normal vector of the surface (p.102)

$\vec{E}_t$: Tangential component of the E-field (p.102)

$\vec{E}_n$: Normal component of the E-field (p.102)

A : Arbitrary surface height factor (p.103)

N : Normal projection operator (p.103)

T : Tangential propagation operator (p.103)

$\vec{E}_s$: Electric field radiated by the source (p.104)

G_0 : Green's function solution of the Helmholtz equation in the free space (p.104)

Λ : Arbitrary height factor (p.104)

$F(\cdot)$: Sommerfeld attenuation function (p.104)

J : Jacobian determinant (p.117)

H : Hessian matrix (p.118)

c : Free space speed of light (p.124)

η_0 : Intrinsic impedance of the vacuum (p.125)

τ_0 : Pulse width (p.126)

A_r : Effective aperture of the receiving antenna (p.134)

G_r : Gain of receiving antenna (p.134)

List of Acronyms

FDTD:	Finite-difference time-domain (p.4)
FEM:	Finite element method (p.4)
GPR:	Ground penetrating radar (p.4)
E-field:	Electric field (p.4)
SIs:	Sommerfeld Integrals (p.5)
VED:	Vertical electric dipole (p.8)
HF:	High frequency (p.8)
SPM:	Small perturbation method (p.10)
RMS:	Root mean square (p.10)
KA:	Kirchhoff approximation (p.11)
SSA:	Small slope approximation (p.12)
FDM:	Finite difference method (p.12)
MoM:	Method of moments (p.12)
VHF:	Very high frequency (p.14)
H-field:	Magnetic field (p.17)

ACES: Applied Computational Electromagnetics Society Symposium (p.17)

NRMSE: Normalized root-mean-square error (p.35)

RMSE: Root-mean-square error (p.35)

NMAE: Normalized maximum absolute error (p.77)

LHS: Left-hand side (p.103)

RHS: Right-hand side (p.104)

PDF: probability density function (p.137)

SNR: signal-to-noise ratio (p.139)

TM: Transverse mode (p.139)

AIEM: advanced integral equation method (p.149)

Chapter 1

Introduction

The propagation, absorption and scattering of electromagnetic (EM) waves provide potential tools for exploring different media, such as the surface of the ocean and soil media. These phenomena have been important in the design and use of various systems and devices, such as radar, sonar, altimeter and radio communication links. EM scattering incorporates wave refraction, reflection, diffraction and absorption, while the development of EM scattering essentially depends on mathematical modeling and analysis of wave phenomena [1]. Generally, EM field theories are expressed in terms of partial differential equations along with boundary conditions. The method of Green's function [2] is utilized to represent scattered EM fields in the integral form depending on the unknown field, which can be within or on the scatterers. EM scattering from a surface is a complex process depending on two surface parameters including the dielectric properties of the surface (i.e., relative permittivity and conductivity) and its

geometric structure. In scattering from surfaces, two main phenomena are identified: diffuse reflection and specular reflection. Depending on their varying proportions on the observed surface type, the combination of these two phenomena should be considered in the scattering process. For specular reflection, EM waves transmitted in one direction with a specific energy E_1 are reflected in another direction with a slightly lower energy E_2 due to absorption by the surface. On the other hand, the diffuse reflection is the reflection of the EM wave in different directions with different energies. The proportion of these two phenomena in the scattering process is determined by dielectric properties and roughness of the surface. In this study, plasmonic and non-plasmonic half-spaces with and without roughness are considered and the scattered fields are derived by assuming vertically polarized incident waves at different frequencies and distances from the antenna, i.e., in the near and far field regions. The proposed solutions are compared with numerical and state of the art solutions for different material constitutions, various frequencies and distances from the antenna.

1.1 Research Rationale

The scattering of EM waves is the process of re-radiation of an incident wave by a material body. The incident wave may change its type (e.g., from plane to spherical or cylindrical), the direction of propagation, amplitude, phase, and polarization state. EM fields scattered by an object incorporate information regarding geometric and material properties of the scatterer along with its position, orientation and

speed. Remote sensing technologies use this information to survey, explore, and study remotely and non-destructively the space and material objects surrounding an observer. It is essential to know the way that EM waves interact with the targets and are scattered from them in order to extract the information encoded in the scattered fields. The wave nature of EM fields is determined by various scattering effects such as penetration, absorption, reflection, resonance and so forth. In general, these wave phenomena cannot be comprehended and modeled in the framework of simple ray optical constructions.

EM scattering theory, as a branch of electromagnetics, describes, explains, and predicts EM field behavior in the presence of material obstacles. EM theory is still in the process of development motivated by different insights arising from different contexts and applications, from radar and remote sensing technologies to metamaterials and plasmonics in photonics and nanoscience [3]. The physics of EM scattering can be studied by the solutions of Maxwell's equations, while exact analytical solutions are relatively difficult to acquire. A closed-form solution is only obtainable for simply shaped scatterers, i.e., planar infinite interfaces of homogeneous materials, spheres, cones, wedges and cylinders, with simple materials, such as a perfect electric conductor. These closed-form solutions provide important information about radiation, propagation, diffraction and scattering of EM waves and can be used to explain and forecast the behavior of the fields. Recent advances in computational technologies have empowered researchers to use numerical methods, such as the finite-difference

time-domain method (FDTD) and the finite element method (FEM), to represent the behavior of the scattered fields. However, numerical approaches have fundamental limitations. First, calculation of scattered fields for objects larger than a dozen wavelengths leads to systems of equations with millions of unknowns, which are difficult to evaluate due to unrealistic runtime and memory requirements. Second, numerical solutions may not be able to provide physical insights regarding the mechanism of the scattering. Therefore, there is a continuing need for the development of approximate and asymptotic solutions for EM scattering scenarios.

In this research, one of the common EM scattering problems, which is called the Sommerfeld problem, is reconsidered for smooth and rough interfaces due to its application in remote sensing [1, 4], ground penetrating radar (GPR) [5], near field optics [6], terahertz (THz) devices [7], and plasmonic/nanophotonic applications [8, 9]. In earth sciences, GPR is utilized to study soils, bedrock, groundwater and ice [10]. GPR electromagnetic wave propagation can be modeled by the Sommerfeld problem with smooth and rough interfaces, and then material constitution can be characterized from the scattered fields [11]. In remote sensing applications, the scattered fields over natural targets (e.g., ocean surface, sea ice, vegetation and earth) are analyzed to detect and monitor their physical characteristics, while the backscattered fields can be obtained through the Sommerfeld problem [12]. For instance, the backscattered electric field (E-field) from the ocean surface or sea ice can be acquired by modeling the scattering surface as a two-dimensional random rough surface. In near-field

optics, the goal is to increase the optical resolution beyond the diffraction limit. In order to model the light scattering mechanism and limitations of near-field optics, an arbitrarily oriented dipole antenna as an elementary light source is considered above a half-space and the light scattering can be modeled using the Sommerfeld problem [6].

In this thesis, various approximate closed-form solutions for the Sommerfeld problem with smooth and rough interfaces at various frequencies, distances from the antenna (near and far field regions) and material constitutions are proposed.

1.2 Literature Review

To develop detection or inversion techniques in the study of EM wave scattering, interaction of EM waves with smooth and rough surfaces is required. Many researchers have attempted to present approximate solutions for the scattered fields over smooth and rough surfaces [13–18].

1.2.1 EM Scattering Over Smooth Surfaces

The problem of EM scattering from lossy half-spaces has been the subject of numerous studies since 1909. Sommerfeld presented the first rigorous solution of the EM field of a vertical Hertzian dipole in the presence of a lossy ground [19]. The proposed solution contains improper integrals commonly with a Bessel function kernel, referred to as Sommerfeld integrals (SIs) and cannot be evaluated in closed form due

to the oscillatory and slowly decaying integrand, as well as various singularities on the integration path of the integrands. He deformed the integration path of the Fourier-Bessel transform around the fundamental branch cuts and the pole of the integrand to convert the axial-transmission form of the solution to the radial-transmission form associated with the cylindrical Zennek surface wave [20] playing a considerable role in long-distance EM field propagation on the half-space interface. He also presented an asymptotic closed-form expression for the term associated with the Zenneck surface wave in the Hertz vector using the error function of a complex argument called numerical distance. Subsequently, this problem was reconsidered by Wise [21] and Van Der Pol [22], and their independent solutions for the Hertz vector were in agreement with the Sommerfeld solution for high media contrast (i.e., $|\eta^2| \gg 1$, where η is the complex refractive index) and far field regions near the interface of regions (i.e., $k_0\rho \gg 1$ and $z/\rho \ll 1$, wherein k_0 represents the free-space wavenumber, z denotes the z coordinate of the observation point and ρ is the horizontal distance between the source and the observation point). Another important milestone in the development of scattered EM fields over lossy half-spaces was the surface wave formula derived by Norton [23] and Wait [24], which was based on the work of Wise [21] and is referred to as the Norton surface wave or the Sommerfeld-Norton groundwave formula, and is valid for an arbitrary height of transmitter or receiver. However, in this formulation, Norton's numerical distance parameter was not quite accurate, particularly for field points away from the interface due to premature truncation of a binomial expansion

of a square root in the derivation of the solution. Subsequently, Bannister [25] extended Norton's far-field equations to the quasi-near-field region, while an inaccurate Norton's numerical distance parameter was adopted.

The saddle point method of integration is an asymptotic technique applied to evaluate SIs when the distance between the source and the observation point is large. However, for a highly lossy surface, the integrand poles are close to the saddle point and their contributions cannot be separated. Thus, Van Der Waerden [26] introduced the modified saddle point method by considering the presence of the poles near the saddle point, and then the proposed method was applied to the Sommerfeld problem by Bernard and Ishimaru [27] and Collin [28]. The obtained solutions, which considered higher order terms (i.e., lateral wave), were consistent with the Norton surface wave formulation for highly conductive and far-field regions near the interface.

Wait [29, 30] and King and Schlak [31] studied the effect of a layered ground in the Sommerfeld problem, where the surface impedance becomes inductive. In this problem, the Zenneck wave evolves into a trapped surface wave contributing to the asymptotic ground-wave solution. An integral formulation using the surface impedance concept and the compensation theorem were applied to the Sommerfeld problem by King [32] and Green [33]. In their formulations, the auxiliary Hertz vector was employed for obtaining the scattered field components, while only the terms of order r^{-1} were retained. It should be noted that the numerical distance parameter employed in this method was similar to Norton's numerical distance. The most recent

approximate solution of the Sommerfeld problem was proposed by King and Sandler [34–36], which is valid for high contrast media with refractive index of $|\eta^2| \geqslant 9$ (e.g., ocean surface in the high frequency (HF) band) and is hereinafter referred to as the King solution. By a simple modification in the presented numerical distance in [34, 35], the formulation is capable of calculating the scattered electric field components in the presence of a thin dielectric overlayer. The King approach is relatively similar to previous methods of Sommerfeld and Norton, while his formulation is based on the real-axis integral representation of the scattered electric and magnetic fields rather than the Hertz vector. Furthermore, instead of the error function used by Norton and Wait, he used the Fresnel integral. However, it was indicated by Collin [37] and Mahmoud et al. [38] that the solutions for EM fields excited by a vertical electric dipole (VED) in the presence of lossy or dielectric coated half-space were not quite accurate due to the trapped surface wave. Therefore, this classical problem was revisited by several researchers over the past several years [14, 15, 36, 39, 40]. Sarabandi et al. [41] introduced an analytical method for calculating SIs in the near-field and far-field regions based on the reflection coefficient approximation of integrands using the Prony method. Although this method can estimate the value of the integral in the near-field and far-field regions, its accuracy is limited due to the number of image points when the source and observation points are located near the surface.

In order to evaluate the Sommerfeld-type integrals numerically, several techniques have been proposed. Parhami et al. [42] deformed the path of integration to the steep-

est descent path, and computed the SIs numerically when the distance between image and observation is large. Michalski [43] improved Parhami's method by proposing a variation over the branch cut. Subsequently, Johnson and Dudley [44] proposed a numerical method valid for small distances between the observation and the image, in which the integration is performed after removing singularities along the real axis. Lindell and Alanen [45] proposed an interesting approach called exact image theory to rectify the difficulty in the calculation of SIs by modifying the Sommerfeld integrand to a convenient form for numerical purposes. Although the convergence properties of the SIs have been improved by employing these numerical techniques, the computational cost of numerical evaluation is high. Further, they are not valid for the general source and observation point locations and arbitrary electrical properties of a lossy half-space [41].

In this thesis, the classical Sommerfeld half-space problem is reconsidered and rigorous approximate closed-form solutions for the intermediate Hertz potential and the scattered fields are presented for general source and observation point locations as well as good dielectric and conductor media. The theoretical development is validated by representative numerical results and compared with alternative state of the art solutions for ordinary and plasmonic media.

1.2.2 EM Scattering by Random Rough Surfaces

Over the past six decades, the problem of EM scattering from rough surfaces has been the subject of extensive investigation due to its application in sonar, optics, astronomy, medical imaging and remote sensing of the environment [1] including radar remote sensing of the oceans [4, 46], mine detection [47] and soil moisture measurement [48].

In the study of electromagnetics, wave scattering from natural targets such as sea ice, vegetation, soil and ocean surface can be modeled as a three-dimensional random rough surface scattering problem (the third dimension is the height of each point in the 2D plane) and valuable information, such as physical characteristics, can be extracted from the scattered fields. However, an exact analytical solution for EM scattering by random rough surfaces does not exist [13] and many researchers have attempted to present approximate closed-form solutions for the scattered fields [13, 16–18]. Different approximate solutions have been presented by researchers for calculating the scattered E-field over rough surfaces with different roughness characteristics. The small perturbation method (SPM) is one of the most common methods for the calculation of scattered fields for surfaces with small root mean square (RMS) height and slope. Rayleigh [49] presented the perturbation scattering theory by considering acoustic scattering from corrugated surfaces with sinusoidal profile. This method is applicable for slightly rough surfaces where the product of the incident wavenumber (k) and surface deviation, $\xi(x, y)$, from the mean is much less than unity (i.e., $k\xi \ll 1$). Afterwards, Rice [50] presented an extensive methodology for EM wave

scattering from two-dimensional slightly rough surfaces with small slopes, for which the surface derivatives are much less than one (i.e., $\xi_x, \xi_y \ll 1$), using the perturbation method. The surface roughness was represented by expanding a periodic rough surface into a Fourier series with independent random coefficients, and scattered E-field components were calculated by applying the divergence relation ($\nabla \cdot \vec{E} = 0$) and boundary conditions to the E-field series form. Later, Wait [51] calculated the scattered fields from a two-dimensional rough surface along with the effective normalized surface impedance for the case of specular reflection for a vertically polarized incident wave using the perturbation technique. Subsequently, the SPM method was developed for time-varying rough sea surfaces [52], homogeneous dielectric [53] and inhomogeneous dielectric [54] rough surfaces. However, the main constraint in using the SPM is the small height assumption in the derivation of the scattered E-field.

The other method for calculating scattered fields is the Kirchhoff approximation (KA) (i.e., tangent approximation or physical optics approximation) based on the Stratton–Chu integral equations [55, 56]. This method is valid if the radius of curvature (R_c) on the rough surface is much greater than the wavelength (λ) of the incident wave (i.e., $R_c \gg \lambda$). In this method, the dependence of the scattered field on the surface slope is indicated as functions of the Fresnel coefficients. Kodis [57] used the physical optics approach to calculate the radar cross-section of a highly conductive rough time-invariant surface, while the stationary phase method was used for evaluating the scattered field integrals. Afterwards, Barrick [58] extended Kodis's analysis

to the bistatic configuration and finite conductive and time-varying rough surfaces, particularly for the sea surface [59]. The small slope approximation (SSA) is another scattering model making a bridge between the KA and the SPM in order to broaden its validity region incorporating the SPM and KA validity domains. By using the SPM kernels, the scattering amplitude of the first-order SSA can be acquired [60].

Monte Carlo simulation is an alternative approach for finding the scattered field and its statistics over rough surfaces. Several sample rough surfaces are generated first with defined roughness distribution, and then the scattered field for each sample surface is acquired by a numerical method, such as the finite difference method (FDM) [61, 62], the FEM [63, 64] and the method of moments (MoM) [60]. However, the required memory and the computation time are the main constraints in computing scattered fields.

The fundamental analysis of scattered fields in this dissertation is based on a decomposition of surface characteristics and electromagnetic field components employing Heaviside functions imposed by the various scattering regions. Scattered EM fields are derived directly from the point form of Maxwell's equations, while the boundary conditions are evolved naturally from the beginning of the formulations. Two integral equations associated with above and below the scatter are generated, and then the Neumann series solution is used for obtaining scattered fields with different orders. Final equations directly relate the scattered field to the arbitrary source field without employing the intermediate Hertz potential. This approach was initially proposed

by Walsh [65] for the study of rough surface scattering using mathematical distributions known as generalized functions. The method was later developed for two-body scattering [66], horizontally stratified media [67] and surface propagation for periodic rough surfaces [68]. Subsequently, Walsh and Gill [69] developed the formulations for highly conductive rough surfaces with arbitrary profiles while the small height and small slope assumptions were considered in the EM field derivations. As the surface height grows beyond the small height limitation, the scattered field expressions lose their validity in this method. Silva et al. [46, 70] proposed new formulations for the scattering of ocean surfaces with large roughness scales in the HF frequency band. They derived the radar cross-section for the ocean surfaces (highly conductive) with different significant wave heights at grazing angle with and without correction terms. However, their formulations are not applicable to the case of different incident angles and moderate contrast media, while the roughness height is large. Also, the validation of the results has not been made using a numerical method.

In this thesis, the EM wave scattering formulations are developed for a time-invariant random rough surface with large roughness heights and different contrast media, and the normal component of the scattered electric field is obtained in the form of a Fredholm integral equation. With a monostatic configuration, the field equations are developed for a pulsed radar, and then the first-order scattered E-field and the radar cross-section at different incident angles are derived.

1.3 The Scope of the Thesis

This thesis focuses on proposing analytical solutions for the scattered EM fields over smooth and rough surfaces in the presence of a VED at different frequencies and distances from the antenna in the near and far field regions. The outline of this thesis is as follows.

In Chapter 2, the intermediate Hertz potential and scattered fields are derived in the presence of a VED over a lossy half-space with a smooth interface. The intermediate Hertz potential is decomposed into three terms and approximate solutions are proposed for each term below the very high frequency (VHF) band. The developed formulation for the intermediate Hertz potential is assessed by comparing it with the conventional [36, 71] and numerical solutions.

In Chapter 3, by decomposing the Sommerfeld integral into two integrals and using proper near and far field approximations, the intermediate Hertz potential and scattered electric field components over a lossy half-space with a smooth interface are acquired at various frequencies (up to 10 GHz) and distances from the antenna in the near and far field regions. The theoretical developments for the intermediate Hertz potential and scattered electric field are compared with two alternative state of the art solutions referred to as the King [36] and the Norton-Bannister [25] solutions for different media characteristics and various frequencies and distances from the antenna in the near and far field regions.

In Chapter 4, the scattered electric and magnetic field components are obtained above a lossy half-space with a smooth interface using the modified saddle-point method for both ordinary and plasmonic media in a wide frequency range, i.e., 100 MHz to 100 GHz for non-plasmonic and 300 THz to 900 THz for plasmonic media in far field regions. The developed formulations for the scattered electric and magnetic field components are validated by representative numerical results and compared with the King and the Norton-Bannister solutions for ordinary and plasmonic media.

In Chapter 5, time-invariant random roughness is added to the interface and scattered fields over a two-dimensional random rough surface with large roughness heights and different contrast media are calculated. The scattered electric field is derived from a general operator equation for the Neumann boundary conditions, which results in an integral equation containing the normal component of the scattered electric field. By using the Neumann series solution and considering a Fourier series representation of the scattering surface, a general series solution is derived. By considering a monostatic configuration, the scattered electric field formulation is developed for a pulsed radar. Then, the first-order scattered electric field along with radar cross-section is calculated for different contrast media and roughness heights. The theoretical development is validated by the MoM [60] as a numerical reference solution and compared with the widely accepted SPM [50] and KA [72] solutions.

In Chapter 6, a summary of the fundamental conclusions obtained from the research in this thesis is given. Moreover, several suggestions for future work are pro-

posed.

The research results presented in this thesis have been published in four refereed journal and two conference papers as listed below:

1. M. E. Nazari and W. Huang, "An analytical solution of electromagnetic radiation of a vertical dipole over a layered half-space," IEEE Trans. Antennas Propag., vol. 68, no. 2, pp. 1181-1185, 2020.

   This journal paper provides the development of the scattered E-field over a lossy half-space for frequencies below VHF band (Section 2.2 and Section 2.3).

2. M. E. Nazari and W. Huang, "An analytical solution of the electric field excited by a vertical electric dipole above a lossy half-space: From radio to microwave frequencies," IEEE Trans. Antennas Propag., vol. 68, no. 11, pp. 7517-7529, 2020.

   This journal paper proposes the development of the scattered E-field over a lossy half-space at different frequencies (below 10 GHz) and distances from the antenna in the near and far field regions (Chapter 3).

3. M. E. Nazari and W. Huang, "An analytical solution of the electric field radiated by a dipole over a layered half-space," 2020 IEEE International Symposium on Antennas and Propagation and North American Radio Science Meeting, vol. 68, no. 11, pp. 943-944, 2020.

   This conference paper proposes the development of the scattered E-field over a lossy half-space below 10 GHz in the near and far field regions (Chapter 3).

4. M. E. Nazari, W. Huang, "Asymptotic solution for the electromagnetic scattering of a vertical dipole over plasmonic and non-plasmonic half-spaces," IET Microw. Antennas Propag., vol. 15, no. 7, pp. 704-717, 2021.

   This journal paper presents the development of the scattered E- and H-field over a lossy half-space with extensions to plasmonics (Chapter 4).

5. M. E. Nazari and W. Huang, "EM wave scattering by random surfaces with different contrast and large roughness heights," IEEE J. Multiscale Multiphys. Comput. Tech., vol. 7, pp. 252-267, 2022.

   This journal paper provides the development of the scattered E-field and the radar cross-section from random rough surfaces with different contrast and large roughness heights (Chapter 5).

6. M. E. Nazari and W. Huang, "Scattering of EM waves from random surfaces with different contrast and surface roughness," 2021 International Applied Computational Electromagnetics Society Symposium (ACES), pp. 1-3, 2021.

   This conference paper provides the development of the scattered E-field and the radar cross-section from random rough surfaces with low and moderate contrasts and different roughness heights (Chapter 5).

Chapter 2

Intermediate Hertz Potential Calculation for Frequencies Below the VHF Band

In this chapter[1], the classical Sommerfeld half-space problem with a smooth interface is revisited and the formal solution presented by Walsh and Donnelly [66] is utilized for calculating electric field intensity when the source is a vertical dipole. New approximations for the electric field integral equations are proposed to achieve a rigorous approximate closed-form solution for the scattered electric fields for frequencies be-

[1]The content of this chapter is based on the following publication:
M. E. Nazari and W. Huang, "An analytical solution of electromagnetic radiation of a vertical dipole over a layered half-space," IEEE Trans. Antennas Propag., vol. 68, no. 2, pp. 1181-1185, 2020.
This paper provides the development of the scattered E-field over a lossy half-space for frequencies below the VHF band (Section 2.2 and Section 2.3).
Roles: Mr. Nazari conducted this research under the guidance of Dr. Huang and acted as the first author of the manuscript. All the contents of this paper were written by Mr. Nazari and further refined by Dr. Huang.

low VHF band. It is shown that the proposed solution solution is not only effective for the far field, but also justifiable near the antenna. The theoretical development is validated by the representative numerical results, and is also compared with the widely accepted approximation presented in [36, 71].

This chapter is organized as follows. In Section 2.1, theoretical analysis and formulation of the problem are presented. In Section 2.2, the formulations of the scattered electric field above a lossy half-space in the presence of a vertical dipole antenna are introduced. In Section 2.2.1, each term of the approximate closed-form solution for the scattering problem is presented. In Section 2.3, the solution obtained in Section 2.2.1 is assessed at various frequencies for the near and far field regions and is implemented for the particular case of ocean surface scattering in the HF frequency band.

2.1 Theoretical Analysis and Formulation of the Problem

In this section, a detailed analysis of the two-body model with different electrical properties, as shown in Fig. 2.1, is reviewed and scattered fields are represented using the generalized functions approach [73]. Subsequently, the scattered E-field expression for a lossy half-space is derived from the general scattered E-field expression obtained from the analysis of the two-body model. With the aid of two Heaviside functions as

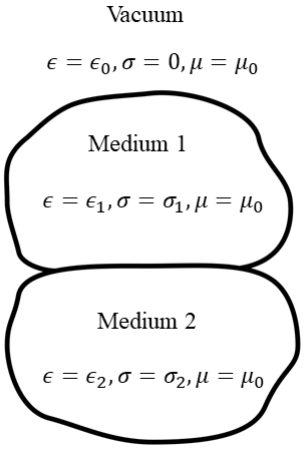

Fig. 2.1: Cross section of the 3D physical geometry for the two-body model.

$$h_{M_1} = \begin{cases} 1, & (x,y,z) \in M_1 \\ \\ 0, & \text{otherwise} \end{cases}, \quad h_{M_2} = \begin{cases} 1, & (x,y,z) \in M_2 \\ \\ 0, & \text{otherwise} \end{cases}, \tag{2.1}$$

the electrical properties of the entire space can be represented as

$$\epsilon_t = h_{M_1}\epsilon_1 + h_{M_2}\epsilon_2 + (1 - h_{M_1})(1 - h_{M_2})\epsilon_0 \tag{2.2}$$

$$\sigma_t = h_{M_1}\sigma_1 + h_{M_2}\sigma_2 \tag{2.3}$$

in which M_1 and M_2 denote Medium 1 and Medium 2, respectively, in Fig. 2.1. Also, ϵ_i, μ_i and σ_i represent permittivity, permeability and conductivity of each medium, i, respectively. In the entire space, the point form of Maxwell's equations for the electric

($\vec{E}$) and magnetic ($\vec{H}$) fields in the frequency domain can be expressed as

$$\nabla \times \vec{E} = -j\omega\mu_0\vec{H}, \tag{2.4}$$

$$\nabla \times \vec{H} = j\omega\vec{D} + \vec{J}_c + \vec{J}_s, \tag{2.5}$$

and

$$\nabla \cdot \vec{D} = \rho_v,\ \nabla \cdot \vec{B} = 0 \tag{2.6}$$

where $\vec{J}_c$ represents the conduction current, $\vec{J}_s$ denotes the source current out of media 1 and 2, ρ_v denotes the volumetric charge density, ω is the angular frequency, $\vec{D}$ is the electric flux density and $\vec{B}$ represents the magnetic flux density. Using (2.2) and (2.3), the conduction current and the electric flux density in the entire space may be expressed as

$$\vec{J}_c = \sigma_t\vec{E} = h_{M_1}\sigma_1\vec{E} + h_{M_2}\sigma_2\vec{E} \tag{2.7}$$

and

$$\vec{D} = \epsilon_t\vec{E} = h_{M_1}\epsilon_1\vec{E} + h_{M_2}\epsilon_2\vec{E} + (1 - h_{M_1})(1 - h_{M_2})\epsilon_0\vec{E}. \tag{2.8}$$

By substituting (2.7) and (2.8) into (2.5), (2.5) can be written as

$$\nabla \times \vec{H} = j\omega\epsilon_0\eta_0^2\vec{E} + \vec{J}_s \tag{2.9}$$

wherein the refractive index η_0 is defined by

$$\eta_0 \equiv \left[\frac{\epsilon_t}{\epsilon_0} + \frac{\sigma_t}{j\omega\epsilon_0}\right]^{1/2} = \left[\eta_{01}^2 h_{M_1} + \eta_{02}^2 h_{M_2} + (1-h_{M_1})(1-h_{M_2})\right]^{1/2} \tag{2.10}$$

in which η_{01} and η_{02} are the refractive index in Medium 1 and Medium 2, respectively, and can be expressed as

$$\eta_{01} = \left[\frac{\epsilon_1}{\epsilon_0} + \frac{\sigma_1}{j\omega\epsilon_0}\right]^{1/2},\ \eta_{02} = \left[\frac{\epsilon_2}{\epsilon_0} + \frac{\sigma_2}{j\omega\epsilon_0}\right]^{1/2}. \tag{2.11}$$

By applying the curl operator to both sides of (2.4) and using (2.9) for the right hand side of the obtained equation, the Helmholtz equation for this problem can be obtained as

$$\nabla^2\vec{E} + k_0^2\eta_0^2\vec{E} = \nabla(\nabla\cdot\vec{E}) + j\omega\mu_0\vec{J}_s \tag{2.12}$$

wherein k_0 is the wavenumber in free space. Now, we need to find an expression for the divergence of the E-field in (2.12). By taking the divergence of (2.9), we have

$$\nabla\cdot(\eta_0^2\vec{E}) = -\frac{1}{j\omega\epsilon_0}\nabla\cdot\vec{J}_s. \tag{2.13}$$

By taking the divergence of $\eta_0^2\vec{E}$ and using (2.10), the left hand side of (2.13) becomes

$$\begin{aligned}\nabla\cdot(\eta_0^2\vec{E}) =& (1-h_{M_1})(1-h_{M_2})\nabla\cdot\vec{E} + \eta_{01}^2 h_{M_1}\nabla\cdot\vec{E} + \eta_{02}^2 h_{M_2}\nabla\cdot\vec{E} \\ &+ \eta_{01}^2\vec{E}^{1-}\cdot\nabla h_{M_1} + \eta_{02}^2\vec{E}^{2-}\cdot\nabla h_{M_2} - \vec{E}^{1+}\cdot\nabla h_{M_1} - \vec{E}^{2+}\cdot\nabla h_{M_2}\end{aligned} \tag{2.14}$$

wherein the subscript $1-$ and $2-$ indicate the E-field within the boundary of Medium 1 and Medium 2, respectively. Similarly, $1+$ and $2+$ represent the E-field outside of Medium 1 and Medium 2 on the boundary area. By inserting (2.14) into (2.13) we have

$$\begin{aligned}
&h_{M_1}\nabla\cdot\vec{E}=0,\ h_{M_2}\nabla\cdot\vec{E}=0,\ (1-h_{M_1})(1-h_{M_2})\nabla\cdot\vec{E}=-\frac{1}{j\omega\epsilon_0}\nabla\cdot\vec{J}_s\\
&\left(\eta_{01}^2\vec{E}^{1-}-\vec{E}^{1+}\right)\cdot\nabla h_{M_1}\Big|_{R_1}=0,\ \left(\eta_{02}^2\vec{E}^{2-}-\vec{E}^{2+}\right)\cdot\nabla h_{M_2}\Big|_{R_2}=0\\
&\eta_{01}^2\vec{E}^{1-}\cdot\nabla h_{M_1}\Big|_{R_{12}}+\eta_{02}^2\vec{E}^{2-}\cdot\nabla h_{M_2}\Big|_{R_{12}}=0
\end{aligned}\tag{2.15}$$

where R_1 illustrates the restriction of the expression to the boundary between region M_1 and the vacuum and the same definition is provided for R_2. R_{12} denotes the the boundary between region M_1 and M_2. It should be noted that the boundary conditions are provided by the last three equations of (2.15). The E-field for different regions can also be expressed as

$$\vec{E}=h_{M_1}\vec{E}+h_{M_2}\vec{E}+(1-h_{M_1})(1-h_{M_2})\vec{E}.\tag{2.16}$$

Moreover, the divergence of $\vec{E}$ with the use of the fact that $\nabla h_{M_1}\Big|_{R_{12}} = -\nabla h_{M_2}\Big|_{R_{12}}$ becomes

$$\begin{aligned}\nabla \cdot \vec{E} =& h_{M_1}\nabla \cdot \vec{E} + h_{M_2}\nabla \cdot \vec{E} + (1-h_{M_1})(1-h_{M_2})\nabla \cdot \vec{E} + \left(\vec{E}^{1-} - \vec{E}^{1+}\right) \cdot \nabla h_{M_1}\Big|_{R_1} \\ &+ \left(\vec{E}^{2-} - \vec{E}^{2+}\right) \cdot \nabla h_{M_2}\Big|_{R_2} + \left(\vec{E}^{1-} - \vec{E}^{2-}\right) \cdot \nabla h_{M_1}\Big|_{R_{12}}.\end{aligned} \tag{2.17}$$

Now, by substituting (2.15) into (2.17) and replacing the negative superscript quantities with the positive ones, or vice versa, the divergence of the E-field can be acquired as

$$\begin{aligned}\nabla \cdot \vec{E} =& -\frac{1}{j\omega\epsilon_0}\nabla \cdot \vec{J}_s + \left(\frac{1}{\eta_{01}^2} - 1\right) \vec{E}^{1+} \cdot \nabla h_{M_1}\Big|_{R_1} + \left(\frac{1}{\eta_{02}^2} - 1\right) \vec{E}^{2+} \cdot \nabla h_{M_2}\Big|_{R_2} \\ &+ \left(\vec{E}^{1-} - \vec{E}^{2-}\right) \cdot \nabla h_{M_1}\Big|_{R_{12}}.\end{aligned} \tag{2.18}$$

By inserting the divergence of the E-field obtained from the last equation into (2.12), the Helmholtz equation becomes

$$\begin{aligned}\nabla^2\vec{E} + k_0^2\eta_0^2\vec{E} = -T_{SE}(\vec{J}_s) &+ \nabla\left(\vec{E}^{1+} \cdot \nabla h_{M_1}\Big|_{R_1}\right)\left(\frac{1}{\eta_{01}^2} - 1\right) \\ &+ \left(\frac{1}{\eta_{02}^2} - 1\right)\nabla\left(\vec{E}^{2+} \cdot \nabla h_{M_2}\Big|_{R_2}\right) + \nabla\left[\left(\vec{E}^{1-} - \vec{E}^{2-}\right) \cdot \nabla h_{M_1}\Big|_{R_{12}}\right]\end{aligned} \tag{2.19}$$

in which T_{SE} is the electrical source operator defined as

$$T_{SE}(\vec{J}_s) = \frac{1}{j\omega\epsilon_0}\left[\nabla(\nabla \cdot \vec{J}_s) + k_0^2\vec{J}_s\right]. \tag{2.20}$$

In order to find the scattered fields over a lossy half-space, the Heaviside function of Medium 1 and its gradient, respectively, can be written as $h_{M_1} = 1 - h(z)$ and $\nabla h_{M_1} = -\delta(z)\hat{z}$, while $h_{M_2} = 0$. Now, by using (2.15), (2.19) may be expressed as [66]

$$\nabla^2 \vec{E} + k_0^2 \eta_0^2 \vec{E} = -\left(\eta_{01}^2 - 1\right) \nabla \left[{E_z}^{1+} \delta(z)\right] + \left[\frac{\eta_{01}^2 - 1}{\eta_{01}^2}\right] \nabla \left[{E_z}^{z_p} \delta(z)\right] - T_{SE}(\vec{J}_s) \tag{2.21}$$

in which z_p represents the z coordinate of the observation point. On the other hand, the general form of the Green's function for each medium can be expressed as

$$G_m(x, y, z) = \frac{e^{-j\gamma'_m r}}{4\pi r}, m \in \{0, 1\} \tag{2.22}$$

wherein γ'_m denotes the propagation constant for each medium and can be written as $\gamma'_m = k_0 \eta_{0m}$ in which η_{0m} is calculated using (2.11) for different media. The source current when the source is a VED located at $(0, 0, h)$ in the Cartesian coordinate system above the lossy half-space can be given by

$$\vec{J}_s = I\Delta l \;\; \delta(x)\, \delta(y)\, \delta(z - h)\, \hat{z} \tag{2.23}$$

where I is the current source and Δl represents the length of the antenna. The Helmholtz equation along with the boundary conditions can be obtained by substituting (2.23) into (2.20) and then (2.21). Subsequently, the method of Green's

function is utilized to calculate the spatial Fourier transform of the scattered E-field components as

$$\underline{E_x} = \frac{I\Delta l}{\omega\epsilon_0} k_x \frac{\partial}{\partial z} \left[\frac{e^{-|z-h|\gamma_0}}{2\gamma_0} + \frac{e^{-(z+h)\gamma_0}}{2\gamma_0} \frac{\gamma_0 - \frac{1}{\eta_{01}^2}\sqrt{k^2 - \gamma_1'^2}}{\gamma_0 + \frac{1}{\eta_{01}^2}\sqrt{k^2 - \gamma_1'^2}} \right] \tag{2.24}$$

$$\underline{E_y} = \frac{I\Delta l}{\omega\epsilon_0} k_y \frac{\partial}{\partial z} \left[\frac{e^{-|z-h|\gamma_0}}{2\gamma_0} + \frac{e^{-(z+h)\gamma_0}}{2\gamma_0} \frac{\gamma_0 - \frac{1}{\eta_{01}^2}\sqrt{k^2 - \gamma_1'^2}}{\gamma_0 + \frac{1}{\eta_{01}^2}\sqrt{k^2 - \gamma_1'^2}} \right] \tag{2.25}$$

$$\underline{E_z} = \frac{I\Delta l}{j\omega\epsilon_0} \left(\frac{\partial^2}{\partial z^2} + k^2 \right) \frac{\partial}{\partial z} \left[\frac{e^{-|z-h|\gamma_0}}{2\gamma_0} + \frac{e^{-(z+h)\gamma_0}}{2\gamma_0} \frac{\gamma_0 - \frac{1}{\eta_{01}^2}\sqrt{k^2 - \gamma_1'^2}}{\gamma_0 + \frac{1}{\eta_{01}^2}\sqrt{k^2 - \gamma_1'^2}} \right] \tag{2.26}$$

in which $k^2 = k_x^2 + k_y^2$ (K_x and k_y are spatial frequency domain) and a bar beneath a quantity denotes its two-dimensional Fourier transform. The scattered magnetic field components can also be calculated by substituting (2.24)-(2.26) into (2.4). In the next section, we attempt to find approximate closed-form solutions for the scattered fields over a lossy half-space in the presence of a VED for different frequencies and distances from the antenna.

2.2 Scattered E-field Calculation

In this section, the scattered fields above a lossy half-space is obtained when the source is taken to be a VED located at $(0, 0, h)$ in the Cartesian coordinate system above the lossy half-space, as shown in Fig. 2.2. By applying an inverse two dimensional

Fourier transform to (2.24)-(2.26), scattered E-field components can be obtained as [16]

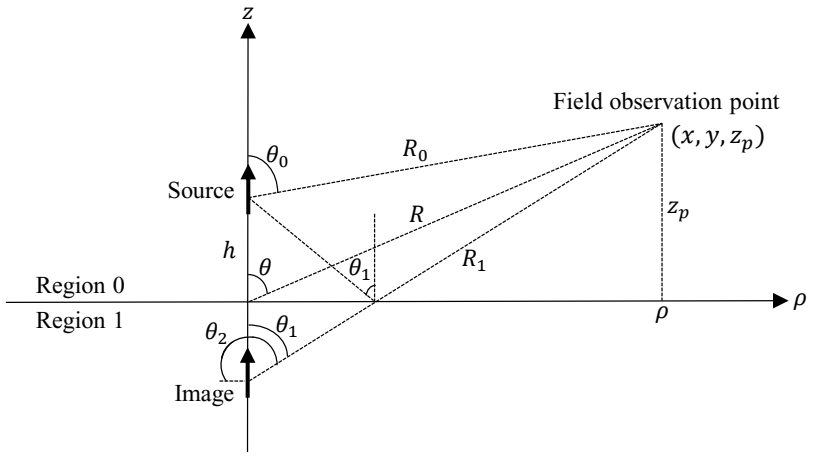

Fig. 2.2: Dipole source above a lossy half-space.

$$\vec{E} = \frac{I\Delta l}{j\omega\epsilon_0}\left[\frac{\partial^2\Pi_z}{\partial x\partial z}\,\hat{x} + \frac{\partial^2\Pi_z}{\partial y\partial z}\,\hat{y} + \left(\frac{\partial^2}{\partial z^2} + k_0^2\right)\Pi_z\,\hat{z}\right]\Bigg|_{z=z_p} \tag{2.27}$$

in which ϵ_0 denotes the permittivity of free space. Also, the Fourier transform of the intermediate Hertz potential Π_z is defined by

$$\underline{\Pi_z} = \left[\frac{e^{-|z-h|\gamma_0}}{2\gamma_0} + \frac{e^{-(z+h)\gamma_0}}{2\gamma_0}\frac{\gamma_0 - \frac{1}{\eta_{01}^2}\gamma_1}{\gamma_0 + \frac{1}{\eta_{01}^2}\gamma_1}\right]\Bigg|_{z=z_p} \tag{2.28}$$

wherein γ_m and the refractive index η_{0m} can be written as

$$\gamma_m = \sqrt{k^2 - k_0^2\eta_{0m}^2}\,,\ \ \eta_{0m} = \left[\frac{\epsilon_m}{\epsilon_0} + \frac{\sigma_m}{j\omega\epsilon_0}\right]^{1/2} \tag{2.29}$$

where the value of m can be 0 or 1. The inverse Fourier transform needs to be applied to (2.28) in order to determine the components of the electric field in (2.27). After taking the inverse Fourier transform of (2.28), the intermediate Hertz potential can be expressed as

$$\Pi_z = \frac{1}{4\pi^2}\int_{-\infty}^{+\infty}\int_{-\infty}^{+\infty}\left(\frac{e^{-|z-h|\gamma_0}}{2\gamma_0}+\frac{e^{-(z+h)\gamma_0}}{2\gamma_0}\right)e^{j(k_x x+k_y y)}dk_x dk_y - P \tag{2.30}$$

wherein

$$P = \frac{1}{4\pi^2}\int_{-\infty}^{+\infty}\int_{-\infty}^{+\infty}\frac{\frac{1}{\eta_{01}^2}\gamma_1}{\gamma_0+\frac{1}{\eta_{01}^2}\gamma_1}\frac{e^{-(z+h)\gamma_0}}{\gamma_0}\,e^{j(k_x x+k_y y)}dk_x dk_y. \tag{2.31}$$

2.2.1 Evaluation of Integrals

Although some approximate solutions have been offered for the calculation of (2.30), their accuracy depends significantly on the location of the observation point. Researchers in [36] and [71] used the free-space Green's function solution of the Helmholtz equation, which is referred to as the conventional method, as an approximation to simplify the integral in (2.30). Nonetheless, this approximation is justifiable at distances quite far away from the antenna and cannot follow the exact solution, which can be considered as the numerical solution, in the near and far field regions excluding quite far away distances from the source.

In order to reduce the complexity of calculation in (2.30) and (2.31), the double integral is converted to a single integral by changing the Cartesian integration variables

into polar form. Therefore, (2.30) can be converted to

$$\Pi_z = \frac{1}{4\pi}\int_0^{+\infty} k\left(\frac{e^{-|z-h|\gamma_0}}{\gamma_0} + \frac{e^{-(z+h)\gamma_0}}{\gamma_0}\right) J_0(k\rho)dk \;\; - 2P \tag{2.32}$$

and P can be changed to

$$P = \frac{1}{4\pi}\int_0^{+\infty} k\,\frac{\frac{1}{\eta_{01}^2}\gamma_1}{\gamma_0 + \frac{1}{\eta_{01}^2}\gamma_1}\frac{e^{-(z+h)\gamma_0}}{\gamma_0} J_0(k\rho)\,dk \tag{2.33}$$

wherein $J_0(k\rho)$ denotes the zero-order Bessel function with argument $k\rho$ and $\rho = \sqrt{x^2+y^2}$. Subsequently, (2.32) and (2.33) can be separated into three terms as

$$\text{Term 1} = \int_0^{+\infty} k\frac{e^{-|z-h|\gamma_0}}{\gamma_0} J_0(k\rho)\,dk \tag{2.34}$$

$$\text{Term 2} = \int_0^{+\infty} k\frac{e^{-(z+h)\gamma_0}}{\gamma_0} J_0(k\rho)\,dk \tag{2.35}$$

$$\text{Term 3} = \int_0^{+\infty} k\,\frac{\frac{1}{\eta_{01}^2}\gamma_1}{\gamma_0 + \frac{1}{\eta_{01}^2}\gamma_1}\frac{e^{-(z+h)\gamma_0}}{\gamma_0} J_0(k\rho)\,dk \tag{2.36}$$

and the intermediate Hertz potential, which consists of three terms, can be written as

$$\Pi_z = \frac{1}{4\pi}\left(\text{Term 1} + \text{Term 2} - 2\,\text{Term 3}\right). \tag{2.37}$$

2.2.1.1 Term 1 and Term 2

Our goal is to seek an approximate closed-form solution for terms in (2.34) - (2.36). The zero order Bessel function can be written as the sum of two Hankel functions of

the first and second kinds with the same argument as [15]

$$J_0(k\rho) = \frac{1}{2}\left[H_0^1(k\rho) + H_0^2(k\rho)\right] = \frac{1}{2}\left[H_0^1(k\rho) - H_0^1(-k\rho)\right]. \tag{2.38}$$

By substituting (2.38) into (2.34) and changing the limits of the second integral to $-\infty$ and zero, Term 1 can be written as

$$\text{Term 1} = \frac{1}{2}\int_{-\infty}^{+\infty} k\frac{e^{-|z-h|\gamma_0}}{\gamma_0} H_0^1(k\rho)dk. \tag{2.39}$$

The Hankel function of the first kind in (2.39) can be approximated by the first term of asymptotic expansion as

$$H_0^1(k\rho) \approx \sqrt{\frac{2}{\pi k\rho}} e^{j\left(k\rho - \frac{\pi}{4}\right)}. \tag{2.40}$$

Although this Hankel function approximation gets quite accurate for large arguments, its accuracy is still acceptable for small arguments. After substituting (2.40) into (2.39) and assuming that the observation point is higher than the antenna height on the z-axis (this assumption simply remove the absolute value in the exponential), Term 1 becomes

$$\text{Term 1} = \frac{1}{2}\sqrt{\frac{2}{\pi\rho}} e^{-j\frac{\pi}{4}} \int_{-\infty}^{+\infty} g(k)\, e^{jk\rho}\, dk \tag{2.41}$$

where

$$g(k) = \sqrt{\frac{k}{k^2 - k_0^2}}\, e^{-(z-h)\sqrt{k^2-k_0^2}}. \tag{2.42}$$

By approximating $g(k)$ with a complex exponential function at various k, an approximate closed-form solution for (2.41) can be obtained. Although using two exponential functions forms a better approximation, finding a closed-form expression in this case is practically impossible due to the system of nonlinear equations. The function of $g(k)$ decays fast when the magnitude of the argument is large. Therefore, it can be assumed that the function is close to zero after its argument reaches a certain value k_f, which depends on the wavenumber or frequency of the source. In order to estimate k_f, first, the behavior of $g(k)$ is represented with $w(k)$, defined by $w(k) = \frac{e^{-(z-h)k}}{\sqrt{k}}$, and then the value of k_f is calculated when the amplitude of $w(k)$ reaches 1% of its maximum (i.e., $\frac{e^{-(z-h)k_f}}{\sqrt{k_f}} = \frac{e^{-(z-h)k_0}}{100\sqrt{k_0}}$). Consequently, the tail of the function after k_f will not significantly affect the integral since the amplitude of the function after that point is close to zero. By applying the natural logarithm function to both sides of $w(k)$ and solving the obtained nonlinear equation employing linear approximation of the ln() function around k_f, k_f can be obtained as

$$k_f = \frac{9.2 + 2(z-h)k_0 + \ln(k_0) + n}{n + 2(z-h)} \tag{2.43}$$

in which

$$n = \frac{\ln\left(k_0 + 6.7e^{-1.1(z-h)} + 2e^{-0.1(z-h)}\right)}{k_0 + 6.7e^{-1.1(z-h)} + 2e^{-0.1(z-h)} - 1}. \tag{2.44}$$

As noted previously, it can then be assumed that for $|k| > k_f$, $g(k)$ is close to zero. For $-k_f < k < -k_0$ and $k_0 \leq k < k_f$, $g(k)$ of (2.42) is an imaginary and real function,

respectively, because of the presence of $\sqrt{k/(k^2-k_0^2)}$. Moreover, for $-k_0 \leq k < 0$ and $0 \leq k < k_0$, $g(k)$ becomes a complex value since the exponential function in (2.42) becomes complex. Therefore, we obtain estimates for $g(k)$ in the following intervals:

$$\begin{cases} -k_f < k < -k_0: & g(k) \approx jA_1 e^{B_1 k} \\ -k_0 \leq k < 0: & g(k) \approx A_2 e^{B_2 k} - jA_3 e^{B_3 k} \\ 0 \leq k < k_0: & g(k) \approx A_4 e^{B_4 k} + jA_5 e^{B_5 k} \\ k_0 \leq k < k_f: & g(k) \approx A_6 e^{B_6 k} \\ |k| > k_f: & g(k) \approx 0 \end{cases} \tag{2.45}$$

where

$$\begin{aligned} A_1 =& \sqrt{\frac{p_1}{p_1^2 - k_0^2}}\ \exp\left[-(z-h)\sqrt{p_1^2 - k_0^2} - B_1 p_1\right] \\ A_2 =& \frac{1}{\sqrt{k_0}}\ \cos\left[0.8k_0(z-h)\right]\ \exp\left(0.6k_0 B_2\right) \\ A_3 =& \frac{0.6}{\sqrt{k_0}}\ \sin\left[k_0(z-h)\right]\ \exp\left(0.3k_0 B_3\right) \\ A_4 =& \frac{1.2}{\sqrt{k_0}}\ \sin\left[0.7k_0(z-h)\right] \exp\left(-0.7k_0 B_5\right) \\ A_5 =& \frac{1}{\sqrt{k_0}}\ \cos\left[0.8k_0(z-h)\right] \exp\left(-0.6k_0 B_5\right) \\ A_6 =& \sqrt{\frac{p_1}{p_1^2 - k_0^2}}\ \exp\left[-(z-h)\sqrt{p_1^2 - k_0^2} + B_1 p_1\right] \end{aligned} \tag{2.46}$$

and also

$$
\begin{aligned}
B_1 =& \frac{\ln c - (z-h)\left[\sqrt{p_1^2 - k_0^2} - \sqrt{p_2^2 - k_0^2}\right]}{p_1 - p_2},\ p_1 = k_0 + \frac{k_f + k_0}{10},\ p_2 = k_0 + \frac{k_f + k_0}{5} \\
B_2 =& \frac{1}{0.3k_0} \ln\left[\frac{\cos\left[0.8k_0\left(z-h\right)\right]}{2.2\cos\left[0.43k_0\left(z-h\right)\right]}\right],\ B_3 = \frac{1}{0.6k_0} \ln\left[\frac{0.3\sin\left[0.8k_0\left(z-h\right)\right]}{\sin\left[0.43k_0\left(z-h\right)\right]}\right] \\
B_4 =& \frac{1}{0.6k_0} \ln\left[\frac{4k_0\sin\left[0.7\left(z-h\right)\right]}{\sin\left[k_0\left(z-h\right)\right]}\right],\ B_5 = \frac{1}{0.3k_0} \ln\left[\frac{2.2k_0\cos\left[0.43\left(z-h\right)\right]}{\cos\left[0.8k_0\left(z-h\right)\right]}\right] \\
B_6 =& \frac{\ln c - (z-h)\left[\sqrt{p_1^2 - k_0^2} - \sqrt{p_2^2 - k_0^2}\right]}{p_2 - p_1},\ c = \sqrt{\frac{p_1\left(p_2^2 - k_0^2\right)}{p_2\left(p_1^2 - k_0^2\right)}}.
\end{aligned}
\tag{2.47}
$$

By substituting (2.46) and (2.47) into (2.45), and then splitting the integral of (2.41) according to the five intervals in (2.45), Term 1 can be expressed as

$$
\begin{aligned}
\text{Term 1} \approx\ & j\frac{A_1}{B_1 + j\rho}\exp\left[-k_0(B_1 + j\rho)\right] + \frac{2A_2}{B_2 + j\rho}\sinh\left[\frac{k_0(B_2 + j\rho)}{2}\right] \\
& \exp\left[\frac{-k_0(B_2 + j\rho)}{2}\right] - j\frac{2A_3}{B_3 + j\rho}\sinh\left[\frac{k_0(B_3 + j\rho)}{2}\right]\exp\left[\frac{-k_0(B_3 + j\rho)}{2}\right] \\
& + \frac{2A_4}{B_4 + j\rho}\sinh\left[\frac{k_0(B_4 + j\rho)}{2}\right]\exp\left[\frac{k_0(B_4 + j\rho)}{2}\right] + j\frac{2A_5}{B_5 + j\rho} \\
& \sinh\left[\frac{k_0(B_5 + j\rho)}{2}\right]\exp\left[\frac{k_0(B_5 + j\rho)}{2}\right] - \frac{A_6}{B_6 + j\rho}\exp\left[k_0(B_6 + j\rho)\right].
\end{aligned}
\tag{2.48}
$$

The same procedure can be applied to Term 2 to find an approximate closed-form solution for that integral. However, the only difference between Term 1 and Term 2 is the $z + h$ term. In other words, by changing the term of $z - h$ to $z + h$ in (2.46) and (2.47), the solution for Term 2 can be obtained.

2.2.1.2 Term 3

In order to find an approximate closed-form solution for Term 3, the modified steepest descent method [74] is utilized to approximate this integral. Deforming the integration contour to lie on the steepest descent path leads to the following approximation for (2.29) in Term 3 because the significant portion of the integral occurs for k in the vicinity of the saddle point. Therefore, Term 3 can be expressed as

$$\text{Term } 3 = \int_0^{+\infty} k \, \frac{jk_0\beta}{\gamma_0 + jk_0\beta} \frac{e^{-(z+h)\gamma_0}}{\gamma_0} J_0(k\rho) \, dk \tag{2.49}$$

wherein $\beta = \frac{\gamma_1}{jk_0} \frac{1}{\eta_{01}^2}$ for $\eta_{01}^2 > 1$. By substituting (2.38) into (2.49) and changing the variable k as $k = k_0 \cos\alpha$, Term 3 becomes

$$\frac{jk_0\beta}{2} \int_{-j\infty}^{\pi+j\infty} \frac{\cos\alpha \; H_0^1(k_0\rho\cos\alpha) \; e^{-jk_0(z+h)\sin\alpha}}{\sin\frac{\alpha+\alpha_0}{2} \; \cos\frac{\alpha-\alpha_0}{2}} \, d\alpha \tag{2.50}$$

in which $\alpha_0 = \sin^{-1}(\beta)$. By employing the first term of asymptotic expansion of the Hankel function, which was mentioned in (2.40), Term 3 becomes

$$e^{j\frac{\pi}{4}} \beta \sqrt{\frac{k_0}{2\pi\rho}} \int_{-j\infty}^{\pi+j\infty} \frac{\sqrt{\cos\alpha} e^{-jk_0 R\cos(\theta-\alpha)}}{\sin\frac{\alpha+\alpha_0}{2} \cos\frac{\alpha-\alpha_0}{2}} \tag{2.51}$$

where R and θ are defined as

$$R = \sqrt{\rho^2 + (z+h)^2} \, , \quad \theta = -\tan^{-1}\left(\frac{z+h}{\rho}\right) \tag{2.52}$$

Using the modified steepest descent method, (2.51) can be further simplified as

$$\text{Term 3} \simeq j\sqrt{\pi P_e}\, e^{-W_e}\, \text{erfc}(j\sqrt{W_e})\, \frac{e^{-jk_0R}}{R} \tag{2.53}$$

in which W_e and P_e may be expressed as

$$P_e = -\frac{jk_0R}{2}\beta^2\,, \quad W_e \simeq P_e\left(1+\frac{h+z}{\beta R}\right)^2 \tag{2.54}$$

wherein erfc() denotes the complementary error function [75]. The intermediate Hertz potential Π_z is the sum of three terms and can be obtained from (2.37). By substituting (2.48) and (2.53) into (2.34) - (2.36) the approximate closed-form solution for Π_z can be obtained. Finally, by employing (2.27), the amplitude and phase of the scattered E-field can be calculated.

2.3 Results

In this section, we show the accuracy of the proposed solutions for calculating Term 1, Term 2 and Term 3 using the normalized root-mean-square error (NRMSE), while the numerical method presented in [76] with error tolerance 10^{-8} is used as reference. The NRMSE can be calculated using the reference and calculated values as

$$\text{NRMSE} = \frac{\left[\dfrac{\sum_{i=1}^{n}(\chi_i-\hat{\chi}_i)^2}{n}\right]^{1/2}}{\bar{\chi}} \tag{2.55}$$

wherein χ denotes the reference values, $\hat{\chi}$ represents the calculated values and n is the number of reference or calculated values. It should be noted that in (2.55), the mean value of the reference values ($\bar{\chi}$) is adopted to normalize the root-mean-square error (RMSE).

In order to evaluate the efficiency as well as the accuracy of the proposed closed-form solution for different distances from the source, NRMSE is calculated in the near and far field regions at each frequency, while the z coordinate of the observation point and antenna height are 1.5 m and 1 m, respectively. Furthermore, the relative permittivity and conductivity of the impedance half-plane is assumed to be 81 and 4 S/m respectively, which corresponds to seawater. It is worth mentioning that 101 points (i.e., n=101) have been considered here to calculate and plot the NRMSE in terms of the frequency and distance from the antenna.

For the near field evaluation, according to the near field definition, the value of NRMSE is calculated in terms of frequency, while the horizontal distance between the source and the observation point is changed between $-\lambda_0/10$ to $\lambda_0/10$, in which λ_0 denotes the wavelength of the source. Fig. 2.3(a) depicts the value of NRMSE in terms of frequency for the near field region for Term 1. The value of NRMSE is obtained at each frequency when the observation point is changed in the near field region. As is evident, the NRMSE value of the proposed solution for the near field regions is less than 0.06, and also less than the free-space Green's function solution of the Helmholtz equation, which is referred to as the conventional method, for all

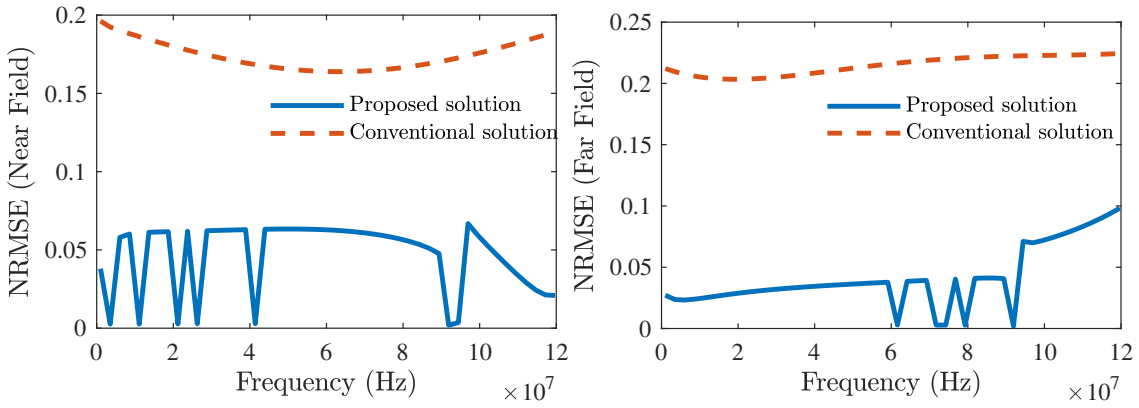

Fig. 2.3: Comparison between the conventional and proposed solutions for Term 1 in terms of NRMSE in the (a) near field region and (b) far field region.

frequencies shown. It should be noted that the proposed approximations for the integrand of Term 1 and Term 2 depend on the frequency (i.e., the points defined in each integral limit for the approximation of the integrand depend on the frequency), and they become small at some frequencies such as 20 MHz in 2.3(a). This results in sharp reductions in the NRMSE shown in Fig. 2.3. For the far field regions, according to its definition, the horizontal distance between the source and the observation point is changed between $-10\lambda_0$ to $10\lambda_0$ excluding the near field region. Fig. 2.3(b) depicts the NRMSE value of Term 1 at each frequency when the observation point is in the far field of the antenna. As can be seen in this figure, the NRMSE is less than 0.08 at various frequencies. This figure shows that the proposed solution of Term 1 outperforms the conventional solution in terms of NRMSE and it can be safely used up to the VHF band for both near and far field regions. It is worth mentioning that the NRMSE value of Term 2 for the near and far field regions is similar to Term 1

due to the fact that only $z - h$ is changed to $z + h$ in (2.46) and (2.47).

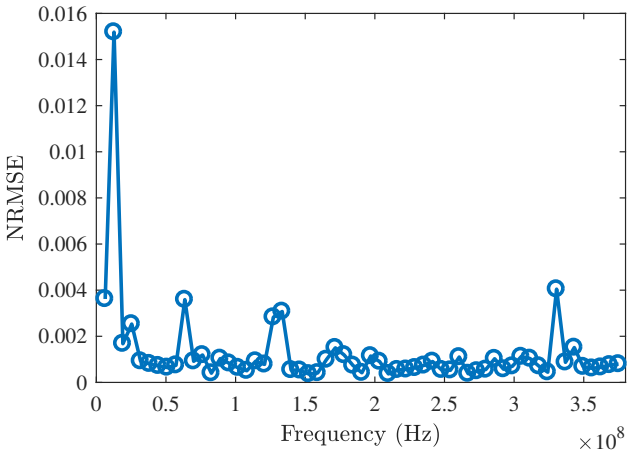

Fig. 2.4: The value of NRMSE for Term 3 at various frequencies.

Fig. 2.4 shows the NRMSE of Term 3 at various frequencies when the horizontal distance between the source and the observation point is between $-10\lambda_0$ to $10\lambda_0$. As shown, the NRMSE is less than 0.015 for all frequencies and indicates the accuracy of the proposed solution.

The HF band is employed in radio oceanography and HF radars use high frequency radio waves in order to remotely measure sea surface parameters after receiving scattered fields [77–79]. The proposed technique can be applied to the ocean surface, which is used to study weather, climate and other dynamic ocean phenomena, in order to find the scattered E-field. By assuming air and seawater EM properties, the intermediate Hertz potential can be acquired. The proposed solutions are employed for calculating the intermediate Hertz potential, which consists of Term 1, Term 2 and Term 3, and is compared with results obtained by the numerical method [76]. It

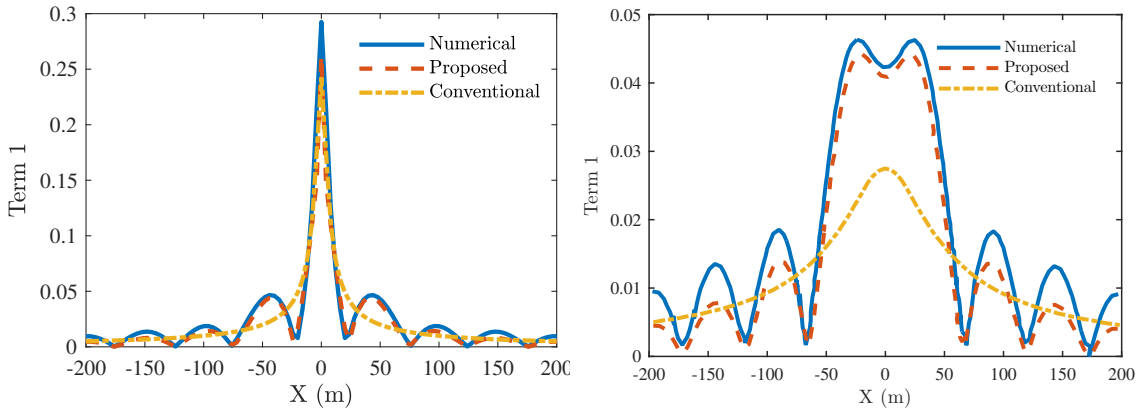

Fig. 2.5: Comparison between the numerical, proposed and conventional methods for the magnitude of Term 1 in (a) $Y = 0$ plane and (b) $Y = 36$ m plane.

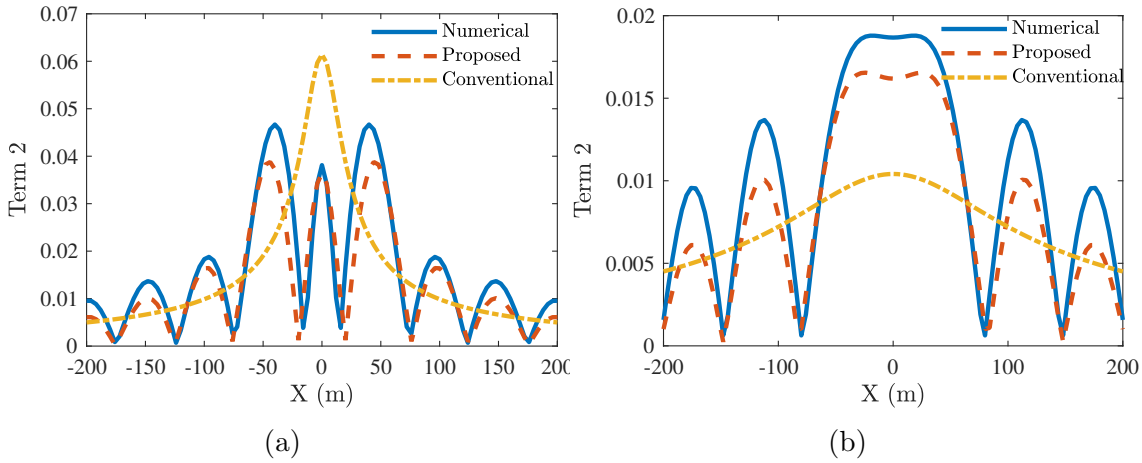

Fig. 2.6: Comparison between the numerical, proposed and conventional methods for the magnitude of Term 2 in (a) $Y = 16$ m plane and (b) $Y = 96$ m plane.

should be noted that the frequency of the antenna has been assumed to be 30 MHz and also the z coordinate of the observation point and antenna height have been assumed to be 2 m and 1 m, respectively. Fig. 2.5(a) shows the magnitude of Term 1 between -200 m to $+200$ m in the $Y = 0$ plane. As can be seen in this figure, the closed-form solution has good agreement with the numerical solution in all intervals

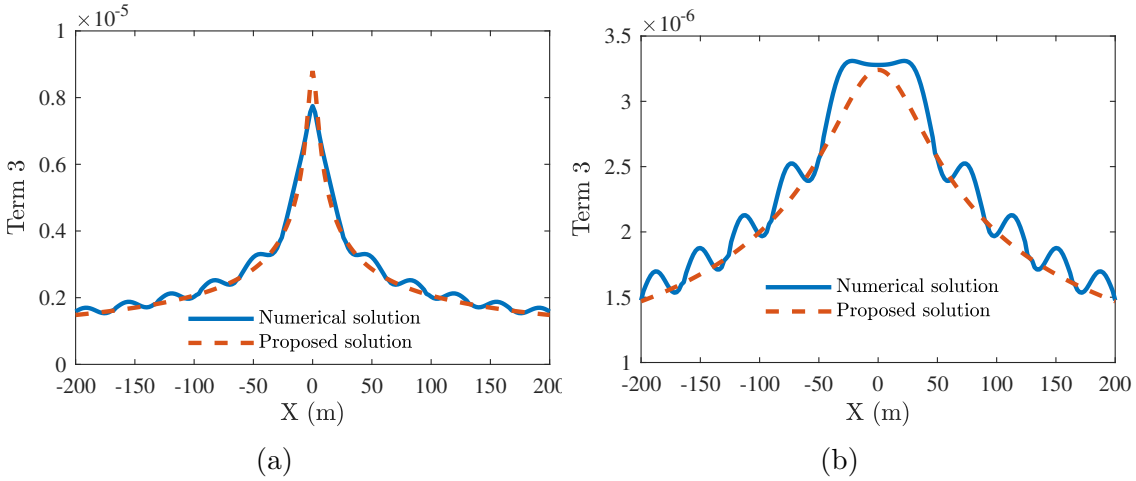

Fig. 2.7: Comparison between the numerical and proposed solutions for the magnitude of Term 3. (a) In $Y = 0$ plane. (b) In $Y = 38$ m plane.

and can follow the oscillation of the response in the near and far field regions. On the other hand, except for the region surrounding the antenna, which has a large value, the conventional method is unable to match the numerical solution in the near and far field regions. Far from the point at which all solutions converge to a certain value, the conventional solution is quite accurate. Fig. 2.5(b) also shows the magnitude of Term 1 for the $Y = 36$ m plane. As can be seen in this figure, the proposed solution follows the numerical solution not only in the near field region, but also in the far field region. However, the conventional solution can only be acceptable at distances far away from the antenna. Although the main difference between Term 1 and Term 2 is the sign of h in $z - h$, the magnitude of Term 2 in two different planes has been obtained and shown in Fig. 2.6. As is obvious in this figure, the proposed solution outperforms the conventional solution at various distances from the antenna. Fig. 2.7 also shows the magnitude of Term 3 between -200 m to $+200$ m in the $Y = 0$ and

$Y = 38$ m planes. Note that these two planes are simply being used as examples. For the proposed and numerical solution, as can be seen in this figure, the proposed solution has a good agreement with the numerical method in both near and far field regions.

2.4 Chapter Summary

In this chapter, the development of an approximate analytical solution for the intermediate Hertz potential over a smooth lossy half-space below the VHF band is presented. The first and second terms of the intermediate Hertz potential are calculated using hyperbolic functions, and the third term is represented with the help of the error function, which is dependent on the frequency, observation point and electromagnetic properties of the half-space. In order to verify the obtained results, the solutions are compared with the numerical and conventional methods for different cases (i.e., various frequencies and distances from the source). The comparisons indicate that the proposed solutions are more accurate than the conventional method at various frequencies (up to the VHF band) and distances from the antenna in the near and far field regions.

Chapter 3

Scattered Electric Field Calculation for Frequencies Below 10 GHz

In the previous chapter, an approximate solution for the intermediate Hertz potential below the VHF band for highly conductive surfaces was proposed. In this chapter[1], the classical Sommerfeld half-space problem with a smooth interface is revisited, and

[1]The content of this chapter is based on the following publications:
-M. E. Nazari and W. Huang, "An analytical solution of the electric field excited by a vertical electric dipole above a lossy half-space: From radio to microwave frequencies," IEEE Trans. Antennas Propag., vol. 68, no. 11, pp. 7517-7529, 2020.
-M. E. Nazari and W. Huang, "An analytical solution of the electric field radiated by a dipole over a layered half-space," IEEE AP-S/URSI, vol. 68, no. 11, pp. 943-944, 2020.
These papers propose the development of the scattered E-field over a lossy half-space at different frequencies (below 10 GHz) and distances from the antenna in the near and far field regions.
Roles: Mr. Nazari conducted this research under the guidance of Dr. Huang and acted as the first author of the manuscript. All the contents of this paper were written by Mr. Nazari and further refined by Dr. Huang.

rigorous approximate closed-form solutions for the scattered electric field and intermediate Hertz potential for a source above good dielectric and conductor media below 10 GHz in the near and far field regions are presented. The theoretical development is validated by representative numerical results and compared with the widely accepted solutions presented in [36] and [25], referred to as the King and the Norton-Bannister methods, respectively. It is worth mentioning that those solutions are valid in both near and far-field regions, as well as high media contrast (i.e., $|\eta^2| \gg 1$).

This chapter is organized as follows. In Section 3.1, the scattered electric field components using the intermediate Hertz potential over a lossy half-space are derived. A rigorous approximate closed-form solution for the intermediate Hertz potential and scattered electric field components in the near and far-field regions is proposed in Section 3.2. Finally, in Section 3.3, the proposed solutions are evaluated numerically and compared with the conventional methods, i.e., King [36] and Norton-Bannister [25] methods, at various frequencies, from radio to microwave frequencies, in the near and far field regions.

3.1 Problem Statement and Formulation

The scattered electric field components from a lossy half-space when the source is taken to be a VED located on the z-axis of the Cartesian coordinate system at height h above a lossy half-space, as illustrated in Fig. 2.2, can be obtained from (2.27). By

using the Sommerfeld approximation in the cylindrical coordinate [80]

$$\int_0^{\infty} \frac{e^{-jk_z|z|}}{jk_z} J_0(k_\rho \rho) k_\rho dk_\rho \approx \frac{e^{-jkr}}{r}, \tag{3.1}$$

the intermediate Hertz potential in (2.30) can be approximated as [17, 81]

$$\Pi_z \simeq \frac{1}{4\pi}\left(\frac{e^{-jk_0R_0}}{R_0} + \frac{e^{-jk_0R_1}}{R_1} - 2P\right) \tag{3.2}$$

wherein

$$R_0 = (\rho^2 + (z_p - h)^2)^{1/2},\ R_1 = (\rho^2 + (z_p + h)^2)^{1/2}. \tag{3.3}$$

Also, P expressed initially in (2.31) can be represented as

$$P = \frac{1}{4\pi^2} \iint_{-\infty}^{+\infty} \frac{\frac{1}{\eta_{01}^2}\gamma_1}{\gamma_0 + \frac{1}{\eta_{01}^2}\gamma_1} \frac{e^{-(z+h)\gamma_0}}{\gamma_0}\ e^{j(k_x x + k_y y)} dk_x dk_y \tag{3.4}$$

while γ_1 is calculated from (2.29). In order to reduce the complexity of the calculations in (3.4), the double integral is converted to a single integral by changing the Cartesian integration variables into polar form. Subsequently, (3.4) can be written as

$$P = \int_0^{\infty} k\ \frac{\frac{1}{\eta_{01}^2}\gamma_1}{\gamma_0 + \frac{1}{\eta_{01}^2}\gamma_1} \frac{e^{-(z+h)\gamma_0}}{\gamma_0} J_0(k\rho)\ dk \tag{3.5}$$

in which the function $J_0(k\rho)$ denotes the Bessel function of the first kind of order zero and $\rho = \sqrt{x^2 + y^2}$ indicates the horizontal distance between the source and the observation point. By decomposing P into partial fractions and assuming that the observation point is higher than the antenna height on the z-axis, (3.5) becomes

$$P = \int_0^\infty \frac{k}{\gamma_0} e^{-(z+h)\gamma_0} J_0(k\rho) dk - \int_0^\infty \frac{k e^{-(z+h)\gamma_0}}{\gamma_0 + \frac{1}{\eta_{01}^2}\gamma_1} J_0(k\rho) dk. \tag{3.6}$$

After employing the Sommerfeld approximation, (3.6) may be simplified as

$$P = \frac{e^{-jk_0 R_1}}{R_1} - \int_0^\infty \frac{k}{\gamma_0 + \frac{1}{\eta_{01}^2}\gamma_1} e^{-(z+h)\gamma_0} J_0(k\rho)\, dk. \tag{3.7}$$

By multiplying the numerator and denominator by the conjugate of the denominator, the integral part in (3.7) can be divided into two parts, I_1 and I_2, as

$$I_1 = \frac{\eta_{01}^4}{\eta_{01}^4 - 1} \int_0^\infty \frac{k\sqrt{k^2 - k_0^2}}{k^2 - \frac{\eta_{01}^2}{\eta_{01}^2 + 1} k_0^2} e^{-(z+h)\gamma_0}\, J_0(k\rho)\, dk \tag{3.8}$$

$$I_2 = -\frac{\eta_{01}^2}{\eta_{01}^4 - 1} \int_0^\infty \frac{k\sqrt{k^2 - \eta_{01}^2 k_0^2}}{k^2 - \frac{\eta_{01}^2}{\eta_{01}^2 + 1} k_0^2} e^{-(z+h)\gamma_0}\, J_0(k\rho)\, dk. \tag{3.9}$$

The amplitude and the phase of $\nu^2 = \dfrac{\eta_{01}^2}{\eta_{01}^2+1}$ in the denominator of (3.8) and (3.9) can be written as

$$\left|\nu^2\right| = \left[\frac{1+\tan^2\delta}{\left(\dfrac{\epsilon_r+1}{\epsilon_r}\right)^2+\tan^2\delta}\right]^{1/2} \tag{3.10}$$

$$\angle\nu^2 = -\tan^{-1}(\tan\delta) + \tan^{-1}\left(\frac{\epsilon_r\tan\delta}{\epsilon_r+1}\right) \tag{3.11}$$

where $\tan\delta$ and ϵ_r indicate the loss tangent and the permittivity of the half-space, respectively. For good dielectrics ($\tan\delta \ll 1$ such as sea ice in the HF frequency band) and good conductors ($\tan\delta \gg 1$ such as ocean surface in the HF frequency band), which are media of practical importance in applications, the amplitude (3.10) and the phase (3.11) can be replaced by 1 and 0, respectively, when the media contrast is relatively high. Therefore, by substituting $\dfrac{\eta_{01}^2}{\eta_{01}^2+1}$ by 1 in (3.8) and (3.9) and employing the Sommerfeld approximation, (3.8) and (3.9) can be further simplified to the following equations.

$$I_1 \simeq \frac{\eta_{01}^4}{\eta_{01}^4-1}\int_0^\infty \frac{k\,e^{-(z+h)\gamma_0}}{\sqrt{k^2-k_0^2}}\,J_0(k\rho)\,dk = \frac{\eta_{01}^4\,e^{-jk_0R_1}}{R_1\,(\eta_{01}^4-1)} \tag{3.12}$$

$$I_2 \simeq -\frac{\eta_{01}^2}{\eta_{01}^4-1}\int_0^\infty \frac{k\sqrt{k^2-\eta_{01}^2k_0^2}}{k^2-k_0^2}e^{-(z+h)\gamma_0}\,J_0(k\rho)\,dk \tag{3.13}$$

By inserting (3.12) and (3.13) into (3.7), P may be expressed as

$$P \simeq \frac{e^{-jk_0R_1}}{R_1\,(1-\eta_{01}^4)} + \frac{j\eta_{01}^3k_0}{\eta_{01}^4-1}\int_0^\infty \frac{k}{\gamma_0^2}\,e^{-(z+h)\gamma_0}J_0(k\rho)\,dk, \tag{3.14}$$

which consists of a Sommerfeld-type integral.

3.2 Sommerfeld-type Integral Evaluation

In order to calculate the scattered electric field components, first, the intermediate Hertz potential should be calculated. By evaluating (3.14) and then substituting into (3.2), the intermediate Hertz potential and scattered electric field components can be evaluated. In this section, accurate approximate closed-form solutions for the intermediate Hertz potential and the scattered electric field are proposed. The solutions are obtained for the near field, far field and the particular case of $z_p = h = 0$, which implies that both transmitter and receiver are at the interface.

3.2.1 Particular Scattering Problem ($z_p = h = 0$)

In coplanar circuits and antennas, particularly microstrip antennas, the metallization corresponding to the source and observation points is at the interface between the dielectric and the air [82]. In order to calculate the scattered electric field components, the height of the antenna and the z coordinate of the observation point are equal to zero. Consequently, the intermediate Hertz potential (3.2) and also P (3.14) can be reduced to

$$\Pi_z = \frac{1}{2\pi}\left(\frac{e^{-jk_0\rho}}{\rho} - P\right) \tag{3.15}$$

and

$$P \simeq \frac{e^{-jk_0\rho}}{\rho\,(1-\eta_{01}^4)} + \frac{j\eta_{01}^3 k_0}{\eta_{01}^4 - 1}\int_0^\infty \frac{k}{k^2-k_0^2}\,J_0(k\rho)\,dk. \tag{3.16}$$

By decomposing the integral part of (3.16) into partial fractions, the integral is split up into two separate integrals, I_3 and I_4, as follows:

$$I_3 = \frac{1}{2}\int_0^\infty \frac{J_0(k\rho)}{k+k_0}\,dk \tag{3.17}$$

$$I_4 = \frac{1}{2}\int_0^\infty \frac{J_0(k\rho)}{k-k_0}\,dk. \tag{3.18}$$

By using the Bessel function transform, the exact expression of (3.17) can be written as

$$I_3 = \frac{1}{2}\int_0^\infty \frac{J_0(k\rho)}{k+k_0}\,dk = \frac{\pi}{4}\left[H_0\left(k_0\rho\right) - Y_0\left(k_0\rho\right)\right] \tag{3.19}$$

in which $H_0(\cdot)$ denotes the Struve function and $Y_0(\cdot)$ indicates the zero order Bessel function of the second kind (Neumann function) available for reference in [75]. By employing the small and large argument approximation for the Bessel function in (3.18) and performing the change of variable ($k\rho = t$), I_4 can be written as

$$I_4 \simeq \frac{1}{2}\int_0^1 \frac{\cos(0.7t)}{t-k_0\rho}\,dt + \frac{1}{\sqrt{2\pi}}\int_1^\infty \frac{\cos(t-\pi/4)}{\sqrt{t}\,(t-k_0\rho)}\,dt. \tag{3.20}$$

By approximating $1/\sqrt{t}$ within the limits of integration in (3.20) using the rational function $\dfrac{a_r}{t+b_r} + c_r$, in which $a_r = 5.4$, $b_r = 6.8$ and $c_r = 0.03$ are calculated by considering three points between 1 and 1% of the maximum integrand amplitude, the

approximate closed-form solution of I_4 can be expressed as

$$\begin{aligned} I_4 \simeq \frac{1}{2}\cos(0.7k_0\rho)\big[\,\mathrm{Ci}(0.7(1-k_0\rho)) - \mathrm{Ci}(-0.7k_0\rho)\big] + \frac{1}{2}\sin(0.7k_0\rho)\big[\,\mathrm{Si}(-0.7k_0\rho) \\ - \mathrm{Si}(0.7(1-k_0\rho))\big] + \frac{1}{\sqrt{2\pi}}\left(\frac{a_r}{k_0\rho+b_r}+c_r\right)\Bigg[\sin(k_0\rho-\pi/4)\,\mathrm{Si}(1-k_0\rho) \\ - \frac{\pi}{2}\sin(k_0\rho-\frac{\pi}{4}) - \cos(k_0\rho-\frac{\pi}{4})\,\mathrm{Ci}(1-k_0\rho)\Bigg] - \frac{1}{\sqrt{2\pi}}\left(\frac{a_r}{b_r+k_0\rho}\right)\Bigg[\frac{\pi}{2}\sin(b+\frac{\pi}{4}) \\ - \cos(b+\frac{\pi}{4})\,\mathrm{Ci}(1+b) - \sin(b+\frac{\pi}{4})\,\mathrm{Si}(1+b)\Bigg] \end{aligned} \tag{3.21}$$

wherein Ci indicates the Cosine integral and Si denotes the Sine integral [75]. By substituting I_3 and I_4 into (3.16), the approximate closed-form solution of the intermediate Hertz potential (3.15) can be obtained as

$$\Pi_z = \frac{1}{2\pi(\eta_{01}^4-1)}\left[\frac{e^{-jk_0\rho}}{\rho} - j\eta_{01}^3 k_0(I_3+I_4)\right]. \tag{3.22}$$

In order to calculate the scattered electric field components, the intermediate Hertz potential (3.2) along with (3.14) is substituted into (2.27) and then the antenna height and z coordinate of the observation point are set to zero. Afterwards, (3.22) is employed as the intermediate Hertz potential. Therefore, the approximated scattered electric field components over the lossy half-space can be obtained as

$$\begin{aligned} \vec{E} = \frac{I\Delta l}{j2\pi\omega\epsilon_0}\frac{e^{-jk_0\rho}}{\rho}\Bigg[\frac{-jk_0\eta_{01}^3}{\rho^2\,(\eta_{01}^2-1)}\,(x\,\hat{x}+y\,\hat{y}) + \Bigg(k_0^2 - \frac{1}{\rho^2} - \frac{jk_0}{\rho} + \frac{1+jk_0\rho}{\rho^2(1-\eta_{01}^4)} \\ - k_0^2 P\Bigg)\,\hat{z}\Bigg] \end{aligned} \tag{3.23}$$

wherein P can be expressed as

$$P \simeq \frac{e^{-jk_0\rho}}{\rho\,(1-\eta_{01}^4)} + \frac{j\eta_{01}^3 k_0}{\eta_{01}^4 - 1}\,(I_3 + I_4)\,. \tag{3.24}$$

In comparison with the King [36] and Norton-Bannister [25] formulations, the proposed approximate closed-form solution of the scattered electric field is valid not only in the far-field region, but also in the near-field region. Moreover, as can be seen in (3.23), the magnitude of the scattered electric field decays with respect to the free-space Green's function.

3.2.2 Near-Field Region

In the near-field observation, where the horizontal distance of the observation point is much less than the free space wavelength (i.e., $k_0\rho \ll 1$), the evaluation of the electric field components becomes important due to its application in EM wave scattering applications, such as ground penetrating radar (GPR) [83] and nondestructive testing and evaluation [84]. GPR uses backscattered fields over half-spaces (mostly soil) for subsurface surveying. The far-field solutions of calculating depths, which are of interest for GPR applications, may not accurately describe radiation patterns in the near-surface since the scattered electric field components are commonly measured over ranges of centimetres or metres, which is in the near-field region of the antenna at the operating frequency. In order to calculate the scattered electric field components in the near-field regions, first, the intermediate Hertz potential (3.2) along with (3.14) is

calculated in the near-field region, and then all electric field components are calculated using (2.27).

By decomposing the integral part of (3.14) into partial fractions, it can be divided into two integrals, I_5 and I_6, as follows:

$$I_5 = \frac{1}{2}\int_0^\infty \frac{e^{-(z+h)\sqrt{k^2-k_0^2}}}{k+k_0}\, J_0(k\rho)\, dk \tag{3.25}$$

$$I_6 = \frac{1}{2}\int_0^\infty \frac{e^{-(z+h)\sqrt{k^2-k_0^2}}}{k-k_0}\, J_0(k\rho)\, dk. \tag{3.26}$$

I_5 can be further split up according to the different behaviour of the exponential function, which can be real or complex at various k. It should be noted that, for $0 < k < 1/\rho$, the small argument approximation of the Bessel function is used because the argument of the Bessel function ($k\rho$) is less than one in this interval. However, for $k > 1/\rho$, the argument of the Bessel function is greater than one and the large argument approximation of the Bessel function is employed for this interval. Therefore, I_5 can be written as

$$\begin{aligned} I_5 =& \frac{1}{2}\int_0^{k_0} \frac{e^{-j(z+h)\sqrt{k_0^2-k^2}}}{k+k_0}\, \cos(0.7k\rho)\, dk + \frac{1}{2}\int_{k_0}^{1/\rho} \frac{e^{-(z+h)\sqrt{k^2-k_0^2}}}{k+k_0}\, \cos(0.7k\rho)\, dk \\ &+ \frac{1}{\sqrt{2\pi\rho}}\int_{1/\rho}^\infty \frac{e^{-(z+h)\sqrt{k^2-k_0^2}}}{\sqrt{k}(k+k_0)}\, \cos(k\rho-\pi/4)\, dk. \end{aligned} \tag{3.27}$$

In (3.27), for $k > 1/\rho$, $\dfrac{e^{-(z+h)\sqrt{k^2-k_0^2}}}{\sqrt{k}}$ can be approximated by a rational function since it decays when the value of k is greater than $1/\rho$. In addition, it can be assumed

that the function is close to 0 when k reaches k_u, which depends on the wavenumber or frequency of the source, z coordinate of the observation point and antenna height. The value of k_u is obtained when the amplitude of $e^{-(z+h)\sqrt{k^2-k_0^2}}/\sqrt{k}$ reaches 1% of its maximum, which is $0.01/\sqrt{k_0}$. Thus, the tail of the aforementioned function may not impact the integral because the amplitude can be assumed to be zero after k_u. In order to calculate the value of k_u, the nonlinear equation $\left.\dfrac{e^{-(z+h)\sqrt{k^2-k_0^2}}}{k+k_0}\right|_{k=k_u} = \dfrac{1}{100\sqrt{k_0}}$ should be solved. After applying the $\ln(\cdot)$ function to both sides and using the linear approximation of the $\ln(\cdot)$ function around k_0, k_u can be obtained as

$$k_u = \frac{n_p g_1 + \left[(n_p g_1)^2 - (n_p^2 - 1)(g_1^2 + k_0^2)\right]^{1/2}}{1 - n_p^2} \tag{3.28}$$

in which $g_1 = \dfrac{4.6}{z+h} + \dfrac{0.01}{k_0(z+h)}$ and $n_p = -\dfrac{1}{50(z+h)k_0}$.

In (3.27), for $0 < k < k_0$, the function of $\sqrt{k_0^2 - k^2}$ can be approximated as a second-degree polynomial function, and the rational function $\dfrac{1}{k+k_0}$ can be approximated as an exponential function, as shown in (3.29). Also, for $k_0 < k < 1/\rho$, $\dfrac{e^{-(z+h)\sqrt{k^2-k_0^2}}}{k+k_0}$ behaves as a rational function when the value of k increases from k_0 to $1/\rho$ in the interval. Consequently, the following approximations are applied to (3.27)

over various integrals of k to find an approximate closed-form solution for I_5:

$$\begin{aligned}
0 < k < k_0: \quad & \sqrt{k_0^2 - k^2} \simeq p_1 k^2 + p_2 k + p_3\,, \\
& \frac{1}{k + k_0} \simeq p_4 \exp(p_5 k) \\
k_0 < k < \frac{1}{\rho}: \quad & \frac{e^{-(z+h)\sqrt{k^2 - k_0^2}}}{k + k_0} \simeq \frac{p_6}{k + p_7} \\
\frac{1}{\rho} < k < k_u: \quad & \frac{e^{-(z+h)\sqrt{k^2 - k_0^2}}}{\sqrt{k}} \simeq \frac{p_8}{k + p_9} \\
k > k_u: \quad & \frac{e^{-(z+h)\sqrt{k^2 - k_0^2}}}{\sqrt{k}} \simeq 0
\end{aligned} \tag{3.29}$$

In order to find the unknown coefficients of the second-degree polynomial function in the first interval of (3.29), three points are required to be fitted to the original function. To obtain an accurate approximation, the interval is divided into four sections and the first, second and third quarter points are selected to fit the proposed function into the original function. For the rational function approximation using an exponential function at the first interval in (3.29), the first and third quarter points are selected. In order to approximate the rational-exponential function at the second and third intervals in (3.29) using a rational function, the second and third quarter points are considered to obtain accurate approximations. Subsequently, all the unknown coefficients in (3.29) (i.e., $p_i, i = 1, 2, ..., 9$) can be expressed as

$$p_1 = \frac{-0.82}{k_0},\ p_2 = 0.2,\ p_3 = 0.97k_0,\ p_4 = \frac{0.94}{k_0},\ p_5 = \frac{-0.67}{k_0},\ a = z+h,\ k_3 = \frac{3}{4\rho} + \frac{k_u}{4}$$

$$
\begin{aligned}
p_6 =& \frac{k_1+p_7}{k_1+k_0}\exp\left(-a\sqrt{k_1^2-k_0^2}\right),\ p_7=\frac{k_2-h_0k_1}{h_0-1}, k_1=\frac{3k_0}{4}+\frac{1}{4\rho},\ k_2=\frac{k_0}{4}+\frac{3}{4\rho},\\
h_0 =& \frac{k_2+k_0}{k_1+k_0}\exp\left[-a\left(\sqrt{k_1^2-k_0^2}-\sqrt{k_2^2-k_0^2}\right)\right],\ p_8=\frac{k_3+p_9}{\sqrt{k_3}}\exp\left(-a\sqrt{k_3^2-k_0^2}\right),\\
p_9 =& \frac{k_4-h_1k_3}{h_1-1}, h_1=\sqrt{\frac{k_3}{k_4}}\exp\left[-a\left(\sqrt{k_3^2-k_0^2}-\sqrt{k_4^2-k_0^2}\right)\right],\ k_4=\frac{1}{4\rho}+\frac{3k_u}{4}.
\end{aligned}
\tag{3.30}
$$

In order to evaluate the proposed approximations in (3.29), the absolute error of those functions are calculated for the first two intervals shown in Fig. 3.1. The evaluation of the error for the fourth function associated with the third interval has not been shown here since it is quite similar to the second interval.

By employing the proposed approximations in (3.29) for each integrand function in (3.27) and evaluating the integrals, the approximate closed-form expression for I_5 can be obtained as

$$
\begin{aligned}
I_5 \simeq& \frac{\sqrt{\pi}e^{-jap_3}p_4}{8\sqrt{jap_1}}\left[\exp\left(\frac{(p_5-jap_2-j0.7\rho)^2}{j4ap_1}\right)\left[\mathrm{erf}\left(\frac{ja(2p_1k_0+p_2)-p_5+j0.7\rho}{2\sqrt{jp_1a}}\right)\right.\right.\\
&\left.-\mathrm{erf}\left(\frac{jap_2-p_5+j0.7\rho}{2\sqrt{jp_1a}}\right)\right]+\exp\left(\frac{(p_5-jap_2+j0.7\rho)^2}{j4ap_1}\right)\\
&\left.\left[\mathrm{erf}\left(\frac{ja(2p_1k_0+p_2)-p_5+j0.7\rho}{2\sqrt{jp_1a}}\right)-\mathrm{erf}\left(\frac{jap_2-p_5+j0.7\rho}{2\sqrt{jp_1a}}\right)\right]\right]
\end{aligned}
$$

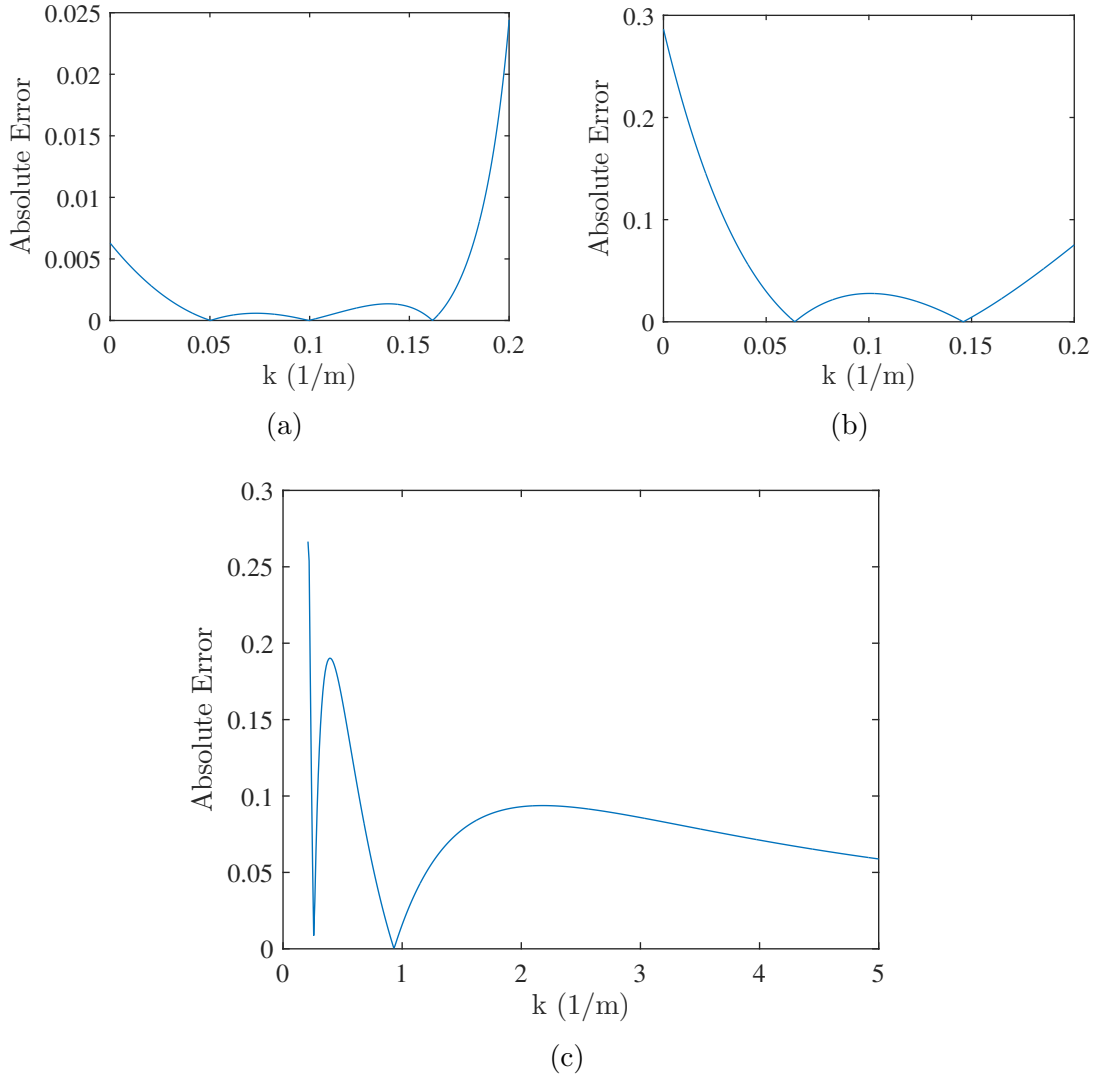

Fig. 3.1: The absolute error of the proposed approximations in 3.29. (a) The first function of the first interval. (b) The second function of the the first interval. (c) The third function in the second interval.

$$+\frac{p_6}{2}\Big[\sin(0.7\rho\,p_7)\left[\,\mathrm{Si}\,(0.7+0.7\rho\,p_7)-\mathrm{Si}\,(0.7\rho\,(k_0+p_7))\,\right]+\cos(0.7\rho\,p_7)$$
$$\left[\,\mathrm{Ci}\,(0.7+0.7\rho\,p_7)-\mathrm{Ci}\,(0.7\rho\,(k_0+p_7))\,\right]\Big]+\frac{p_8}{(p_9-k_0)\sqrt{2\pi\rho}}\Big[-\sin(\rho\,p_9+\frac{\pi}{4})$$
$$\Big[\frac{\pi}{2}-\mathrm{Si}(1+\rho\,p_9)\Big]+\cos(\rho\,p_9+\frac{\pi}{4})\,\mathrm{Ci}(1+\rho\,p_9)+\sin(\rho k_0+\frac{\pi}{4})\big[\frac{\pi}{2}-\mathrm{Si}\,(1+\rho k_0)\,\big]$$
$$-\cos(ck_0+\frac{\pi}{4})\,\mathrm{Ci}\,(1+\rho k_0)\Big] \tag{3.31}$$

in which erf represents the Gauss error function [75]. I_6 is the last integral that should be evaluated for finding the approximate closed-form solution for (3.14), which is a part of the intermediate Hertz potential. The difference between I_5 and I_6 is the pole of k_0 lies on the positive real axis of k. It will be shown that the solution of (3.26) only depends on the wavenumber or frequency of the source, z coordinate of the observation point and antenna height, and is not contingent on the horizontal distance between the observation point and antenna. Therefore, the approximate closed-form solution of (3.26) can be approximated as

$$I_6 \simeq \frac{1}{2}\sum_{i=1}^{2} a_i J_0(b_i\, k_0 + c_i) + \frac{j}{2}\sum_{i=3}^{4} a_i J_0(b_i\, k_0 + c_i). \tag{3.32}$$

The approximate solution in (3.32) does not significantly depend on ρ (i.e., its variation is negligible at various horizontal distances) because the pole of k_0 lies on the positive real axis of k. In other words, the solution of the integral is related to the residue of the integrand at its pole. By assuming the near-field ($k_0\rho \ll 1$) and the far-field ($k_0\rho \gg 1$) regions, the value of $J_0(k_0\rho)$, which is a part of the residue of the integrand, is not significantly dependent on ρ since for small arguments it can be assumed as one and for large arguments it can be neglected. For instance, the numerical solution of I_6 is calculated at different frequencies with respect to ρ in the near field region in order to show the independence of its solution to ρ. Figs. 3.2 and 3.3 show the real and imaginary parts of I_6 with respect to ρ in two different frequencies, i.e., 10 MHz and 10 GHz, and two different a values, i.e., $a = 10$ m and $a = 2$ m. As can

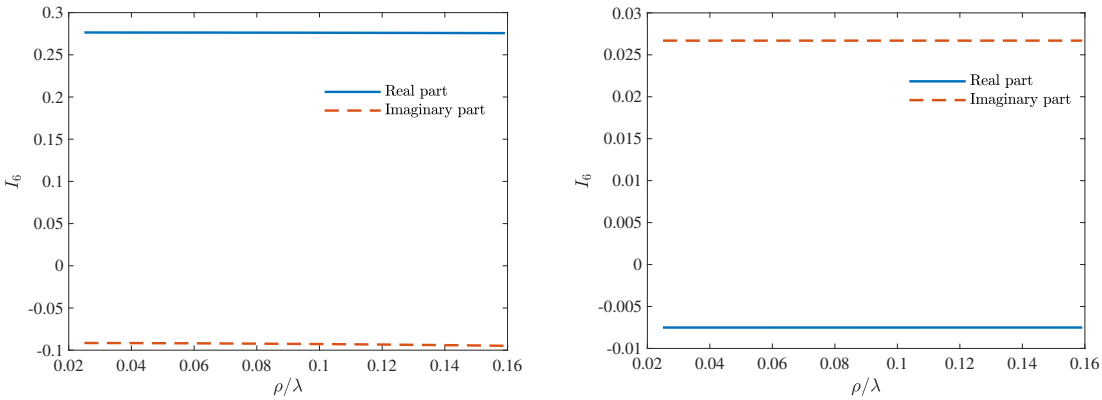

(a) (b)

Fig. 3.2: The real and imaginary parts of I_6 for $a = 10$ m at a) 10 MHz and b) 10 GHz.

be seen from the figures, both the real and imaginary parts of I_6 do not significantly depend on ρ at different frequencies and a values. All the coefficients in (3.32) can

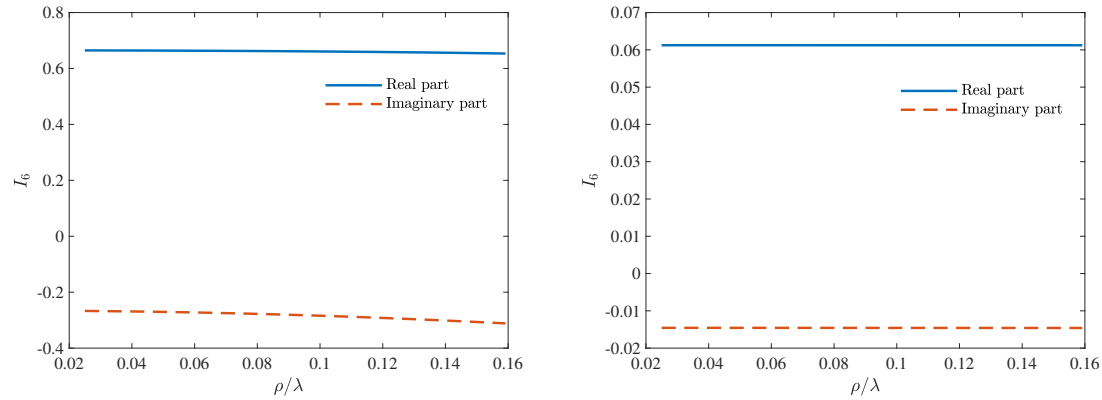

(a) (b)

Fig. 3.3: The real and imaginary parts of I_6 for $a = 2$ m at a) 10 MHz and b) 10 GHz.

be calculated for different z coordinates of the observation points and antenna heights based on the approximate closed-form formulations developed in Appendix A. These coefficients have been acquired for some different coordinates of the observation points

z and antenna heights h as shown in Table 3.1.

Table 3.1: Coefficients of the Bessel series function in (3.32) for different a values

Coefficients	$a = 1$ m	$a = 2$ m	$a = 5$ m	$a = 10$ m
a_1	-2.40	-4.40	-3.70	-2.10
b_1	-1.00	-0.96	-0.90	-1.00
c_1	-0.05	-3.60	-3.50	-0.30
a_2	-0.70	-5.00	-4.10	-2.50
b_2	-1.00	-0.97	-0.90	-1.00
c_2	2.40	-0.60	-0.40	-3.10
a_3	-4.20	-5.40	-0.60	0.80
b_3	-1.00	-0.98	-0.90	-1.00
c_3	-3.60	-4.20	1.00	-0.90
a_4	-5.20	-4.60	0.05	0.30
b_4	-1.00	-1.00	-1.00	-1.00
c_4	-0.70	-0.70	1.00	1.20

By substituting the proposed approximate closed-form solutions of I_5 and I_6, presented in (3.31) and (3.32), respectively, into (3.14), the solution of the intermediate Hertz potential in the near-field region can be obtained as

$$\Pi_z = \frac{1}{4\pi}\left[\frac{e^{-jk_0R_0}}{R_0} + \frac{e^{-jk_0R_1}}{R_1}\left(1 - \frac{2}{R_1\left(1-\eta_{01}^4\right)}\right) - 2\frac{j\eta_{01}^3 k_0}{\eta_{01}^4 - 1}\left(I_5 + I_6\right)\right]. \tag{3.33}$$

In order to calculate the scattered electric components over the lossy half-space, the intermediate Hertz potential (3.33) is inserted into (2.27). Thus, the scattered

electric field components become

$$\vec{E} = \frac{I\Delta l}{j4\pi\omega\epsilon_0}\Bigg[\frac{e^{-jk_0R_0}}{R_0^5}A_0 - \frac{e^{-jk_0R_1}}{R_1^5}\frac{1+\eta_{01}^4}{1-\eta_{01}^4}B_0 + \frac{e^{-jk_0R_1}}{R_1^3}\frac{j2\eta_{01}^3k_0}{(\eta_{01}^4-1)^2}(1+jk_0R_1)\Bigg]$$
$$(x\hat{\mathrm{x}}+y\hat{\mathrm{y}}) + \frac{I\Delta l}{j4\pi\omega\epsilon_0}\Bigg[4\pi k_0^2\Pi_z + \frac{e^{-jk_0R_0}}{R_0^6}A_1 + \frac{e^{-jk_0R_1}}{R_1^6}\Big[\frac{1+\eta_{01}^4}{\eta_{01}^4-1}B_1$$
$$- 2\frac{j\eta_{01}^3k_0}{\eta_{01}^4-1}R_1^3(z+h)(1+jk_0R_1)\Big]\Bigg]\hat{\mathbf{z}} \tag{3.34}$$

in which A_0, B_0, A_1 and B_1 are defined as

$$\begin{aligned}
A_0 =& (h-z)\left[R_0^2k_0^2 - 3\left(1+jk_0R_0\right)\right]\\
B_0 =& (h+z)\left[R_1^2k_0^2 - 3\left(1+jk_0R_1\right)\right]\\
A_1 =& \left(1+jk_0R_0\right)\left[-R_0^3 + jk_0R_0^2(z-h)^2 + 3R_0(z-h)^2\right] - jk_0R_0^2(z-h)^2\\
B_1 =& \left(1+jk_0R_1\right)\left[R_1^3 - jk_0R_1^2(z+h)^2 - 3R_1(z+h)^2\right] + jk_0R_1^2(z+h)^2.
\end{aligned} \tag{3.35}$$

3.2.3 Far-Field Region

Evaluation of the scattered electric field components in the far-field region, in which the horizontal distance between the source and the observation point is much greater than the free space wavelength (i.e., $k_0\rho >> 1$), is important as it has been widely applied in medical imaging [85], geophysics [86], remote sensing [4] and wireless communications [87]. In the same manner as the near-field evaluation, the intermediate Hertz potential (3.2) along with (3.14) are calculated in the far-field region and then (2.27) is adopted for calculating the scattered electric field components. In order to

evaluate the scattered electric field, I_5 in (3.25) and I_6 in (3.26) should be evaluated in the far-field region. After evaluating I_5 and I_6, P in (3.14) can be expressed in closed-form. Then, the intermediate Hertz potential (3.2) and scattered electric fields in (2.27) can be obtained in the far-field region.

I_5 can be split up into three integrals according to the behaviour of the integrand at various k values. For $0 < k < 1/\rho$, the small argument approximation for the Bessel function of the first kind is adopted since its argument is less than one in the interval, while for $1/\rho < k < k_0$ and $1/\rho < k < k_0$ the large argument approximation of the Bessel function is employed as a result of the fact that its argument is greater than one in the aforementioned intervals. Consequently, I_5 can be divided into three parts as

$$\begin{aligned} I_5 = \frac{1}{2}\int_0^{1/\rho} \frac{e^{-j(z+h)\sqrt{k_0^2-k^2}}}{k+k_0}\,\cos(0.7k\rho)\,dk + \frac{1}{\sqrt{2\pi\rho}}\int_{1/\rho}^{k_0} \frac{e^{-j(z+h)\sqrt{k_0^2-k^2}}}{\sqrt{k}(k+k_0)} \\ \times \cos(k\rho-\pi/4)\,dk + \frac{1}{\sqrt{2\pi\rho}}\int_{k_0}^{\infty} \frac{e^{-(z+h)\sqrt{k^2-k_0^2}}}{\sqrt{k}(k+k_0)}\,\cos(k\rho-\pi/4)\,dk. \end{aligned} \tag{3.36}$$

For $0 < k < 1/\rho$ and $1/\rho < k < k_0$, the term of $\sqrt{k_0^2-k^2}$ can be approximated by a second-degree polynomial. Moreover, for $0 < k < 1/\rho$ the rational function $\dfrac{1}{k+k_0}$ can be represented by an exponential, and for $1/\rho < k < k_0$ the function $\dfrac{1}{\sqrt{k}(k+k_0)}$ inside the integral can be approximated by an exponential. Also, in the last part of the integral in (3.36), the integrand $\dfrac{e^{-(z+h)\sqrt{k^2-k_0^2}}}{\sqrt{k}}$ can be modelled by a rational function. Therefore, the following approximations can be proposed for the integrands

of I_5 at corresponding intervals of k.

$$\begin{aligned}
0 < k < 1/\rho: \quad & \sqrt{k_0^2 - k^2} \simeq p_{10}k^2 + p_{11}k + p_{12} \\
& \frac{1}{k + k_0} \simeq p_{13}\exp(p_{14}k) \\
1/\rho < k < k_0: \quad & \sqrt{k_0^2 - k^2} \simeq p_{15}k^2 + p_{16}k + p_{17} \\
& \frac{1}{\sqrt{k}(k + k_0)} \simeq p_{18}\exp(p_{19}k) \\
k_0 < k < k_u: \quad & \frac{e^{-(z+h)\sqrt{k^2 - k_0^2}}}{\sqrt{k}} \simeq \frac{p_{20}}{k + p_{21}}.
\end{aligned} \tag{3.37}$$

The integral is not calculated when $|k|$ is greater than k_u because the integrand decays quickly when the value of k is greater than k_0, and after the value of k_u, the integrand can be assumed to be zero. To represent an accurate approximation for the integrand in the first interval of (3.37), the interval is divided into four sections, and the first, second and third points are chosen to fit the second-degree polynomial function to the original one. The first and third quarter points are selected to approximate the rational function with an exponential function in the first interval. In the second interval of (3.37), three points are required to approximate the radical and rational functions. Thus, the first, second and third quarter points are selected within the interval to fit the proposed functions into the original function. Lastly, for the third interval, the first and the third quarter points are chosen to approximate the function using a rational function. Thus, all the coefficients in (3.37) can be expressed in terms of the wave number, z coordinate of the observation point, antenna height and the

horizontal distance between the source and the observation point as follows:

$$
\begin{aligned}
p_{10} =& 8\rho^2\left(A_2-2A_3+A_4\right),\ p_{11}=-2\rho\left(5A_2-8A_3+3A_4\right), p_{12}=3A_2-3A_3+A_4,\\
p_{13} =& \frac{1}{k_0}\left(\frac{4k_0\rho+3}{4k_0\rho+1}\right)^{1.5}, p_{14}=-2\rho\ln\left(\frac{4k_0\rho+3}{4k_0\rho+1}\right),\ A_2=\frac{(16k_0^2\rho^2-1)^{0.5}}{4\rho},\\
A_3 =& \frac{(4k_0^2\rho^2-1)^{0.5}}{2\rho},\ A_4=\frac{(16k_0^2\rho^2-9)^{0.5}}{4\rho}, x_2=\frac{\rho k_0+1}{2\rho},\ x_3=\frac{3\rho k_0+1}{4\rho},\\
x_4 =& \frac{k_u+3k_0}{4}, p_{15}=\frac{1}{A_5}\left(f_2x_2-f_3x_1-f_2x_3+f_4x_1+f_3x_3-f_4x_2\right), x_1=\frac{\rho k_0+3}{4\rho},
\end{aligned}
$$

$$
\begin{aligned}
p_{16} =& \frac{-1}{A_5}\left(f_2x_2^2-f_3x_1^2-f_2x_3^2+f_4x_1^2+f_3x_3^2-f_4x_2^2\right), f_2=\sqrt{k_0^2-x_1^2}, f_3=\sqrt{k_0^2-x_2^2},\\
p_{17} =& \frac{-1}{A_5}(-f_4x_1^2x_2+f_3x_1^2x_3+f_4x_1x_2^2-f_3x_1x_3^2-f_2x_2^2x_3+f_2x_2x_3^2), f_4=\sqrt{k_0^2-x_2^2},\\
A_5 =& (x_1-x_2)(x_1-x_3)(x_2-x_3), p_{18}=f_5\exp(-p_{19}x_1), p_{19}=\frac{\ln\left(f_5/f_6\right)}{x_1-x_3},\\
f_5 =& \frac{1}{\sqrt{x_1}(x_1+k_0)},\ f_6=\frac{1}{\sqrt{x_3}(x_3+k_0)}, p_{21}=\frac{f_7x_4-f_8x_5}{f_8-f_7},\ p_{20}=f_7(x_4+p_{21}),\\
x_5 =& \frac{3k_u+k_0}{4}, f_7=\frac{\exp(-a\sqrt{x_4^2-k_0^2})}{\sqrt{x_4}}, f_8=\frac{\exp(-a\sqrt{x_5^2-k_0^2})}{\sqrt{x_5}}.
\end{aligned}
\tag{3.38}
$$

By using the proposed approximations in (3.37) along with (3.38) and substituting in (3.36) and performing the integral, the approximate closed-form solution for I_5 can be acquired in the far-field region as

$$
\begin{aligned}
I_5 \simeq & \frac{\sqrt{\pi} p_{12} e^{-jap_{11}}}{8\sqrt{ja}\sqrt{p_9}} \Bigg[\exp\left(\frac{\left(0.7j\rho - p_{13} + jap_{10}\right)^2}{j4ap_9} \right) \Bigg[\operatorname{erf}\left(\frac{ja\left(2p_9/\rho + p_{10}\right) + 0.7j\rho - p_{13}}{2\sqrt{ja}\sqrt{p_9}} \right) \\
& - \operatorname{erf}\left(\frac{jap_{10} + 0.7j\rho - p_{13}}{2\sqrt{ja}\sqrt{p_9}} \right) \Bigg] + \exp \frac{\left(0.7j\rho + p_{13} - jap_{10}\right)^2}{j4ap_9} \\
& \Bigg[\operatorname{erf}\left(\frac{ja\left(2p_9/\rho + p_{10}\right) - 0.7j\rho - p_{13}}{2\sqrt{ja}\sqrt{p_9}} \right) - \operatorname{erf}\left(\frac{jap_{10} - 0.7j\rho - p_{13}}{2\sqrt{ja}\sqrt{p_9}} \right) \Bigg] \Bigg] \\
& + \frac{p_{17} e^{-jap_{16}}}{8\sqrt{ja\rho p_{14}}} \Bigg[(j+1) \exp \frac{\left(j\rho - p_{18} + jap_{15}\right)^2}{j4ap_{14}} \Bigg[\operatorname{erf}\left(\frac{ja\left(2p_{14}k_0 + p_{15}\right) + j\rho - p_{18}}{2\sqrt{ja}\sqrt{p_{14}}} \right) \\
& - \operatorname{erf}\left(\frac{ja\left(2p_{14}/\rho + p_{15}\right) + j\rho - p_{18}}{2\sqrt{ja}\sqrt{p_{14}}} \right) \Bigg] - (j-1) \exp \frac{\left(j\rho + p_{18} - jap_{15}\right)^2}{j4ap_{14}} \\
& \Bigg[\operatorname{erf}\left(\frac{ja\left(2p_{14}k_0 + p_{15}\right) - j\rho - p_{18}}{2\sqrt{ja}\sqrt{p_{14}}} \right) - \operatorname{erf}\left(\frac{ja\left(2p_{14}/\rho + p_{15}\right) - j\rho - p_{18}}{2\sqrt{ja}\sqrt{p_{14}}} \right) \Bigg] \\
& + \frac{p_{19}}{(p_{20} - k_0)\sqrt{2\pi\rho}} \Bigg[- \sin(p_{20}\rho + \pi/4) \left[\frac{\pi}{2} - \operatorname{Si}(\rho k_0 + \rho p_{20}) \right] + \cos(p_{20}\rho + \pi/4) \\
& \operatorname{Ci}(\rho k_0 + \rho p_{20}) + \sin(k_0\rho + \pi/4) \left[\frac{\pi}{2} - \sin(2k_0\rho) \right] - \cos(k_0\rho + \pi/4) \operatorname{Ci}(2\rho k_0) \Bigg].
\end{aligned}
\tag{3.39}
$$

By using the proposed approximate closed-form solution for I_5 and I_6 in the far-field region, the intermediate Hertz potential in the far-field zone is calculated. Therefore, we obtain

$$
\Pi_z = \frac{1}{4\pi} \left[\frac{e^{-jk_0R_0}}{R_0} + \frac{e^{-jk_0R_1}}{R_1} \left(1 - \frac{2}{R_1\left(1 - \eta_{01}^4\right)} \right) - 2\frac{j\eta_{01}^3 k_0}{\eta_{01}^4 - 1} \left(I_5 + I_6 \right) \right]. \tag{3.40}
$$

It should be noted that the scattered electric field components in the far-field region have the same formulation as (3.34) except the intermediate Hertz potential, which should be replaced by (3.40).

3.3 Results

In order to evaluate the accuracy of the proposed approximate closed-form solutions for the intermediate Hertz potential and the scattered electric field, the NRMSE is employed, while the numerical computation of the Sommerfeld integrals is considered as reference. The NRMSE value in (2.55) is calculated for various frequencies and distances from the antenna, while the observation point is changed in the near and far-field regions. In the near-field, the observation point is changed between 0 to $\lambda_0/(2\pi)$, in which λ_0 represents the wavelength of the source. For the far-field transition region, the distance of the observation point from the antenna is changed between $\lambda_0/(2\pi)$ to $10\lambda_0$. In this calculation, at each observation point, in either the near or far-field regions, the NRMSE is calculated for the whole frequency range, which is between 10 MHz to 10 GHz. Moreover, in order to obtain the accuracy of the proposed solution in terms of frequency, the NRMSE value is calculated at each frequency while the observation point is changed in the whole distance range of the near and far field.

Four different problems have been selected for analysis, with the parameters listed in Table 3.2. It should be noted that the relative permittivity and permeability in Table 3.2 do not depend on the frequency. Also, f_1 and f_2 in Table 3.2 correspond to 10 MHz and 10 GHz, respectively. The scattered electric field components are calculated over the four media, i.e. seawater, wet earth, dry earth and lake water, using the proposed solutions in the near and far-field regions, and are compared with the King

Table 3.2: Media characteristics

Parameters	Seawater	Wet earth	Dry earth	Lake water
σ (S/m)	4.00	0.40	0.04	4×10^{-3}
ϵ_r	80.00	12.00	8.00	80.00
$\lvert\eta_{01}^2(f_1)\rvert$	7193.90	719.44	72.38	80.32
$\lvert\eta_{01}^2(f_2)\rvert$	80.32	12.02	8.00	80.00
$\tan\delta(f_1)$	89.91	59.94	9.00	0.09
$\tan\delta(f_2)$	0.09	0.06	9×10^{-3}	9×10^{-5}
$\lvert\nu^2(f_1)\rvert$	1	1	0.99	0.99
$\lvert\nu^2(f_2)\rvert$	0.99	0.92	0.9	0.98
$\angle\nu^2(f_1)$	-1.39×10^{-4}	-0.0014	-0.013	-0.001
$\angle\nu^2(f_2)$	-0.0011	-0.0046	-0.001	-1.1×10^{-6}

and Norton-Bannister formulations while the numerical integral computations are considered as reference. As seen in Table 3.2, the value of $|\nu^2|$ in low and high frequencies and different layer properties is around one, which is consistent with the results obtained in (3.10) and (3.11). Also, the value of the loss tangent at 10 MHz shows that all media, except lake water, act as good conductors in low frequencies since the loss tangent is greater than one, and they act as good dielectrics in high frequencies because the loss tangent is less than one. Lake water acts as a good dielectric in the whole frequency range according to the value of the loss tangent in Table 3.2. Two sets of the antenna height and z coordinate of the observation point are chosen in the evaluation of the scattered electric field. For the cases of on boundary source and observation point, which has been derived in Section 3.2.1, the antenna height and z coordinate of the observation point are assumed to be zero, while for a general scattering problems, they are both taken as 0.5 m as example.

3.3.1 Near-Field Evaluation

In this section, the scattered electric field components are evaluated in the near-field region when the dipole antenna is located over the different media mentioned in Table 3.2. Fig. 3.4 shows the NRMSE value of the proposed approximate closed-form solution for the magnitude of the scattered electric field obtained by (3.41) in the near-field region in terms of frequency and distance from the antenna when the antenna height and z coordinate of the observation point are both 0.5 m.

$$|E| = \left(|E_x|^2 + |E_y|^2 + |E_z|^2\right)^{1/2} \tag{3.41}$$

As can be seen in Fig. 3.4(a), the NRMSE value of the proposed approximate closed-form solution is better than 0.026 and also better than the King and Norton-Bannister solutions in the whole frequency range. Fig. 3.4(b) depicts the value of NRMSE for the proposed solution and its comparison with the King and Norton-Bannister solutions at various distances from the antenna in the near-field region. As is evident, the NRMSE is better than 0.028 and is better than the conventional methods in all horizontal distances from the antenna in the near-field region. Furthermore, at high frequencies where higher accuracy is required (according to the radar equation for the received power), the accuracy of the proposed solution is improved and returns more accurate results than the conventional solutions, which has a constant accuracy over all the frequencies.

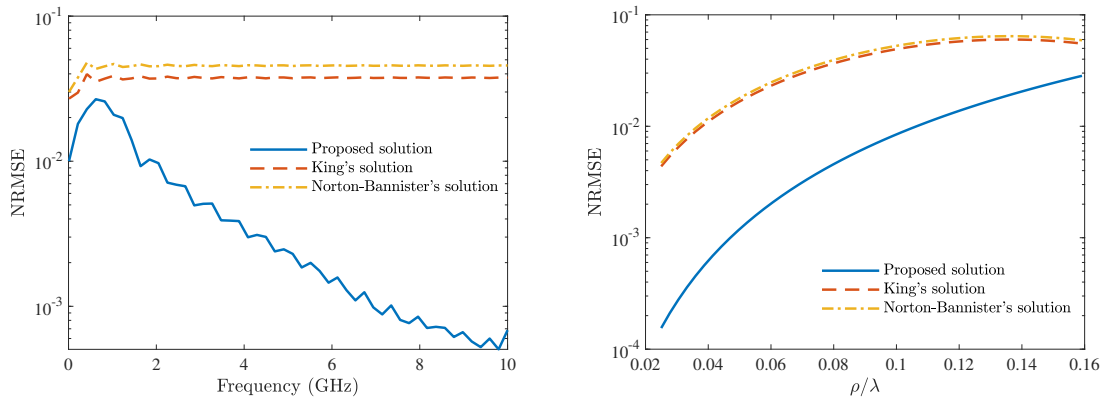

Fig. 3.4: Comparison between the proposed, King and Norton-Bannister solutions for seawater at various (a) frequencies and (b) distances from the antenna in the near field region when $a = 1$ m.

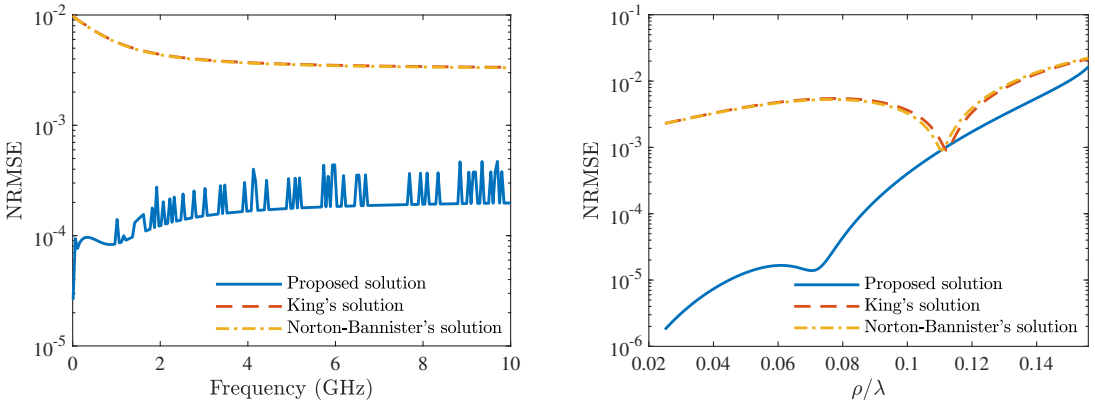

Fig. 3.5: Comparison between the proposed, King and Norton-Bannister solutions over seawater at various (a) frequencies and (b) distances from the antenna in the near field region when $a = 0$ m.

Fig. 3.5 depicts the NRMSE value of the proposed solution and its comparison with the conventional methods for the scattered electric field in the particular scattering problem, where the antenna and the observation point are at the interface. As we can see in Fig. 3.5(a), the proposed solution performs better than the conventional

methods in terms of NRMSE and is less than 0.0004 in the whole frequency range. In order to evaluate the accuracy of the proposed solution in terms of distance from the antenna for this particular case of scattering, the NRMSE is calculated in each horizontal distance while the frequency is changed between 10 MHz and 10 GHz, as shown in Fig. 3.5(b). As the figure demonstrates, the proposed solution outperforms the conventional methods at various distances from the antenna and the value of NRMSE is better than 0.016. It should be noted that the proposed approximations for the integrand of P depend on frequency due to the points defined in each integral limits and these points generate a choppy curve for the NRMSE at different frequencies shown in Fig. 3.5(a). In order to assess the accuracy of the proposed solution for moderate contrast media, the NRMSE value is obtained in terms of varying frequency and distance from the antenna for dry earth, as shown in Fig. 3.6. In this figure, the NRMSE values of the proposed solution are less than those of the King and Norton-Bannister solutions not only at various frequencies, but also at different distances from the antenna. These plots substantiate that the proposed solution performs better than the conventional solutions even for moderate contrast media, in which the reflection coefficient becomes smaller compared with high media contrast.

In order to quantify the validity of the proposed solution for different layer properties mentioned in Table 3.2, some measures of accuracy are obtained in the near-field region for the scattered electric field when $a = 1$ m, as shown in Table 3.3. The NRMSE and the mean absolute error (MAE) presented in (3.42) have been chosen to

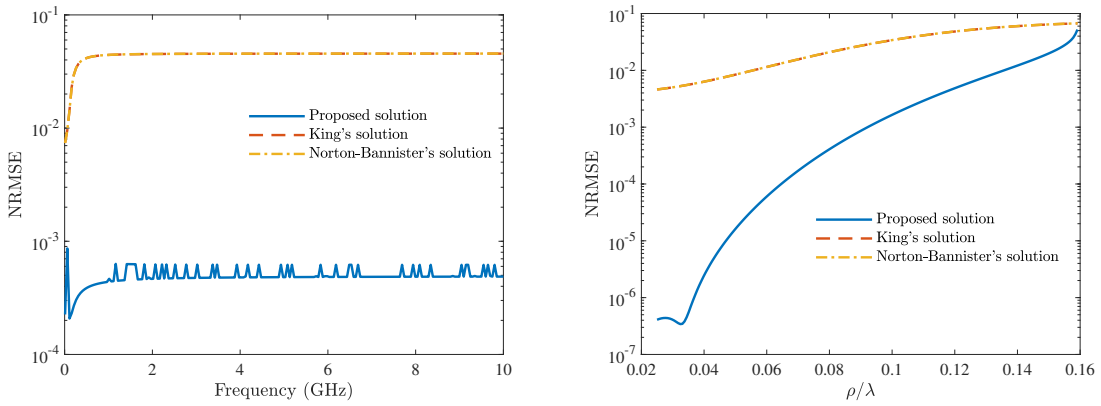

Fig. 3.6: Comparison between the proposed, King and Norton-Bannister solutions over dry earth at various (a) frequencies and (b) distances from the antenna in the near-field region when $a = 0$ m.

Table 3.3: Performance comparison between the proposed and conventional methods in the near field region

Method		Seawater		Wet earth		Dry earth		Lake water	
		NRMSE	MAE (V/m)	NRMSE	MAE (V/m)	NRMSE	MAE (V/m)	NRMSE	MAE (V/m)
Proposed solution	E(f)	0.005	0.155	0.016	0.406	0.022	0.503	0.008	0.157
	E(ρ)	0.009	0.178	0.024	0.466	0.030	0.581	0.009	0.181
King	E(f)	0.037	1.147	0.037	1.142	0.037	1.143	0.037	1.082
	E(ρ)	0.039	1.317	0.039	1.325	0.039	1.212	0.039	1.324
Norton-Bannister	E(f)	0.045	1.395	0.045	1.383	0.045	1.391	0.045	1.320
	E(ρ)	0.042	1.312	0.042	1.324	0.042	1.312	0.042	1.305

quantify the accuracy of the solutions for different layer properties with respect to the frequency (E(f)) and the distance from the antenna (E(ρ)), where MAE is calculated by

$$\text{MAE} = \frac{\sum_{i=1}^{n} |\chi_i - \hat{\chi}_i|}{n} \tag{3.42}$$

in which χ represents the reference values, $\hat{\chi}$ denotes the calculated values and n is

the number of reference or calculated values.

As can be seen in this table, the NRMSE and MAE values of the proposed method are better than the conventional methods for different layer properties.

3.3.2 Far-Field Evaluation

The NRMSE is also used to evaluate the accuracy of the proposed solution in the far-field region obtained in Section 3.2.3. Fig. 3.7 shows the NRMSE comparison of the proposed solution with the conventional methods when the dipole antenna has been located over seawater with $a = 1$ m.

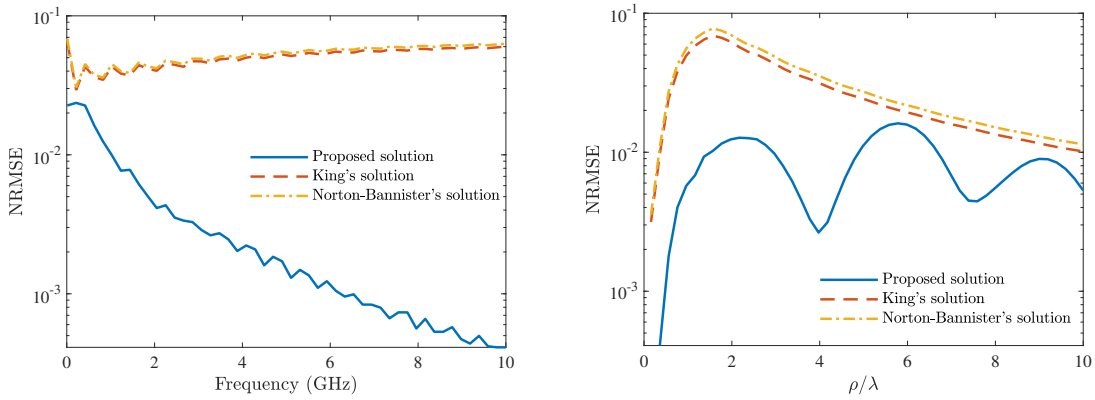

Fig. 3.7: Comparison between the proposed, King and Norton-Bannister solutions for seawater at various (a) frequencies and (b) distances from the antenna in the far-field region when $a = 1$ m.

As can be seen in Fig. 3.7(a), the NRMSE value of the proposed solution is better than 0.023 and better than the conventional methods in the whole frequency range in the far-field region. In terms of distance from the antenna, the NRMSE of the

proposed solution is less than 0.015 and better than the conventional methods in the far-field region as shown in Fig. 3.7(b). As it is evident, the proposed solution outperforms the conventional methods in the far-field region in terms of frequency and distance from the antenna.

Fig. 3.8 shows the NRMSE comparison between the proposed solution and the conventional methods for the particular scattering problem over seawater ($a = 0$ m). As we can see in Fig. 3.8(a), the proposed solution has a better accuracy in the whole frequency range and the NRMSE value is less than 0.024. In Fig. 3.8(b), the NRMSE value has been obtained at various distances from the antenna, while the frequency is changed from 10 MHz to 10 GHz at each distance. The figure shows that, the proposed solution has lower NRMSE values and outperforms the conventional methods in the far-field region. In order to evaluate the efficiency of the proposed solution in the calculation of the scattered electric field components over moderate contrast media, the NRMSE value is calculated over dry earth at various frequencies and distances from the antenna. Fig. 3.9 shows the accuracy comparison between the proposed and conventional solutions for dry earth, as moderate contrast media, when $a = 0$ m. As can be seen from the figure, the proposed solution has accuracy that is better than the conventional methods in the whole frequency range and various distances from the antenna in the far-field region.

Table 3.4 shows the performance of the proposed approximate closed-form solution for the scattered electric field in the far-field region and its comparison with other

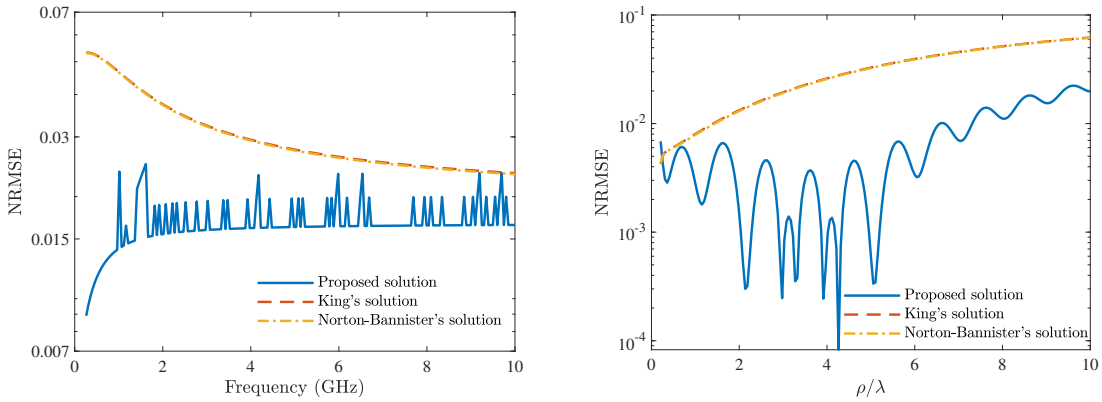

(a) (b)

Fig. 3.8: Comparison between the proposed, King and Norton-Bannister solutions for seawater at various (a) frequencies and (b) distances from the antenna in the far-field region when $a = 0$ m.

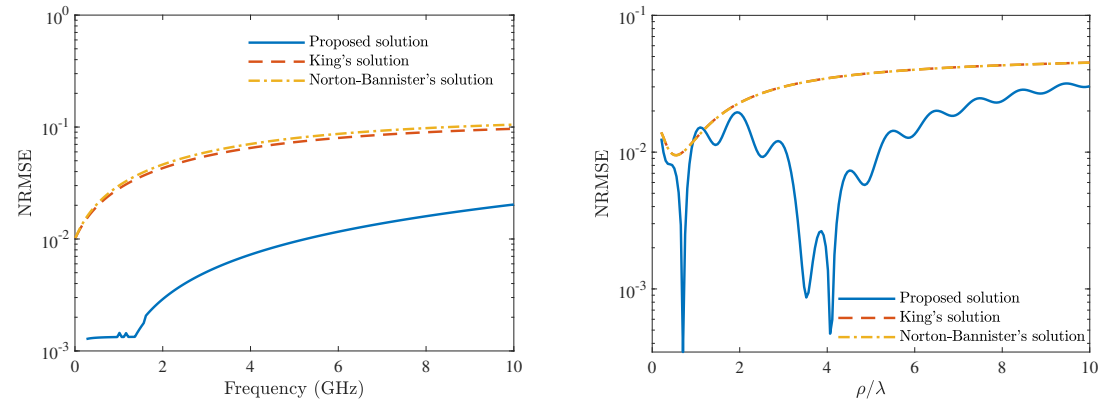

(a) (b)

Fig. 3.9: Comparison between the proposed, King and Norton-Bannister solutions over dry earth at various (a) frequencies and (b) distances from the antenna in the far-field region when $a = 0$ m.

methods. With regard to the accuracy metrics, the proposed solution is the most accurate method for different layer properties since it has the lowest NRMSE and MAE values compared with other methods.

To evaluate the contribution of the interface between the top and bottom half-

Table 3.4: Performance comparison between the proposed and conventional methods in the far field region

Method		Seawater		Wet earth		Dry earth		Lake water	
		NRMSE	MAE (V/m)	NRMSE	MAE (V/m)	NRMSE	MAE (V/m)	NRMSE	MAE (V/m)
Proposed solution	E(f)	0.004	0.110	0.004	0.143	0.005	0.153	0.001	0.108
	E(ρ)	0.005	0.148	0.008	0.162	0.009	0.164	0.004	0.147
King	E(f)	0.054	1.424	0.050	1.410	0.049	0.408	0.054	1.411
	E(ρ)	0.027	0.588	0.020	0.561	0.018	0.558	0.027	0.583
Norton-Bannister	E(f)	0.057	1.481	0.053	1.431	0.051	1.412	0.057	1.480
	E(ρ)	0.030	0.610	0.022	0.571	0.020	0.563	0.029	0.587

space on the pattern of the scattered electric field in the far-field region, the corresponding elevation pattern of $|E| = (|E_x|^2 + |E_y|^2 + |E_z|^2)^{1/2}$ is computed over seawater, as the case of high contrast media, and dry earth, as the case of moderate contrast media, for two different frequencies using the reference solution, which is the numerical method, and the proposed solution. Figs. 3.10(a) and (b), respectively, show the elevation patterns of the scattered electric field over seawater at 10 MHz and 10 GHz when the antenna height is 5 m and the distance between the origin of the Cartesian coordinate and the observation point is $50/k_0$. As is evident in the figure, the proposed solution has good agreement with the numerical method in both low and high frequencies. Furthermore, as the frequency increases, blind zones occur over the interface due to multipath fading [1]. Figs. 3.10(c) and (d), respectively, depict the elevation pattern of the scattered electric field over dry earth under same conditions. As we can see, the proposed solution also agrees well with the numerical solution in high and low frequencies. It is worth mentioning that the contribution

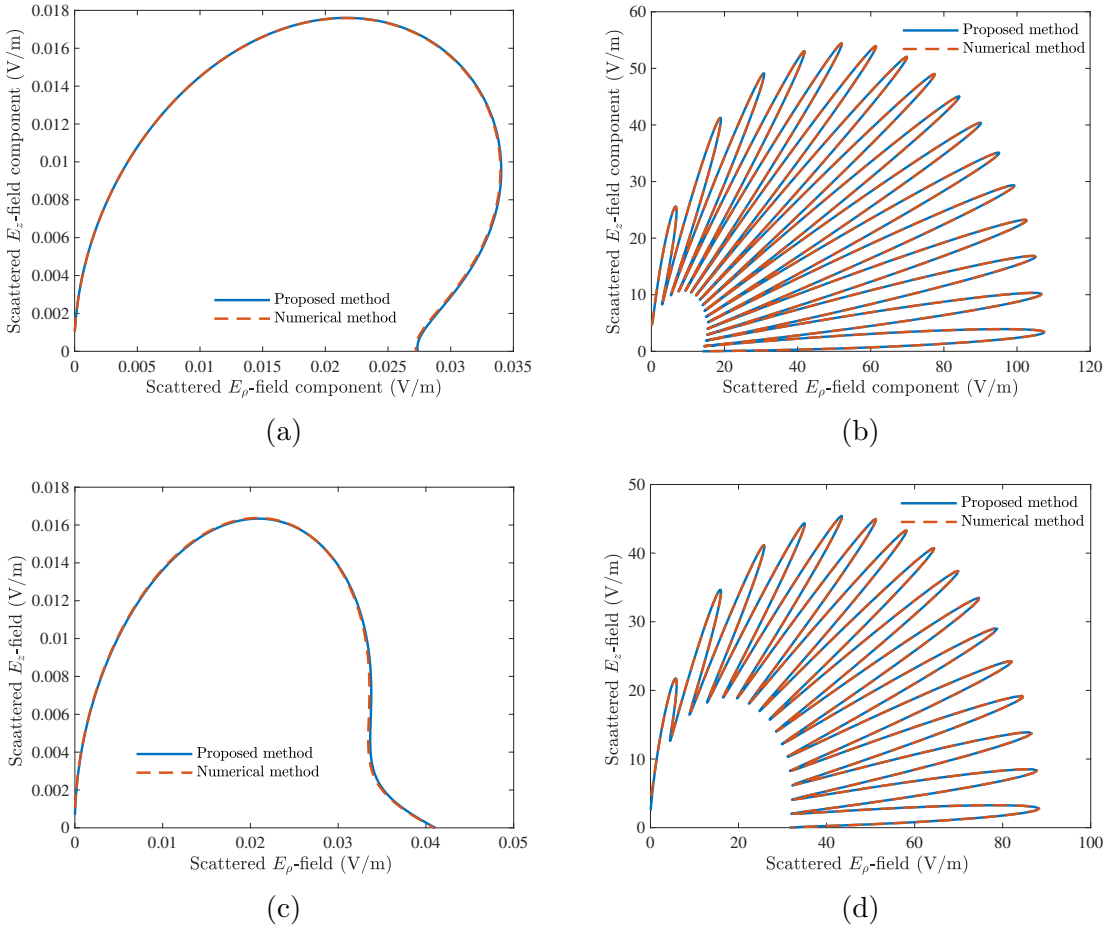

Fig. 3.10: Elevation pattern of the scattered electric field. (a) Over seawater at 10 MHz. (b) Over seawater at 10 GHz. (c) Over dry earth at 10 MHz. (d) Over dry earth at 10 GHz.

of the surface wave is relatively high in dry earth case compared with seawater since the refractive index as well as the reflection coefficient of seawater is higher than dry earth.

It should be noted that the computation time using a computer equipped with a core i7-4700MQ CPU clocked at 2.40 GHz and 16 GB RAM memory for the numerical computations accomplished in Fig. 3.10 is around 1 h 54 min for each medium.

3.4 Chapter Summary

In this chapter, an analytical evaluation of the intermediate Hertz potential and the scattered electric field components in the presence of a VED over a lossy half-space with a smooth interface is proposed. The solution consists of the Sommerfeld integral evaluated in the near and far-field regions. The accuracy of the proposed solution was assessed using NRMSE and MAE in the near and far-field regions over different layer properties in the whole frequency range, from radio to microwave frequencies. The comparisons indicate that the proposed solution has higher accuracy compared with the conventional methods at various distances from the antenna and different frequencies in the whole frequency range. In many EM scattering applications, such as nondestructive testing to determine the thickness or internal structure of a test piece [88], highly accurate solutions for the scattered fields are needed.

Chapter 4

Scattered Fields Calculation With Extensions to Plasmonics

In this chapter[1], the classical Sommerfeld half-space problem with a smooth interface is reconsidered and a rigorous approximate closed-form solution for the intermediate Hertz potential and the scattered electric and magnetic field components is presented for ordinary and plasmonic media in a wide frequency range (i.e., 100 MHz to 100 GHz for non-plasmonic and 300 THz to 900 THz for plasmonic media). The scattered fields with more terms associated with high-order surface waves are characterized

[1]The content of this chapter is based on the following publication:
M. E. Nazari, W. Huang, "Asymptotic solution for the electromagnetic scattering of a vertical dipole over plasmonic and non-plasmonic half-spaces," IET Microw. Antennas Propag., vol. 15, no. 7, pp. 704-717, 2021.
This paper presents the development of the scattered E- and H-field over a lossy half-space with extensions to plasmonics.
Roles: Mr. Nazari conducted this research under the guidance of Dr. Huang and acted as the first author of the manuscript. All the contents of this paper were written by Mr. Nazari and further refined by Dr. Huang.

from the intermediate Hertz potential approximated by the modified saddle-point method. The theoretical development is validated by representative numerical results and compared with two alternative state of the art solutions referred to as the King [36] and the Norton-Bannister [25] solutions for non-plasmonic and plasmonic media. The obtained results show that the proposed solution outperforms the conventional solutions at various frequencies and distances from the antenna and even for moderate contrast media.

This chapter is organized as follows. In Section 4.1, the scattered electric and magnetic field components using the intermediate Hertz potential are derived and a rigorous approximate closed-form solution for the intermediate Hertz potential and scattered electric and magnetic field components in the far field region is proposed. In Section 4.2, numerical evaluation of the proposed solution at various frequencies and comparisons with the conventional methods, i.e., King and Norton-Bannister solutions, for both ordinary and plasmonic media are presented in terms of the NRMSE and the normalized maximum absolute error (NMAE).

4.1 Scattered Fields Calculation

The scattered electric field components radiated by a VED located on the z-axis of the cylindrical coordinate system at height h above a lossy half-space, as shown in Fig. 2.2, can be obtained from the intermediate Hertz potential mentioned in (3.2). Using Maxwell's equations, the scattered magnetic field components can be calculated

from the scattered electric field (2.27) as [18]

$$\vec{H} = I\Delta l \left[\frac{\partial \Pi_z}{\partial y}\hat{x} - \frac{\partial \Pi_z}{\partial x}\hat{y} \right]. \tag{4.1}$$

The Sommerfeld-type integral of P in (3.4) should be identified for the calculation of the scattered electric and magnetic field components. Various analytical solutions have been proposed for seeking an approximate closed-form solution for the scattered electric and magnetic field components. However, proposing a general closed-form solution for different antenna and observation point locations with an arbitrary value of the complex refractive index is the main difficulty in evaluating them.

The zero order Bessel function in (3.5) can be written as the sum of two Hankel functions of the first and second kinds with the same argument mentioned in (2.38). By substituting (2.38) into (3.5), P can be written as

$$P = \frac{1}{2}\int_{-\infty}^{\infty} k \, \frac{\frac{1}{\eta_{01}^2}\gamma_1}{\gamma_0 + \frac{1}{\eta_{01}^2}\gamma_1} \frac{e^{-(z+h)\gamma_0}}{\gamma_0} H_0^1(k\rho)\, dk. \tag{4.2}$$

For moderate and high contrast media, (4.2) can be further simplified as

$$P = \frac{1}{2}\int_{-\infty}^{+\infty} k \, \frac{\mathrm{j}k_0\beta}{\gamma_0 + \mathrm{j}k_0\beta} \frac{e^{-(z+h)\gamma_0}}{\gamma_0} H_0^1(k\rho)\, dk \tag{4.3}$$

wherein $\beta = \gamma_1/\mathrm{j}k_0\eta_{01}^2$. By changing the integral variable k to $\zeta = \arccos(k/k_0)$, P

becomes

$$\frac{\mathrm{j}k_0\beta}{2}\int_{-\mathrm{j}\infty}^{\pi+\mathrm{j}\infty}\frac{\cos\zeta\ H_0^1(k_0\rho\cos\zeta)\ e^{-\mathrm{j}k_0(z+h)\sin\zeta}}{\sin\frac{\zeta+\alpha_0}{2}\ \cos\frac{\zeta-\alpha_0}{2}}\,d\zeta \tag{4.4}$$

in which $\alpha_0 = \sin^{-1}(\beta)$. It should be noted that by representing ζ in the polar form (i.e., $e^{j\zeta} + e^{-j\zeta} = k/k_0$), the bounds of the integral in (4.4) are obtained. By using the first term of the asymptotic expansion of the Hankel function of the first kind in the far field region, (4.4) can be expressed as

$$e^{\mathrm{j}\frac{\pi}{4}}\beta\sqrt{\frac{k_0}{2\pi\rho}}\int_{-\mathrm{j}\infty}^{\pi+\mathrm{j}\infty}\frac{\sqrt{\cos\zeta}\ e^{-\mathrm{j}k_0R_1\cos(\theta_2-\zeta)}}{\sin\frac{\zeta+\alpha_0}{2}\cos\frac{\zeta-\alpha_0}{2}}d\zeta \tag{4.5}$$

where θ_2 is defined as

$$\theta_2 = -\tan^{-1}\left(\frac{z+h}{\rho}\right) = \frac{\pi}{2} + \theta_1. \tag{4.6}$$

Although extra terms for the asymptotic expansion of the Hankel function in (4.5) may increase the accuracy of the integral evaluation, it is quite accurate in the far-field region since the NRMSE values for the real and imaginary parts of the proposed approximation of the Hankel function are 0.004 and 0.0042, respectively.

By deforming the integration path via the substitution $\cos(\theta_2 - \zeta) = 1 - \mathrm{j}t^2$ and using the modified saddle-point method, P can be approximated as

$$P \approx -2\sqrt{2j}e^{-j\pi/4}e^{-\mathrm{j}k_0R_1}\cos\left((\theta_2-\alpha_0)/2\right)\int_{-\infty}^{\infty}\frac{e^{-k_0R_1t^2}dt}{t^2+\mathrm{j}2\cos^2\left((\theta_2-\alpha_0)/2\right)} \tag{4.7}$$

and finally,

$$P \simeq \mathrm{j}\sqrt{\pi P_e}\; e^{-W_e}\; \mathrm{erfc}(\mathrm{j}\sqrt{W_e})\; \frac{e^{-\mathrm{j}k_0 R_1}}{R_1} \tag{4.8}$$

in which P_e and W_e may be expressed as

$$P_e = -\frac{\mathrm{j}k_0 R_1}{2}\beta^2\,, \quad W_e \approx P_e\left(1+\frac{h+z}{\beta R_1}\right)^2. \tag{4.9}$$

4.1.1 Scattered E-field Components

In order to calculate the scattered electric field components over the lossy half-space, the intermediate Hertz potential (3.2) along with (4.8) are substituted into (2.27). The x-component of the scattered electric field may be expressed as

$$\begin{aligned}\vec{E}_x = \frac{I\Delta l}{\mathrm{j}4\pi\omega\epsilon_0}\Bigg[& x(h-z)\left[R_0^2k_0^2-3\left(1+\mathrm{j}k_0R_0\right)\right]\frac{e^{-\mathrm{j}k_0R_0}}{R_0^5} - x(h+z) \\ & \left[R_1^2k_0^2-3\left(1+\mathrm{j}k_0R_1\right)\right]\frac{e^{-\mathrm{j}k_0R_1}}{R_1^5} + \sqrt{2\pi k_0}\; e^{-\mathrm{j}\frac{3\pi}{4}}\;\beta\left[T_1\;T_2+T_3\;\mathrm{erfc}(\mathrm{j}\sqrt{W_e})-\mathrm{j}T_4\right]\Bigg]\end{aligned} \tag{4.10}$$

wherein T_1 to T_4 with their sub variables (i.e., C_1 to C_7) can be acquired from the following equations.

$$\begin{aligned} T_1 &= -\frac{k_0\beta^2 x e^{W_e}}{2R_1\sqrt{\pi W_e}}\left[1-\frac{\cos^2\theta_1}{\beta^2}\right] \\ T_2 &= -e^{-W_e}\frac{e^{-\mathrm{j}k_0R_1}}{R_1^{2.5}}\left[(\frac{1}{2}+\mathrm{j}k_0R_1)(h+z)+C_1R_1^2\right] \\ T_3 &= -2(1+\mathrm{j}k_0R_1)C_2 - \mathrm{j}k_0\; x\; e^{-W_e}\; e^{-\mathrm{j}k_0R_1}\;\frac{h+z}{R_1^{3.5}} + C_2 \end{aligned}$$

$$
\begin{aligned}
T_4 &= C_7 e^{-\mathrm{j}k_0 R_1} - \frac{\mathrm{j}k_0\, x\, C_1}{\sqrt{\pi W_e}} \frac{e^{-\mathrm{j}k_0 R_1}}{R_1^{1.5}} \\
C_1 &= -\frac{\mathrm{j}k_0 \beta^2}{2} \left(1 + \frac{\cos\theta_1}{\beta}\right) \left[\cos\theta_1 \left(1 + \frac{\cos\theta_1}{\beta}\right) + 2R_1\right] - C_4 e^{-W_e} \frac{e^{-\mathrm{j}k_0 R_1}}{R_1^{0.5}} - C_5 C_6 \\
C_2 &= -\frac{(h+z) e^{-W_e} e^{-\mathrm{j}k_0 R_1}}{2R_1^{4.5}} \left(C_3 R_1^2 + \mathrm{j}k_0 x R_1 + 2.5x\right) \\
C_3 &= \frac{-\mathrm{j}k_0 \beta^2 x}{2R_1} \left(1 - \frac{\cos^2\theta_1}{\beta^2}\right) \\
C_4 &= \frac{-\mathrm{j}k_0 x}{2R_1^2} \left[-\sin(2\theta_1)\sin\theta_1 - \cos\theta_1 \left(\beta^2 - \cos^2\theta_1\right)\right] \\
C_5 &= -\frac{\mathrm{j}k_0 \beta}{2} \left[(1+\cos\theta)\left(1 + \sin^2\theta_1 + \beta\cos\theta_1\right)\right] \\
C_6 &= \frac{e^{-W_e} e^{-\mathrm{j}k_0 R_1}}{R_1^{2.5}} \left(-R_1^2 C_3 + \frac{x}{2} - x(1 + \mathrm{j}k_0 R_1)\right) \\
C_7 &= \frac{1}{2R_1^2 W_e \sqrt{\pi R_1 W_e}} \left[2C_4 R_1^2 W_e - C_1 \left(x W_e + R_1^2 C_3\right)\right]
\end{aligned}
\tag{4.11}
$$

The y-component of the scattered electric field can be expressed as

$$
\begin{aligned}
\vec{E}_y = \frac{I\Delta l}{\mathrm{j}4\pi\omega\epsilon_0} \Bigg[& y(h-z)\left[R_0^2 k_0^2 - 3\left(1 + \mathrm{j}k_0 R_0\right)\right] \frac{e^{-\mathrm{j}k_0 R_0}}{R_0^5} - y(h+z)\Big[R_1^2 k_0^2 \\
& - 3\left(1 + \mathrm{j}k_0 R_1\right)\Big] \frac{e^{-\mathrm{j}k_0 R_1}}{R_1^5} + \sqrt{2\pi k_0}\, e^{-\mathrm{j}\frac{3\pi}{4}}\, \beta \left[T_1'\, T_2 + T_3'\, \mathrm{erfc}(\mathrm{j}\sqrt{W_e}) - \mathrm{j}T_4'\right] \Bigg].
\end{aligned}
\tag{4.12}
$$

The only difference between the prime parameters, i.e., T_1', T_2', T_3' and T_4', and unprimed parameters in (4.12) is the x parameter. In other words, by changing x to y in T_1, T_2, T_3, T_4 and their sub variables, prime parameters can be obtained. By calculating the x- and y- components of the scattered electric field over the lossy half-space, cross polarized components are obtained since the polarization of the antenna is vertical. By using (2.27), the z-component of the scattered electric field can be

calculated. Thus, we have

$$\vec{E}_z = \frac{I\Delta l}{\mathrm{j}4\pi\omega\epsilon_0}\Bigg[k_0^2\left(\frac{e^{-\mathrm{j}k_0R_0}}{R_0}+\frac{e^{-\mathrm{j}k_0R_1}}{R_1}\right)+\frac{\cos^2\theta_0\,(1+\mathrm{j}k_0R_0)\,e^{-\mathrm{j}k_0R_0}}{R_0^3}\Big(-\sec\theta_0 + \mathrm{j}k_0R_0+3-\frac{\mathrm{j}k_0R_0}{1+\mathrm{j}k_0R_0}\Big)+\frac{\cos^2\theta_1\,(1+\mathrm{j}k_0R_1)\,e^{-\mathrm{j}k_0R_1}}{R_1^3}\Big(-\sec\theta_1+\mathrm{j}k_0R_1+3 + \frac{\mathrm{j}k_0R_1}{1+\mathrm{j}k_0R_1}\Big)-2k_0^2P-2T_5\Bigg] \tag{4.13}$$

in which T_5 to T_8 and their sub variables are obtained from the following equations.

$$\begin{aligned}
T_5 &= -\sqrt{\frac{\pi k_0}{2}}e^{-\mathrm{j}\frac{3\pi}{4}}\,\beta\left[-\mathrm{j}\frac{e^{W_e}C_1}{\sqrt{\pi W_e}}\,T_6+T_7\,\mathrm{erfc}(\mathrm{j}\sqrt{W_e})-\mathrm{j}T_8\right]\\
T_6 &= -\frac{\cos\theta_1 e^{-W_e}e^{-\mathrm{j}k_0R_1}}{R_1^{1.5}}\left(\frac{1}{2}+\mathrm{j}k_0R_1+\frac{R_1C_1}{\cos\theta_1}\right)\\
T_7 &= -\,(1+2\mathrm{j}k_0R_1)\,C_8+\frac{\mathrm{j}k_0}{R_1^{1.5}}e^{-W_e}e^{-\mathrm{j}k_0R_1}\cos^2\theta_1+C_9\\
T_8 &= \frac{C_1e^{-\mathrm{j}k_0R_1}}{\sqrt{\pi R_1W_e}}\left[C_1-\mathrm{j}k_0\cos\theta_1-\frac{W_e\cos\theta_1+R_1C_1}{2R_1W_e}\right]\\
C_8 &= -\frac{e^{-\mathrm{j}k_0R_1-W_e}}{2R_1^{2.5}}\left[-1+(h+z)C_1+\cos^2\theta_1(\mathrm{j}k_0R_1+\frac{5}{2})\right]\\
C_9 &= \frac{e^{-\mathrm{j}k_0R_1-W_e}}{2R_1^{1.5}}\big[-2R_1C_{10}+2R_1C_1^2+C_1(1+2\mathrm{j}k_0R_1)\cos\theta_1\big]\\
C_{10} &= -\frac{\mathrm{j}k_0}{2R_1}\left[(1+\beta)\sin^2\theta_1\cos\theta_1+2\sin^4\theta_1+(\beta+\cos\theta_1)\left(\sin^2\theta_1-\frac{2\cos\theta_1\rho^2}{\beta R_1^2}\right)\right]
\end{aligned} \tag{4.14}$$

4.1.2 Scattered H-field Components

The scattered magnetic field components can also be calculated using the intermediate Hertz potential (3.2). In other words, by substituting (3.2) along with (4.8) into (4.1), different components of the scattered magnetic field can be obtained. The x-component of the scattered magnetic field may be expressed as

$$\vec{H}_x = -\frac{I\Delta l}{4\pi} y \Bigg[\frac{e^{-\mathrm{j}k_0 R_0}(1+\mathrm{j}k_0 R_0)}{R_0^3} + \frac{e^{-\mathrm{j}k_0 R_1}(1+\mathrm{j}k_0 R_1)}{R_1^3} - e^{\mathrm{j}\frac{\pi}{4}} e^{-\mathrm{j}k_0 R_1} \beta \sqrt{2\pi k_0} \left(\mathrm{erfc}(\mathrm{j}\sqrt{W_e}) e^{-W_e} T_9 + \frac{\mathrm{j}C_{11}}{y\sqrt{\pi W_e R_1}} \right) \Bigg] \tag{4.15}$$

wherein T_9 and C_{11} can be expressed as follows:

$$\begin{aligned} T_9 &= \frac{C_{11}}{y\sqrt{R_1}} + \frac{1+2\mathrm{j}k_0 R_1}{2R_1^{2.5}} \\ C_{11} &= -\frac{\mathrm{j}k_0 \beta^2 y}{2R_1} \left(1 - \frac{\cos^2\theta_1}{\beta^2} \right). \end{aligned} \tag{4.16}$$

The y-component of the scattered magnetic field over the lossy half-space can also be written as

$$\vec{H}_y = -\frac{I\Delta l}{4\pi} x \Bigg[\frac{e^{-\mathrm{j}k_0 R_0}(1+\mathrm{j}k_0 R_0)}{R_0^3} + \frac{e^{-\mathrm{j}k_0 R_1}(1+\mathrm{j}k_0 R_1)}{R_1^3} - e^{\mathrm{j}\frac{\pi}{4}} e^{-\mathrm{j}k_0 R_1} \beta \sqrt{2\pi k_0} \left(\frac{\mathrm{erfc}(\mathrm{j}\sqrt{W_e}) e^{-W_e}}{x} T_9' + \frac{\mathrm{j}C_3}{x\sqrt{\pi W_e R_1}} \right) \Bigg] \tag{4.17}$$

in which T_9' can be obtained by noting that C_{11} in (4.16) is the same as C_3 in (4.11) with x changed to y.

4.2 Results

In order to evaluate the accuracy and efficiency of the recently developed method for the calculation of the intermediate Hertz potential and the scattered electric and magnetic field components over the lossy half-space, the NRMSE and the normalized maximum absolute error (NMAE) (see 4.18 below), in which the standard deviation of the reference values is used for normalization [89], are utilized for each frequency. It should be noted that in the calculation of the NRMSE, the numerical solutions obtained by the high-order global adaptive quadrature method [90] are considered as reference. In order to calculate the NRMSE for each frequency using (2.55), the amplitude of the scattered electric field (i.e., $\sqrt{|E_x|^2 + |E_y|^2 + |E_z|^2}$) is considered as $\hat{\chi}$ while θ (elevation angle in Fig. 2.27) is changed between 0 to $\pi/2$ with a resolution of $\pi/200$ ($N = 100$). The numerical solution for the amplitude of the scattered electric field is also considered as χ, while θ is changed between 0 to $\pi/2$ with the resolution of $\pi/200$. The next metric used here for the accuracy evaluation of the proposed solution is the NMAE defined as the maximum difference between the proposed and numerical solutions for the scattered electric field. The normalization is accomplished by the standard deviation of the numerical results. Therefore, the NMAE can be expressed

Table 4.1: Media parameters

Parameter	Seawater	Silty loam soil	Silty clay soil	Lake water	Silver	Gold
f	300 MHz	1.8 GHz	108 MHz	9.4 GHz	351.87 THz	420.52 THz
k_0 (m^{-1})	6.28	37.7	2.26	196.87	7.36×10^6	8.8×10^6
h	0.5 m	2.5 m	1.5 m	0.5 m	48 nm	220 nm
$R(m)$	$8/k_0$	$10/k_0$	$10/k_0$	$10/k_0$	$10/k_0$	$20/k_0$
σ_0 (S/m)	4	0.04	0.012	17.51	6.3×10^6	7.2×10^6
ϵ_r	80	4.64	23.06	60.98	-36.93	-17.2
$\lvert n_{01}^2 \rvert$	252.77	4.66	23.15	69.58	36.93	17.24
$\tan\delta$	2.99	0.09	0.086	0.55	0.012	0.075

as

$$\mathrm{NMAE} = \frac{\underset{i=1,2,\ldots,N}{\mathrm{Max}} |\chi_i - \hat{\chi}_i|}{\sigma_\chi}. \tag{4.18}$$

Next, the proposed solutions for the scattered E and H fields are compared with the King and Norton-Bannister solutions, while the reference E- and H-fields are computed by the rigorous numerical computation of the integrals in P considered as SIs using the high-order global adaptive quadrature method [90]. Moreover, the elevation pattern of the scattered electric field is compared with the numerical solution. Six various media with different electromagnetic properties are selected for the accuracy evaluation of the proposed solution listed in Table 4.1. Silver and gold illustrate plasmonic media, which have been considered in the optical frequency range, and the others represent ordinary (i.e., non-plasmonic) media.

4.2.1 Non-plasmonic Media

The proposed formulations are applied to four different ordinary media listed in Table 4.1. In this table, two of the media are soil and the soil composition is characterized by the percentage of soil constituents, i.e., sand, clay, silt and water. Silty loam soil consists of roughly equal amounts of silt and sand and a little less clay. On the other hand, silty clay soil has more clay than silt. The complex relative permittivity of seawater as well as lake water are calculated using the Meissner and Wentz model [91], which is based on the double Debye model and is quite accurate at higher frequencies. On the other hand, for silty loam and silty clay soil, the complex relative permittivity is calculated by the developed Dobson model [92, 93].

The frequency carried by the antenna over each medium in Table 4.1 is related to the application of wave scattering over that region. For seawater, the VHF frequency band has been selected since pulsed radars operate in this frequency band to extract the speed and direction of ocean surface currents in real time [4, 94]. For the silty loam soil scattering problem, the global system for mobile communications (GSM) frequency band has been considered since finding the pattern of the scattered EM fields, coverage area and blind zones over earth surface are of interest [1, 95]. Therefore, GSM-1800 (1.8 GHz) has been selected for this scattering problem. On the other hand, the frequency modulation (FM) broadcast band has been selected for the silty clay soil scattering problem due to its application in finding the coverage area of passive radars and FM broadcast radio systems [96]. For radio oceanography

applications, X-band marine radar is commonly used to scan the water surface with high temporal and spatial resolutions [97], and this frequency range has been selected for the lake water scattering problem.

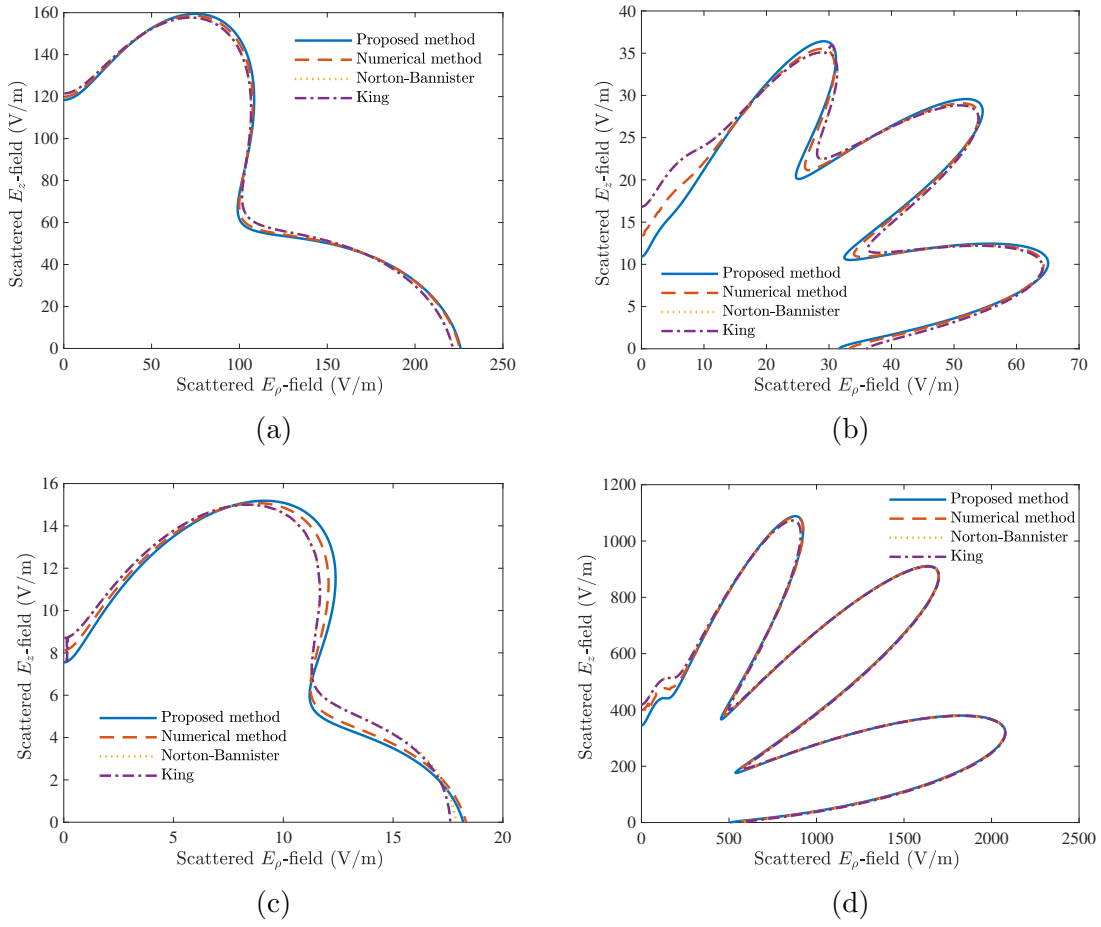

Fig. 4.1: The elevation pattern of the scattered electric field for a VED and its comparison with the proposed, Norton-Bannister and King solutions over a) seawater b) silty loam soil c) silty clay soil and d) lake water as non-plasmonic media.

The elevation pattern of the scattered electric field, i.e., $|E| = (|E_x|^2 + |E_y|^2 + |E_z|^2)^{0.5}$, over the selected ordinary media listed in Table 4.1 is calculated using the proposed method and compared with the numerical and conventional (Norton-

Banister and King solutions) methods. Fig. 4.1 depicts the elevation pattern of the scattered electric field for a VED over selected non-plasmonic media in different frequencies and distances from the antenna. The horizontal and vertical axes, respectively, correspond to $\theta = 90^\circ$ and $\theta = 0^\circ$, as shown in Fig. 2.2. As can be seen in Fig. 4.1, the King and Norton-Bannister results are close to each other and become indistinguishable when the media contrast is sufficiently high [98]. In Fig. 4.1(a), which has been obtained for seawater at VHF band, the proposed solution has a good agreement with the numerical method not only for low angles, but also near the interface, in which groundwave contribution is high. In order to evaluate the accuracy of the proposed solution compared with the conventional solutions, the NRMSE and NMAE are calculated shown in Table 4.2. As can be seen in this table, both NRMSE and NMAE of the proposed solution are lower than the conventional solutions for both scattered E and H fields. The elevation pattern of the scattered electric field over silty loam soil is shown in Fig. 4.1(b). The proposed solution follows the numerical solution, particularly on the pattern nulls and also on the interface, which corresponds to the groundwave contribution. The NRMSE and NMAE evaluation of the scattered E and H fields reveal that the proposed solution outperforms the conventional solutions even for moderate contrast media. In Fig. 4.1(c), the elevation pattern of the scattered electric field over silty clay soil has been obtained. As can be observed in this figure, the proposed solution agrees well with the numerical solution, particularly, in high angles and near the interface, and the NRMSE and NMAE values for silty clay

Table 4.2: Performance comparison between the proposed and conventional solutions for the ordinary media

Medium		Proposed solution		King		Norton-Bannister	
		NRMSE	NMAE	NRMSE	NMAE	NRMSE	NMAE
Seawater	E-field	0.0355	0.0571	0.0654	0.1317	0.0649	0.1313
	H-field	0.0064	0.0135	0.0132	0.0237	0.0112	0.0238
Silty loam soil	E-field	0.1182	0.2216	0.1459	0.2585	0.1458	0.2584
	H-field	0.0135	0.0316	0.0169	0.0452	0.0170	0.0452
Silty clay soil	E-field	0.1098	0.2028	0.1555	0.2794	0.1528	0.2780
	H-field	0.021	0.0525	0.041	0.0612	0.032	0.0610
Lake water	E-field	0.044	0.1042	0.0601	0.1218	0.0601	0.1218
	H-field	0.0287	0.0735	0.0522	0.1096	0.0522	0.1096

soil problem listed in Table 4.2 are lower than the conventional solutions. Fig. 4.1(d) illustrates the elevation pattern of the scattered electric field for lake water, in which discrepancies between results are not noticeable. However, the NRMSE and NMAE values listed in Table 4.2 substantiate that the proposed solution is more accurate than the King and Norton-Bannister solutions. Similarly, to evaluate the accuracy of the proposed solution for the scattered magnetic field, the NRMSE and NMAE values for the H-field over non-plasmonic media listed in Table 4.1 are calculated, which have been shown in Table 4.2. As evident, all the NRMSE and NMAE values for the H-fields are smaller than the conventional solutions for the ordinary media.

To assess the robustness of the proposed solution in terms of NRMSE at various frequencies, the NRMSE value is calculated for the scattered electric field components for the whole frequency range, which is between 100 MHz to 100 GHz for non-plasmonic media. In other words, the NRMSE value is calculated for each frequency (500 frequency samples) while the observation point angle is changed between

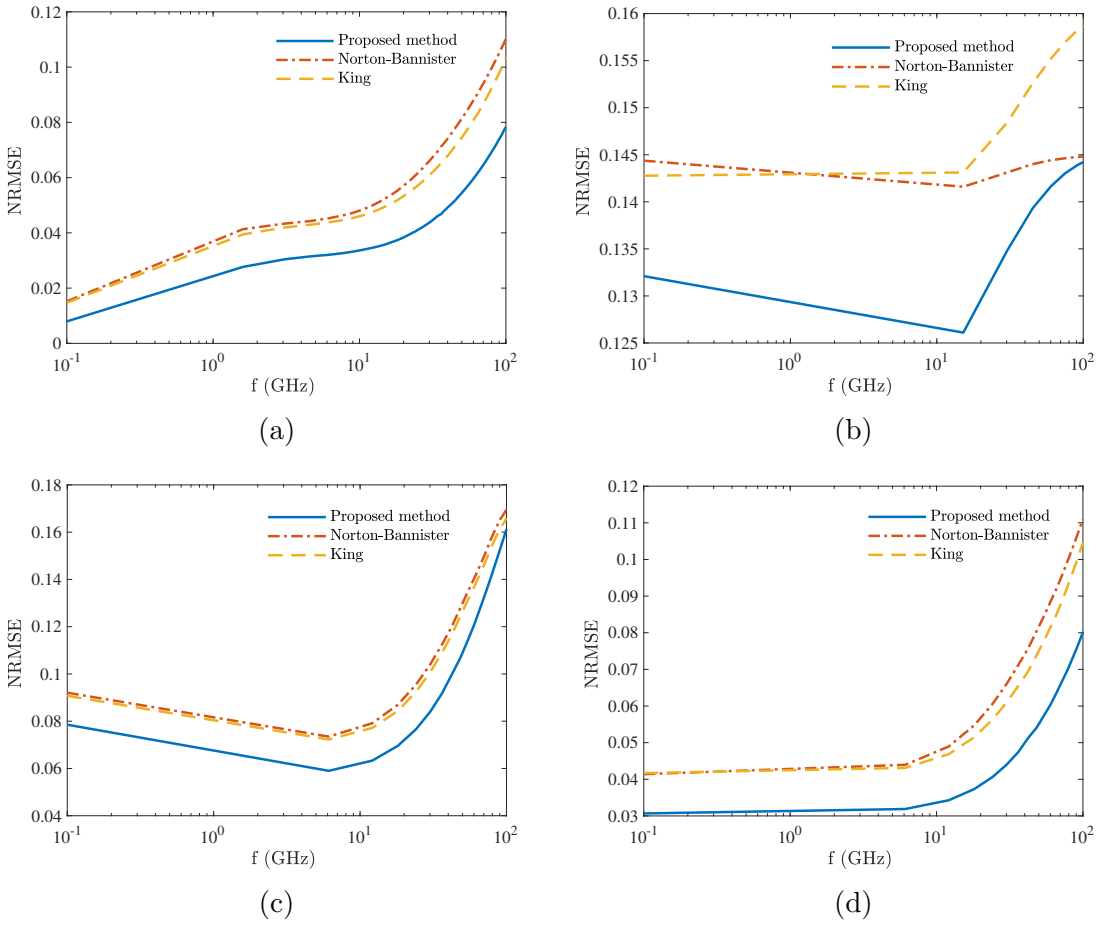

Fig. 4.2: The NRMSE of the scattered electric field for a VED at various frequencies and its comparison with the Norton-Bannister and King solutions over a) seawater b) silty loam soil c) silty clay soil and d) lake water as non-plasmonic media.

$\theta = 0°$ and $\theta = 90°$. It should be noted that the real and imaginary parts of the dielectric constant for the ordinary media listed in Table 4.1 depend on frequency. Therefore, the relative permittivity should be calculated for each frequency for the NRMSE calculation. For seawater, the relative permittivity depends on temperature and also salinity and varies with frequency [99]. In the NRMSE calculation of the scattered fields over seawater, the salinity of seawater and lake water have been as-

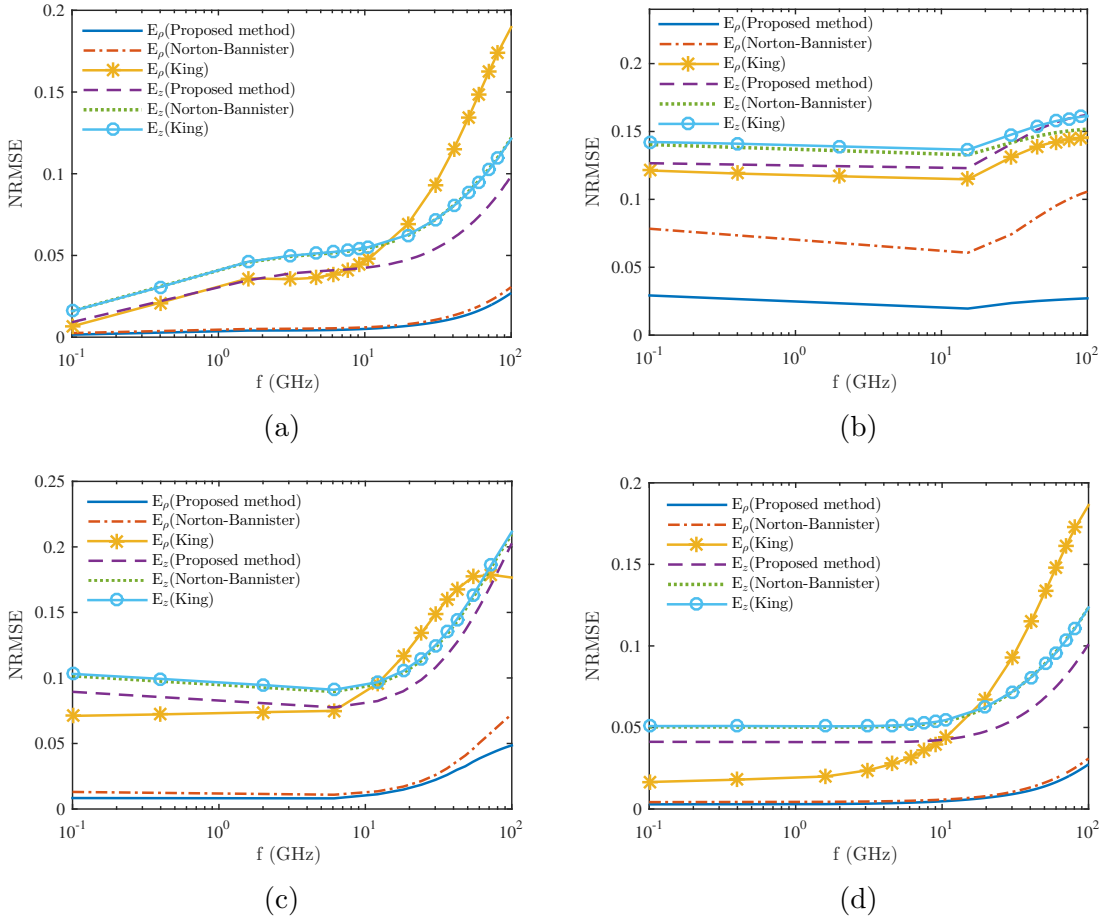

Fig. 4.3: The NRMSE comparison of each scattered electric field component for a VED at various frequencies over a) seawater b) silty loam soil c) silty clay soil and d) lake water.

sumed as 35 and 0, respectively, while the temperature is 17 °C. For the silty clay and loam soil, the relative permittivity depends on frequency, temperature and also the texture of the soil [100]. For this scattering problem, the temperature has been assumed as 23 °C.

Fig. 4.2 illustrates the NRMSE comparison of the proposed and conventional solutions over ordinary media in a wide variety of frequency ranges, while the antenna

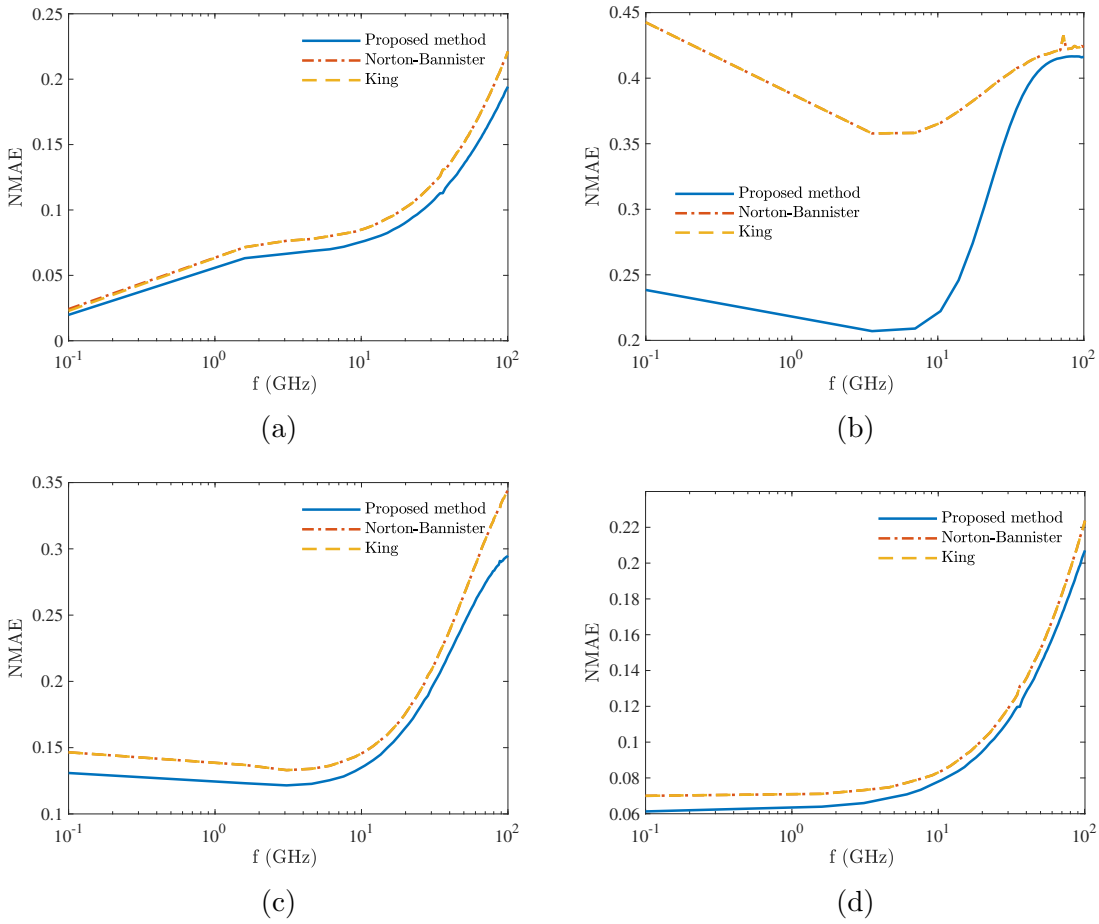

Fig. 4.4: The NMAE of the scattered electric field for a VED at various frequencies and its comparison with the Norton-Bannister and King solutions over a) seawater b) silty loam soil c) silty clay soil and d) lake water as non-plasmonic media.

height (h) and distance of the observation point from the origin of the coordinate system (R) are assumed to be $\lambda/10$ and $k_0/10$, respectively. As is obvious from this figure, the NRMSE value of the scattered electric field components is better than the conventional solutions (i.e., King and Norton-Bannister solutions) in all frequencies shown in Fig. 4.2(a) to (d). In order to evaluate the accuracy of each scattered electric field component, i.e., E_z and E_ρ, the NRMSE has been calculated

over the presented ordinary media. Fig. 4.3 shows the NRMSE comparison of the scattered electric field for each component, i.e., E_ρ and E_z, over non-plasmonic media at various frequencies. As can be seen in this figure, the E_ρ component obtained by the proposed method has better accuracy in comparison with the E_z component. In other words, the E_z component has more impact on the NRMSE value of the scattered electric field over non-plasmonic media since its NRMSE value is greater than the other component. Also, the NMAE comparison between the proposed and the conventional methods shown in Fig. 4.4 substantiates that the proposed solution outperforms the conventional solution over non-plasmonic media since the value of NMAE is better than the King and the Norton-Bannister solutions in all frequency ranges.

The evaluation of the error shown in Figs. 4.2-4.4 for non-plasmonic media indicates that the error becomes greater when the frequency increases. By increasing the frequency, the integrand in (4.5) becomes more oscillatory at the stationary phase and may deviate from the saddle-point assumption.

4.2.2 Plasmonic Media

In order to evaluate the accuracy of the proposed solution for plasmonic media, silver and gold have been considered and the elevation patterns of the scattered electric field have been compared with the numerical solutions at 351.87 and 420.52 THz for silver and gold, respectively. It should be noted that for light-matter interaction in THz

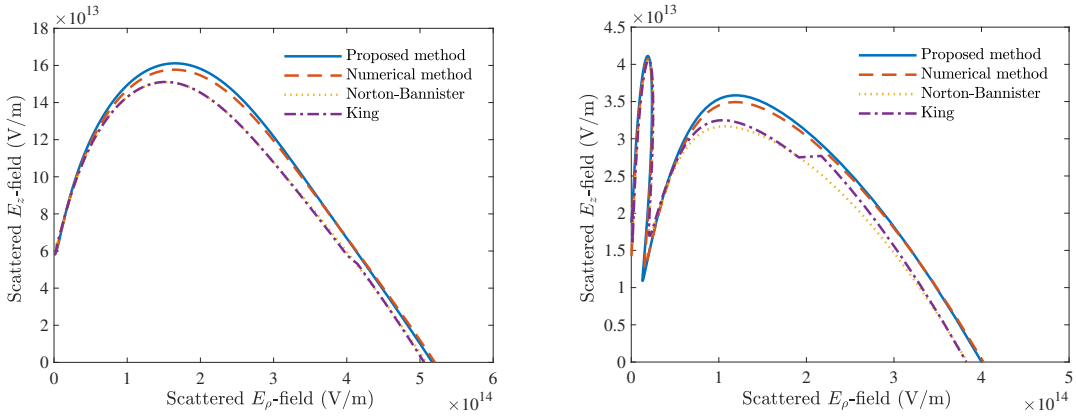

Fig. 4.5: The elevation pattern of the scattered electric field for a VED and its comparison with the proposed, Norton-Bannister and King solutions over a) silver and b) gold.

frequencies, the real part of the permittivity attains negative value and varies with frequency [101]. Figs. 4.5(a) and (b) depict the elevation patterns of the scattered electric field over the silver and gold, respectively, as plasmonic media. As is obvious from these two figures, the proposed solution agrees well with the numerical method, especially at high angles and near the interface where the surface wave contribution is high. Moreover, the NRMSE and NMAE values mentioned in Table 4.3 reveal that the proposed solution outperforms the conventional solution for plasmonic media. In order to evaluate the accuracy of the proposed solution for the magnetic field, the NRMSE and NMAE values of the H-field for silver and gold are provided in Table 4.3. As evident, all the NRMSE and NMAE values for the H-field are smaller than those associated with the conventional solutions.

Similar to non-plasmonic media, the NRMSE evaluation of the scattered electric

Table 4.3: Performance comparison between the proposed and conventional solutions for the plasmonic media

Medium		Proposed solution		King		Norton-Bannister	
		NRMSE	NMAE	NRMSE	NMAE	NRMSE	NMAE
Silver	E-field	0.0261	0.0397	0.0795	0.1188	0.0773	0.1188
	H-field	0.0123	0.0266	0.0237	0.0387	0.0241	0.0397
Gold	E-field	0.0267	0.0537	0.0736	0.2285	0.0896	0.2133
	H-field	0.0057	0.0141	0.0222	0.0495	0.0321	0.0727

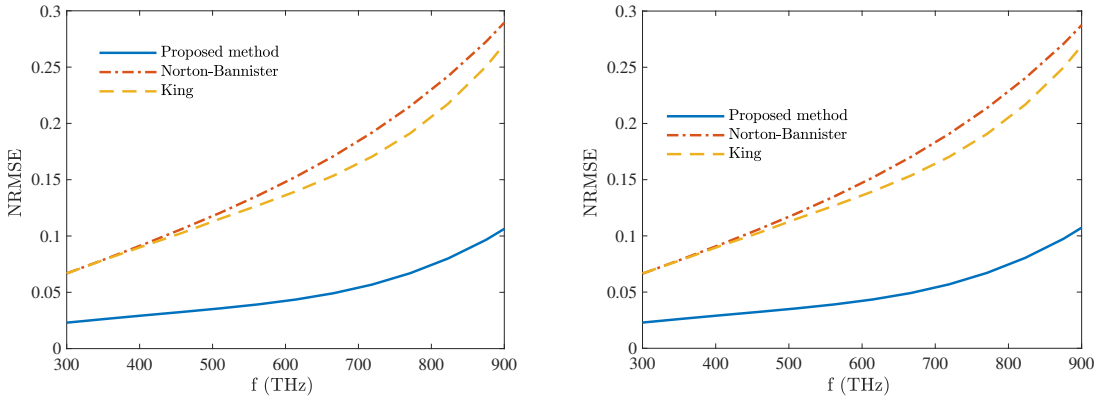

Fig. 4.6: The NRMSE of the scattered electric field for a VED at various frequencies and its comparison with the Norton-Bannister and King solutions over a) silver and b) gold.

fields for silver and gold are accomplished, while the frequency is changed between 300 to 900 THz. Fig. 4.6 demonstrates the NRMSE value of the scattered electric field at various frequencies for plasmonic media. As can be seen in this figure, the NRMSE value of the scattered electric field is less than the King and Norton-Bannister solutions in the optical frequency range. The NRMSE value of the silver in Fig. 4.6(a) is relatively similar to gold in Fig. 4.6(b) since the real and imaginary parts of the permittivity for both of them are quite similar in the optical frequency range. To

evaluate the accuracy of each scattered electric field component over plasmonic media, the NRMSE has been calculated for E_ρ and E_z components over silver and gold and compared with the conventional solutions, as shown in Fig. 4.7. As can be seen in this figure, the E_ρ and E_z components obtained by the proposed method have better accuracy in comparison with the conventional solutions over plasmonic media. The accuracy of E_z is better than E_ρ for plasmonic media contrary to non-plasmonic media due to the approximate solution of the integral in P represented in (4.3) using the modified saddle-point method. In addition, the accuracy of the proposed solution is evaluated in terms of NMAE for plasmonic media. Fig. 4.8 depicts the NMAE of the proposed solution for the scattered electric field intensity over plasmonic media. As is clear from the figure, the proposed solution outperforms the conventional solutions at various frequencies. It is worth mentioning that the complex relative permittivity of the plasmonic media varies with frequency. Here, the Drude model [102] is employed for the calculation of the complex relative permittivity at each frequency, which can be expressed as

$$\epsilon_r(\omega) = 1 + \frac{\mathrm{j}\sigma_0}{\omega\epsilon_0\left(1 - \mathrm{j}\omega\tau\right)} \tag{4.19}$$

wherein τ represents the average time between collisions experienced by an electron and can be written as

$$\tau = \frac{\sigma_0 m}{n_0 e^2} \tag{4.20}$$

in which m denotes the electron mass, n_0 is the electron density of the metal and e represents the elementary charge. Subsequently, (4.19) is utilized for each frequency

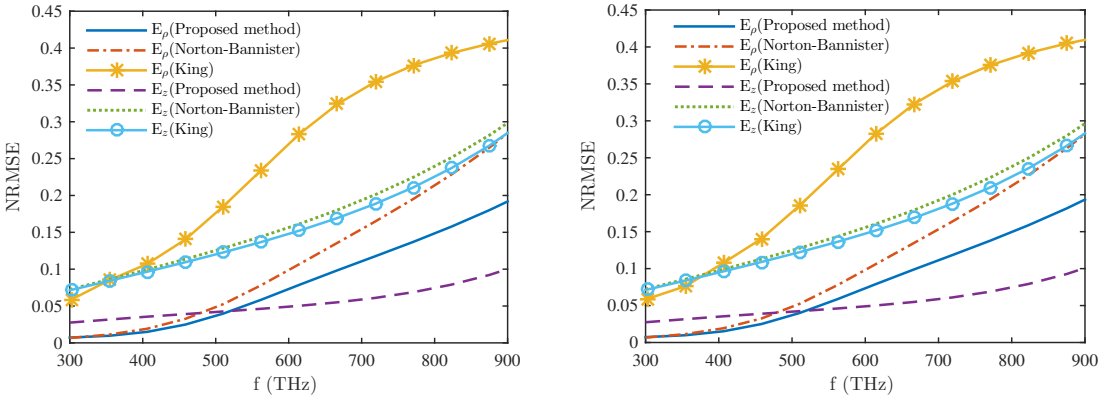

(a) (b)

Fig. 4.7: The NRMSE comparison of each scattered electric field component for a VED at various frequencies over a) silver and b) gold.

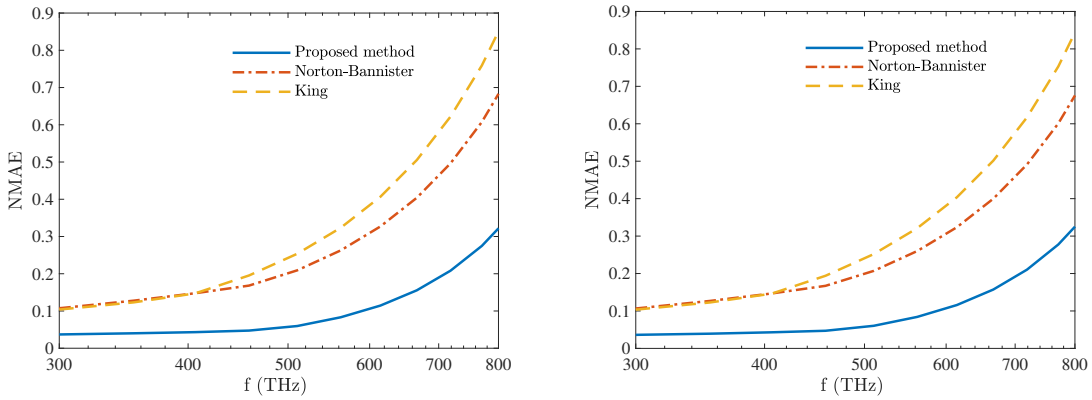

(a) (b)

Fig. 4.8: The NMAE of the scattered electric field for a VED at various frequencies and its comparison with the Norton-Bannister and King solutions over a) silver and b) gold.

in order to calculate the real and imaginary parts of the complex relative permittivity for the NRMSE and the NMAE calculations at various frequencies.

According to the error evaluations for plasmonic and non-plasmonic media, the error shows a general increase with frequency because by increasing the frequency, the

integrand of (4.4) becomes more oscillatory due to the presence of the wavenumber in the exponential function of the inetgrand.

4.3 Chapter Summary

In this chapter, a new asymptotic solution for the far-zone electromagnetic fields of a VED radiating over an imperfectly conducting half-space with a smooth interface has been developed. The solution has been evaluated for the both non-plasmonic and plasmonic media. Accuracy comparison indicates that the proposed solution outperforms the conventional solutions, i.e., King and Norton-Bannister solutions, in terms of NRMSE and NMAE at various frequencies and distances from the antenna in the far field region.

Chapter 5

Electromagnetic Wave Scattering by Random Surfaces With Different Contrast and Large Roughness Heights

In previous chapters, the Sommerfeld problem with a smooth interface was investigated. In this chapter[1], random roughness is added to the interface, and a new

[1]The content of this chapter is based on the following publications:
-M. E. Nazari and W. Huang, "EM wave scattering by random surfaces with different contrast and large roughness heights," IEEE J. Multiscale Multiphys. Comput. Tech., vol. 7, pp. 252-267, 2022.
-M. E. Nazari and W. Huang, "Scattering of EM waves from random surfaces with different contrast and surface roughness," ACES, pp. 1-3, 2021.
These papers provide the development of the scattered E-field and the radar cross-section from random rough surfaces with different contrast and large roughness heights.
Roles: Mr. Nazari conducted this research under the guidance of Dr. Huang and acted as the first author of the manuscript. All the contents of this paper were written by Mr. Nazari and further refined by Dr. Huang.

formulation for the scattered field over lossy time-invariant random rough surfaces with different contrast media and large roughness heights is proposed. The scattered field is represented in the form of an integral equation containing the normal component of the E-field. By using a Fourier series to represent the scattering surface, a general series solution is derived. With a monostatic configuration, the field equations are developed for a pulsed radar, and then the first-order scattered field and the radar cross-section at different incident angles are derived. This developed EM scattering theory can be used to identify electromagnetic properties (i.e., dielectric permittivity, electrical conductivity, and magnetic permeability) of the structure. For instance, in geophysical explorations, this theory may be used to determine the physical boundaries and characteristics of the soil layers [103].

This chapter is organized as follows. In Section 5.1, a general formulation for the scattered E-field over a lossy random rough surface with large roughness height is presented. The scattered E-field derivation incorporating the vertical dipole antenna is carried out in Section 5.2. The first-order backscattered E-field along with the radar cross-section is derived in Section 5.3. The proposed solution is evaluated by comparing it with the numerical (i.e., the method of moments (MoM) solution) and three alternative analytical solutions (i.e., the small perturbation (SPM), Kirchhoff approximation (KA) and small slope approximation (SSA) methods) at different incident angles and media characteristics in Section 5.4.

5.1 Statement of the Problem and Formulations

For a rough surface scattering problem, the entire space is divided into two regions and can be expressed using the generalized functions [69, 73, 104] as

$$h_{\mathcal{R}}(x,y,z) = 1 - h\left[z - \xi(x,y)\right], \;\; \mathcal{R}_{\rangle}\; i \in \{0,1\} \tag{5.1}$$

in which $h(\cdot)$ is the Heaviside function, $\mathcal{R}_{\rangle}$ represents each region and $\xi(x,y)$ denotes the two-dimensional rough surface shown in Fig. 5.1 in which ϵ, μ and σ respectively represent permittivity, permeability and conductivity of each region. Using (5.1), the E-field expression can be written as [69]

$$jk\eta_1|\vec{n}|^2\vec{E}_t^{+} = -\frac{\eta_1^2 - 1}{\eta_1^2}\nabla_{xy}\left(|\vec{n}|E_n^{+}\right) - jk\Delta|\vec{n}|^2\vec{E}_n^{-} - \vec{R}^{+} \tag{5.2}$$

wherein the intermediate vector $\vec{R}^{+}$ can be obtained from

$$2u\vec{E}_s = \mathcal{F}_{xy}\left\{\left(u|\vec{n}|^2\vec{E}^{+} - \vec{R}^{+}\right)e^{z-\xi(x,y)u}\right\}. \tag{5.3}$$

The remaining parameters in (5.2) and (5.3) can be acquired as

$$\begin{aligned} &u = \sqrt{K^2 - k^2},\; \Delta = \frac{1}{\eta_1},\; \eta_1 = \sqrt{\epsilon_{r_1} - \frac{j\sigma_1}{\omega\epsilon_0}},\; \vec{E}_n^{+} = \hat{n}\cdot\vec{E}^{+} \\ &\vec{E}_s = \left\{\frac{1}{j\omega\epsilon_0}\left[\nabla(\nabla\cdot\vec{J}_s) + k^2\vec{J}_s\right]\right\} \overset{xyz}{*} G_0,\; G_0 = \frac{e^{-jkr}}{4\pi r}. \end{aligned} \tag{5.4}$$

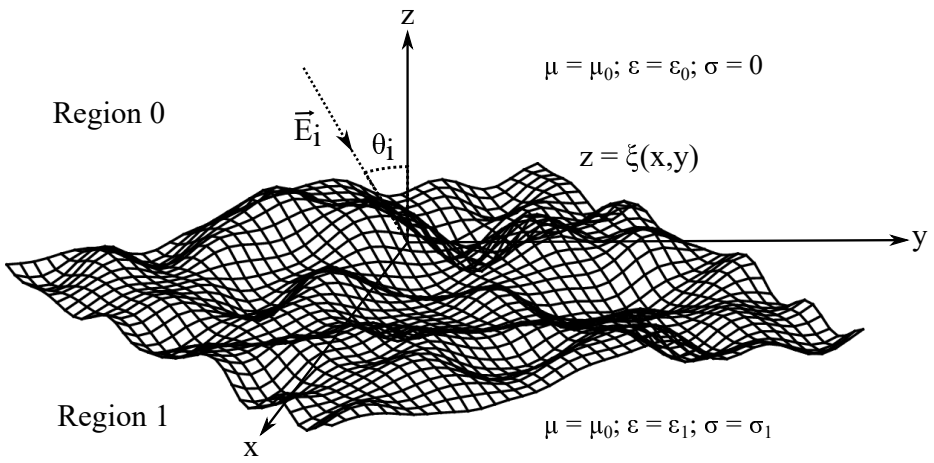

Fig. 5.1: Rough surface characterization and geometry of the problem

The plus and minus superscript respectively denote the value of the E-field above or below the scattering surface. In (5.2)-(5.4), η_1 denotes the refractive index in region 1, ϵ_{r_1} is the relative permittivity of Region 1, $\vec{E}_n$ and $\vec{E}_t$ respectively represent the normal and tangential component of the E-field, K denotes the surface wavenumber, k is the wavenumber of the source field, Δ is the surface impedance, $\mathcal{F}_{xy}$ represents the spatial Fourier transform in the $x-y$ plane, $\vec{n}$ is the normal vector to the scattering surface, $\vec{E}_s$ is the source electric field generated by the source current density $\vec{J}_s$ and G_0 is the Green's function solution of the Helmholtz equation in the free space. By inserting the intermediate vector $\vec{R}^+$ from (5.2) into (5.3) and representing the normal and tangential components of the E-field using operators [69, 73], the E-field operator

equation for lossy rough surface and arbitrary roughness heights can be derived as

$$\begin{aligned}
&NL^{-1}\left[\frac{2u\mathcal{F}_{xy}(\vec{E}_s)}{u+jk\Delta}-\frac{jk(\eta_1-\Delta)}{u+jk\Delta}LTL^{-1}\left(\frac{2u\mathcal{F}_{xy}(\vec{E}_s)}{u+jk\eta_1}\right)\right]\\
&=\vec{E}_n^{+}+NL^{-1}\left[\frac{1}{u+jk\Delta}L\left(\frac{\nabla_{xy}(|\vec{n}|E_n^{+})}{|\vec{n}|^2}\right)\right]\\
&-NL^{-1}\Bigg\{\frac{jk(\eta_1-\Delta)}{u+jk\Delta}LTL^{-1}\left[\frac{1}{u+jk\eta_1}L\left(\frac{\nabla_{xy}(|\vec{n}|E_n^{+})}{|\vec{n}|^2}\right)\right]\\
&+\frac{k^2(\eta_1-\Delta)^2}{u+jk\Delta}LTL^{-1}\left(\frac{L(E_n^{+})}{u+jk\eta_1}\right)\Bigg\}
\end{aligned}\tag{5.5}$$

where the tangential propagation operator T, the normal projection operator N and the invertible L operator are defined as

$$N(\vec{\mathbb{E}})=\hat{n}\hat{n}\cdot\vec{\mathbb{E}}=\vec{\mathbb{E}}_n,\;\; T(\vec{\mathbb{E}})=\vec{\mathbb{E}}-N(\vec{\mathbb{E}})=\vec{\mathbb{E}}_t,\;\; L(\vec{\mathbb{E}})=\mathcal{F}_{xy}\left\{|\vec{n}|^2\vec{\mathbb{E}}\,e^{(z-\xi(x,y))u}\right\}.\tag{5.6}$$

If the small-height approximation along with the highly conductive surface assumption is applied to (5.5), the equation would reduce to (41) presented in [69]. By applying the operators defined in (5.6), the left-hand side (LHS) of (5.5) becomes

$$\begin{aligned}
\text{LHS}=&\frac{A}{|\vec{n}|^2}N\Bigg\{\mathcal{F}_{xy}^{-1}\left(\frac{1}{u+jk\Delta}\right)\overset{xy}{*}\Bigg[\mathcal{F}_{xy}^{-1}\left\{2ue^{-zu}\mathcal{F}_{xy}(\vec{E}_s)\right\}\\
&-jk(\eta_1-\Delta)\mathcal{F}_{xy}^{-1}\left\{e^{-zu}LTL^{-1}\left(\frac{2u\,\mathcal{F}_{xy}(\vec{E}_s)}{u+jk\eta_1}\right)\right\}\Bigg]\Bigg\}
\end{aligned}\tag{5.7}$$

wherein $A=\mathcal{F}_{xy}^{-1}\left\{\mathcal{F}_{xy}\left[e^{\xi(x,y)u}\right]\right\}$ is associated with the RMS height of the rough surface and derived from the L operator. It is worth mentioning that the two Fourier transforms in A cannot cancel each other since the argument $e^{\xi(x,y)u}$ is in both $x-y$

space and spatial frequency (k_x-k_y) domain. On the other hand, by assuming a vertical dipole antenna located above the scattering surface, $\vec{E}_s$ can be expressed as

$$\vec{E}_s = \frac{I\Delta l\, k^2}{j\omega\epsilon_0}\frac{e^{-jkr}}{4\pi r}\,\hat{z} \triangleq C_0 G_0\,\hat{z} \tag{5.8}$$

wherein Δl denotes the dipole length and I is the current of the antenna. To simplify the field source expression in (5.7), the L^{-1} operator is applied to $2u\mathcal{F}_{xy}(\vec{E}_s)$. Therefore, we have

$$L^{-1}\left\{2u\mathcal{F}_{xy}(\vec{E}_s)\right\} = \frac{A}{|\vec{n}|^2}C_0\delta(x)\delta(y)\,\hat{z}. \tag{5.9}$$

By distributing the N operator over a sum in (5.7), using an asymptotic expansion in the integral of $\mathcal{F}_{xy}^{-1}\left(\frac{1}{u+jk\Delta}\right)$ and employing (5.9), the LHS can be further simplified as

$$\text{LHS}{=}C_0 A\vec{n}\left\{\frac{F(\rho)e^{-jk\rho}}{2\pi\rho} + \nabla_\xi\cdot\left[jk(\eta_1-\Delta)\frac{F(\rho)e^{-jk\rho}}{2\pi\rho} \overset{xy}{*} \Lambda\nabla_\xi\right]\right\} \tag{5.10}$$

where $F(\rho)$ is the Sommerfeld attenuation function [105] and $\Lambda = \mathcal{F}_{xy}^{-1}\left(\frac{1}{u+jk\eta_1}\right)$. Using $F(\rho)$ and applying the L^{-1} operator, the right-hand side (RHS) of (5.5) is simplified as

$$\text{RHS} = \vec{E}_n^{+} + \frac{A}{|\vec{n}|^2}N\left[\frac{F(\rho)e^{-jk\rho}}{2\pi\rho} \overset{xy}{*} \mathcal{F}_{xy}^{-1}\left(T_1+T_2+T_3\right)\right] \tag{5.11}$$

wherein T_1, T_2 and T_3 are derived as

$$T_1 = \mathcal{F}_{xy}\left\{e^{-\xi(x,y)u}\nabla_{xy}\left(|\vec{n}|E_n^+\right)\right\} \tag{5.12}$$

$$T_2 = -jk(\eta_1-\Delta)\mathcal{F}_{xy}\left\{Ae^{-\xi(x,y)u}\,T\left[\Lambda \overset{xy}{*} \frac{\nabla_{xy}\left(|\vec{n}|E_n^+\right)}{A}\right]\right\} \tag{5.13}$$

$$T_3 = -k^2(\eta_1-\Delta)^2\mathcal{F}_{xy}\left\{Ae^{-\xi(x,y)u}\,T\left[\Lambda \overset{xy}{*} \frac{\vec{E}_n^+}{A}\right]\right\}. \tag{5.14}$$

By applying the spatial Fourier transform along with the small-slope approximation (i.e., $|\vec{n}|^2 = 1 + |\nabla\xi(x,y)|^2 \approx 1$), the RHS can be derived as

$$\begin{aligned}\text{RHS} = \vec{E}_n^+ + A\vec{n}\vec{n}\cdot\Bigg\{\frac{F(\rho)e^{-jk\rho}}{2\pi\rho} \overset{xy}{*} \Bigg[&-jk(\eta_1-\Delta)T\left(\Lambda \overset{xy}{*} \frac{\nabla_{xy}(E_n^+)}{A}\right)\\ &-k^2(\eta_1-\Delta)^2T\left(\Lambda \overset{xy}{*} \frac{\vec{E}_n^+}{A}\right)+\frac{\nabla_{xy}(E_n^+)}{A}\Bigg]\Bigg\}.\end{aligned} \tag{5.15}$$

By considering (5.15) and (5.10) and applying the small-slope approximation to (5.10), particularly the second term, the scattered E-field expression (5.5) can be written as

$$\begin{aligned}\vec{E}_n^+ - A\vec{n}\vec{n}\cdot\Bigg\{\frac{F(\rho)e^{-jk\rho}}{2\pi\rho} \overset{xy}{*} \Bigg[&jk(\eta_1-\Delta)T\left[\frac{\nabla_{xy}(E_n^+)}{A} \overset{xy}{*} \Lambda\right]\\ &+k^2(\eta_1-\Delta)^2T\left[\Lambda \overset{xy}{*} \frac{\vec{E}_n^+}{A}\right]-\frac{\nabla_{xy}(E_n^+)}{A}\Bigg]\Bigg\} = C_0A\vec{n}\frac{F(\rho)e^{-jk\rho}}{2\pi\rho}.\end{aligned} \tag{5.16}$$

In order to obtain an expression for the scattered E-field in terms of the field source, the first-order Neumann series solution [69] is applied to (5.16). It should be noted that the order of the Neumann series corresponds to the coupling of the electro-

magnetic waves with the rough surface, and the zero order term corresponds to the scattering by a smooth plane surface with the surface impedance Δ. Therefore, the first-order scattered E-field can be derived as [106, 107]

$$
\begin{aligned}
(E_n^+)_1 = -A\vec{n}\cdot\Bigg\{ & \frac{F(\rho)e^{-jk\rho}}{2\pi\rho} \overset{xy}{*} \Bigg[\frac{1}{A}\nabla_{xy}\Big(C_0 A\frac{F(\rho)e^{-jk\rho}}{2\pi\rho}\Big) \\
& - jk(\eta_1-\Delta)T\Bigg[\Lambda \overset{xy}{*} \frac{1}{A}\nabla_{xy}\Big(\frac{C_0 AF(\rho)}{2\pi\rho}e^{-jk\rho}\Big)\Bigg] \\
& - k^2(\eta_1-\Delta)^2 T\Bigg[\Lambda \overset{xy}{*} C_0\frac{F(\rho)}{2\pi\rho}e^{-jk\rho}\vec{n}\Bigg]\Bigg]\Bigg\}.
\end{aligned}
\tag{5.17}
$$

The E-field expression in (5.17) not only contains the arbitrary height factor A but also can deal with moderate contrast media. In order to find an approximate closed-form solution for the first-order scattered E-field (5.17), the RHS of (5.17) is split up into three terms (i.e., Term 1, Term 2 and Term 3) while the first-order scattered E-field is the summation of these three terms. By expanding the normal vector $\vec{n}$ and considering the dot product in (5.17), these three terms can be obtained.

$$
\text{Term 1} = AC_0\nabla_\xi\cdot\Bigg[\frac{F(\rho)e^{-jk\rho}}{2\pi\rho} \overset{xy}{*} \frac{1}{A}\nabla_{xy}\Big(C_0 A\frac{F(\rho)e^{-jk\rho}}{2\pi\rho}\Big)\Bigg] \tag{5.18}
$$

$$
\text{Term 2} = jAk(\eta_1-\Delta)C_0\hat{n}\cdot\Bigg[\frac{F(\rho)e^{-jk\rho}}{2\pi\rho} \overset{xy}{*} T\Bigg[\Lambda \overset{xy}{*} \frac{1}{A}\nabla_{xy}\Big(\frac{AF(\rho)e^{-jk\rho}}{2\pi\rho}\Big)\Bigg]\Bigg] \tag{5.19}
$$

$$
\text{Term 3} = \frac{AC_0k^2}{(\eta_1-\Delta)^{-2}}\hat{n}\cdot\Bigg[\frac{F(\rho)e^{-jk\rho}}{2\pi\rho} \overset{xy}{*} T\Bigg[\Lambda \overset{xy}{*} \frac{F(\rho)e^{-jk\rho}\vec{n}}{2\pi\rho}\Bigg]\Bigg] \tag{5.20}
$$

5.2 Scattered Field Calculation Incorporating Vertical Dipole Antenna

In this section, the proposed three terms associated with the first-order scattered E-field are calculated while the arbitrary height factor and moderate contrast media are considered simultaneously in the derivation of the scattered E-field. First, the A parameter associated with arbitrary height should be calculated. By using the power series expansion of $e^{\xi(x,y)u}$ and applying the spatial Fourier transform we have

$$\mathcal{F}_{xy}\left\{e^{\xi(x,y)u}\right\} \sim 4\pi^2\delta(x)\delta(y) + u\mathcal{F}_{xy}\left\{\xi(x,y)\right\}. \tag{5.21}$$

In order to further simplify (5.21), the rough surface should be characterized. The two-dimensional Fourier series is utilized to represent the rough surface as follows

$$\xi(x,y) = \sum_{m,n} P_{mn} e^{j\kappa(mx+ny)} \tag{5.22}$$

wherein the P_{mn} denote Fourier coefficients and κ represents the fundamental wavenumber of the surface in x and y directions. By using the (m,n)th surface wave vector $\vec{\boldsymbol{k}}_{mn} = \kappa m\hat{x} + \kappa n\hat{y}$ and displacement vector $\vec{\boldsymbol{\rho}} = x\hat{x} + y\hat{y}$ on the surface, the rough

surface can be rewritten as

$$\xi(x,y) = \sum_{m,n} P_{mn} e^{j\vec{\boldsymbol{\rho}}\cdot\vec{\boldsymbol{k}}_{mn}} = \sum_{m,n} P_{mn} e^{j\rho k_{mn}\cos(\theta_{mn}-\theta)} \tag{5.23}$$

where θ and θ_{mn} represent the directions of $\vec{\boldsymbol{\rho}}$ and $\vec{\boldsymbol{k}}_{mn}$, respectively. By inserting (5.22) into (5.21) and using the Dirac delta identities, (5.21) can be further simplified as

$$\mathcal{F}_{xy}\left[e^{\xi(x,y)u}\right] \sim 4\pi^2\left[\sum_{m,n} \frac{P_{mn}\delta(k_x-\kappa m)\delta(k_y-\kappa n)}{(k_{mn}^2-k^2)^{-0.5}} + \delta(x)\delta(y)\right] \tag{5.24}$$

where $\delta(.)$ represents the Dirac delta function. Now, by applying the inverse spatial Fourier transform to (5.24), the A parameter is approximated as

$$A \simeq 1 + \sum_{m,n} P_{mn}\sqrt{k_{mn}^2 - k^2}\, e^{j\rho k_{mn}\cos(\theta_{mn}-\theta)}. \tag{5.25}$$

5.2.1 Term 1

By considering the gradient in $x-y$ space in the cylindrical coordinate, i.e., $\nabla_{xy} = \partial/\partial\rho\,\hat{\rho} + (1/\rho)(\partial/\partial\theta)\,\hat{\theta}$, and considering the far-field region ($k\rho \gg 1$), we have

$$\nabla_{xy}\left(C_0\frac{F(\rho)e^{-jk\rho}}{2\pi\rho}\right) \sim -jkC_0F(\rho)\frac{e^{-jk\rho}}{2\pi\rho}. \tag{5.26}$$

By considering (5.26) and applying the gradient in the cylindrical coordinate, Term 1 can be further simplified in an asymptotic sense as follows

$$\begin{aligned}\text{Term 1}=&-C_0A\left[\frac{F(\rho)e^{-jk\rho}}{2\pi\rho}{}_{xy}{*}\frac{F(\rho)e^{-jk\rho}}{2\pi\rho}(g_1(x,y)+jk)\nabla_\xi\cdot\hat{\rho}\right.\\&\left.+\frac{F(\rho)e^{-jk\rho}}{2\pi\rho}{}_{xy}{*}\frac{F(\rho)e^{-jk\rho}}{2\pi\rho}g_2(x,y)\nabla_\xi\cdot\hat{\theta}\right]\equiv -C_0A(T_4\,\nabla_\xi\cdot\hat{\rho}+T_5\,\nabla_\xi\cdot\hat{\theta})\end{aligned}\tag{5.27}$$

wherein $D_t=1/A$ and g_1 as well as g_2 are

$$\begin{aligned}g_1(x,y)=&-j\sum_{m,n}P_{mn}k_{mn}\cos(\theta_{mn}-\theta)\sqrt{k_{mn}^2-k^2}e^{j\rho k_{mn}\cos(\theta_{mn}-\theta)}\\&-j\sum_{m,n}\sum_{p,q}P_{mn}P_{pq}k_{pq}\cos(\theta_{pq}-\theta)\sqrt{(k_{mn}^2-k^2)(k_{pq}^2-k^2)}\\&\times e^{j\rho[k_{mn}\cos(\theta_{mn}-\theta)+k_{pq}\cos(\theta_{pq}-\theta)]}\end{aligned}\tag{5.28}$$

$$\begin{aligned}g_2(x,y)=&-j\sum_{m,n}P_{mn}k_{mn}\sin(\theta_{mn}-\theta)\sqrt{k_{mn}^2-k^2}e^{j\rho k_{mn}\cos(\theta_{mn}-\theta)}\\&-j\sum_{m,n}\sum_{p,q}P_{mn}P_{pq}k_{pq}\sin(\theta_{pq}-\theta)\sqrt{(k_{mn}^2-k^2)(k_{pq}^2-k^2)}\\&\times e^{j\rho[k_{mn}\cos(\theta_{mn}-\theta)+k_{pq}\cos(\theta_{pq}-\theta)]}.\end{aligned}\tag{5.29}$$

Now, the convolution in (5.27) in $x-y$ space should be calculated. By changing of from Cartesian coordinates to polar form and considering the backscattered E-field we have

$$T_4=\frac{1}{4\pi^2}\int_{\rho_1}\int_{\theta_1}\frac{F^2(\rho_1)e^{-2jk\rho_1}}{\rho_1}g(\theta_1)g_1(\rho_1,\theta_1)\,d\theta_1d\rho_1+\frac{jkG}{4\pi^2}\int_{\rho_1}\frac{F^2(\rho_1)e^{-2jk\rho_1}}{\rho_1}d\rho_1\tag{5.30}$$

wherein $g(\theta)$ denotes the normalized radiation pattern of the receiver antenna and G represents the integral of the radiation pattern over azimuth. By inserting (5.28) into T_4 and using the stationary phase integration technique [108], (5.30) becomes

$$T_4 = -\frac{j\sqrt{2\pi}}{4\pi^2}\int_{\rho_1}\frac{F^2(\rho_1)e^{-2jk\rho_1}}{\rho_1^{1.5}}(T_6+T_7+T_8)\,d\rho_1 + \frac{jkG}{4\pi^2}\int_{\rho_1}\frac{F^2(\rho_1)e^{-2jk\rho_1}}{\rho_1}\,d\rho_1 \tag{5.31}$$

wherein T_6, T_7 and T_8 are calculated as follows

$$\begin{aligned} T_6 = &\sum_{m,n} P_{mn} g(\theta_{mn})\sqrt{k_{mn}(k_{mn}^2-k^2)}e^{j(\rho_1 k_{mn}-\pi/4)} \\ &-\sum_{m,n} P_{mn} g(\theta_{mn}+\pi)\sqrt{k_{mn}(k_{mn}^2-k^2)}e^{-j(\rho_1 k_{mn}-\pi/4)} \end{aligned} \tag{5.32}$$

$$\begin{aligned} T_7 = &\sum_{m,n}\sum_{p,q} P_{mn}P_{pq}k_{pq}\sqrt{(k_{mn}^2-k^2)(k_{pq}^2-k^2)} \\ &e^{j\rho_1|\vec{\boldsymbol{k}}_{mn}+\vec{\boldsymbol{k}}_{pq}|}\,\cos(\theta_{pq}-\theta_s)\,g(\theta_s)\frac{e^{-j\pi/4}}{\sqrt{|\vec{\boldsymbol{k}}_{mn}+\vec{\boldsymbol{k}}_{pq}|}} \end{aligned} \tag{5.33}$$

$$\begin{aligned} T_8 = &-\sum_{m,n}\sum_{p,q} P_{mn}P_{pq}k_{pq}\sqrt{(k_{mn}^2-k^2)(k_{pq}^2-k^2)} \\ &e^{-j\rho_1|\vec{\boldsymbol{k}}_{mn}+\vec{\boldsymbol{k}}_{pq}|}\,\cos(\theta_{pq}-\theta_s)\,g(\theta_s+\pi)\frac{e^{j\pi/4}}{\sqrt{|\vec{\boldsymbol{k}}_{mn}+\vec{\boldsymbol{k}}_{pq}|}} \end{aligned} \tag{5.34}$$

where

$$\theta_s = \tan^{-1}\left[\frac{k_{mn}\sin\theta_{mn}+k_{pq}\sin\theta_{pq}}{k_{mn}\cos\theta_{mn}+k_{pq}\cos\theta_{pq}}\right]. \tag{5.35}$$

The next term that requires calculation for simplifying Term 1 in (5.27) is T_5. By substituting $g_2(x,y)$ from (5.29) into the second expression of (5.27) and using the

stationary phase integration method, T_5 becomes

$$T_5 = -\frac{j\sqrt{2\pi}}{4\pi^2}\int_{\rho_1}\frac{F^2(\rho_1)e^{-2jk\rho_1}}{\rho_1^{1.5}}(T_9+T_{10})\,d\rho_1 \tag{5.36}$$

wherein T_9 and T_{10} respectively are similar to T_7 and T_8 except for the term of $\cos(\theta_{pq}-\theta_s)$. In other words, by replacing $\cos(\theta_{pq}-\theta_s)$ in T_7 and T_8 with $\sin(\theta_{pq}-\theta_s)$, T_9 and T_{10} are acquired.

5.2.2 Term 2

Following Term 1, Term 2 requires calculation for determining the scattered E-field in (5.17). By applying the gradient in $x-y$ space in the cylindrical coordinate to the Sommerfeld attenuation term in (5.19) and employing (5.28) and (5.29) we have

$$\begin{aligned}\text{Term 2} = -\frac{jk}{D_t}(\eta_1-\Delta)C_0\vec{n}\cdot\Bigg[\frac{F(\rho)e^{-jk\rho}}{2\pi\rho}\overset{xy}{*}T\Bigg[\frac{F(\rho)e^{-jk\rho}}{2\pi\rho}\\ \Big[\big(jk+g_1(x,y)\big)\hat{\rho}+g_2(x,y)\hat{\theta}\Big]\overset{xy}{*}\Lambda\Bigg].\end{aligned} \tag{5.37}$$

To simplify (5.37), a solution for Λ should be derived. This solution is addressed below in section 5.2.2.1. It is worth mentioning that by considering small height condition along with highly conductive surface (i.e., high contrast media), the arbitrary height factor A in (5.25) becomes one. Also, $g_1(x,y)$ and $g_2(x,y)$ in (5.28) and (5.29) become zero since the derivative of the arbitrary factor A in $g_1(x,y)$ and $g_2(x,y)$ are zero.

Consequently, Term 1 can be reduced to

$$\text{Term 1} = -jkC_0 \left[\frac{F(\rho)e^{-jk\rho}}{2\pi\rho} \overset{xy}{*} \frac{F(\rho)e^{-jk\rho}}{2\pi\rho} \nabla_\xi \cdot \hat{\rho} \right]. \tag{5.38}$$

Furthermore, the surface impedance can be ignored when compared with the complex refractive index due to highly conductive surface assumption. Thus, Term 2 for small height condition and highly conductive surface can be reduced to

$$\text{Term 2} = -jkC_0 \vec{n} \cdot \left[\frac{F(\rho)e^{-jk\rho}}{2\pi\rho} \overset{xy}{*} T \left[\frac{F(\rho)e^{-jk\rho}}{2\pi\rho} \hat{\rho} \right] \right] \tag{5.39}$$

Also, Term 3 becomes zero as addressed in section 5.2.3. By applying the T operator of (5.6) in (5.39) and adding (5.38) and (5.39), the first order backscattered E-field can be expressed as

$$\begin{aligned}(E_n^+)_1 = &-jkC_0 \left[\frac{F(\rho)e^{-jk\rho}}{2\pi\rho} \overset{xy}{*} \frac{F(\rho)e^{-jk\rho}}{2\pi\rho} \nabla_\xi \cdot \hat{\rho} \right] - jkC_0 \vec{n} \cdot \left[\frac{F(\rho)e^{-jk\rho}}{2\pi\rho} \overset{xy}{*} \frac{F(\rho)e^{-jk\rho}}{2\pi\rho} \hat{\rho} \right. \\ &\left. + \frac{F(\rho)e^{-jk\rho}}{2\pi\rho} \overset{xy}{*} \frac{F(\rho)e^{-jk\rho}}{2\pi\rho} \nabla_\xi \cdot \hat{\rho}\ \hat{n} \right]\end{aligned} \tag{5.40}$$

in which the first two terms cancel each other. Consequently, the first order backscattered E-field for small height condition and highly conductive surface can be reduced to

$$(E_n^+)_1 = -jkC_0 \left[\frac{F(\rho)e^{-jk\rho}}{2\pi\rho} \overset{xy}{*} \frac{F(\rho)e^{-jk\rho}}{2\pi\rho} \nabla_\xi \cdot \hat{\rho} \right] \tag{5.41}$$

which is same as the backscattered E-field equation derived in [69] for small height and high contrast media conditions.

5.2.2.1 Calculation of Λ

By multiplying the numerator and denominator of the argument of Λ by the conjugate of the denominator, Λ can be expressed as

$$\Lambda = \mathcal{F}_{xy}^{-1}\left[\frac{u}{K^2+(\eta_1^2-1)k^2} - \frac{jk\eta_1}{K^2+(\eta_1^2-1)k^2}\right] \tag{5.42}$$

wherein $K^2 = k_x^2 + k_y^2$. By considering high and moderate contrast media, Λ can be approximated as

$$\Lambda \simeq \mathcal{F}_{xy}^{-1}\left(\frac{u}{u_p^2} - \frac{u_1}{u_p^2}\right) \tag{5.43}$$

in which $u_1^2 = K^2 - \eta_1^2 k^2$, $u_p^2 = K^2 + n_p^2 k^2$ and $n_p^2 = \eta_1^2 - 1$. First, we represent an approximate closed-form solution for the second term of Λ since by changing η_1 to one, the first term corresponds to the free space solution. By multiplying the numerator and the denominator of this term with u_1 and then decomposing into partial fractions, this term becomes

$$\begin{aligned}\mathcal{F}_{xy}^{-1}\left(\frac{u_1}{u_p^2}\right) &= \mathcal{F}_{xy}^{-1}\left(\frac{1}{u_1}\right) - k^2(\eta_1^2+n_p^2)\mathcal{F}_{xy}^{-1}\left(\frac{1}{u_1 u_p^2}\right) \\ &= \frac{e^{-jk\eta_1\rho}}{2\pi\rho} - k^2(\eta_1^2+n_p^2)\left[\frac{e^{-jk\eta_1\rho}}{2\pi\rho} \overset{xy}{*} \frac{e^{-kn_p\rho}}{2\pi\rho} \overset{xy}{*} \frac{e^{-kn_p\rho}}{2\pi\rho}\right].\end{aligned} \tag{5.44}$$

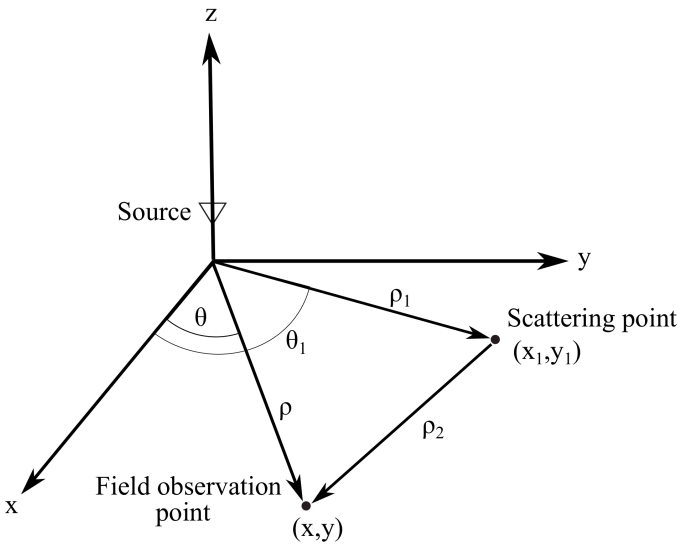

Fig. 5.2: Geometry of the first-order scatter

By calculating the double convolution using a series of variable changes in the Cartesian coordinate for the inner double integral and approximating the integrand in descending powers of ρ, (5.44) is approximated as

$$\mathcal{F}_{xy}^{-1}\left(\frac{u_1}{u_p^2}\right) \simeq \frac{j}{2}\sqrt{\frac{k(\eta_1^2+n_p^2)}{2n_p\rho\pi}}\frac{e^{-k\rho(n_p+j\eta_1)}}{2\pi\rho}\text{erf}\left(\sqrt{\rho k(j\eta_1-n_p)}\right) \tag{5.45}$$

By changing η_1 to one in (5.45), the first term of Λ can also be acquired. Consequently, Λ can be approximated as $\frac{F_n(\rho)e^{-jk\rho}}{2\pi\rho}$ where

$$\begin{aligned} F_n(\rho) = 1 - e^{-jk\rho(\eta_1-1)} + je^{k\rho(j-n_p)}\sqrt{\frac{k\rho\pi}{2n_p}}\Bigg[\sqrt{1+n_p^2}\,\text{erf}\left(\sqrt{\rho k(j-n_p)}\right) \\ - \sqrt{\eta_1^2+n_p^2}\;\text{erf}\left(\sqrt{\rho k(j\eta_1-n_p)}\right)\Bigg]. \end{aligned} \tag{5.46}$$

Now, by inserting (5.46) into (5.37), the internal spatial convolution in $x-y$ space can be calculated. As is evident in (5.37), the argument of operator T has two dimensions. By decomposing this expression into two terms (i.e., I_1 and I_2 respectively in $\hat{\rho}$ and $\hat{\theta}$ directions), we have

$$I_1 = \frac{F_n(\rho)e^{-jk\rho}}{2\pi\rho} \overset{xy}{*} \frac{F(\rho)e^{-jk\rho}}{2\pi\rho}\left(jk + g_1(x,y)\right) \tag{5.47}$$

$$I_2 = \frac{F_n(\rho)e^{-jk\rho}}{2\pi\rho} \overset{xy}{*} \frac{F(\rho)e^{-jk\rho}}{2\pi\rho} g_2(x,y) \tag{5.48}$$

By considering the spatial convolution in the $x-y$ plane, I_1, in its integral form, can be expressed as

$$\begin{aligned} I_1 &= \frac{jk}{4\pi^2}\int_{x_1}\int_{y_1} \frac{F(\rho_1)F_n(\rho_2)}{\rho_1\rho_2} e^{-jk(\rho_1+\rho_2)}\, dx_1 dy_1 \\ &+ \frac{1}{4\pi^2}\int_{x_1}\int_{y_1} \frac{F(\rho_1)F_n(\rho_2)}{\rho_1\rho_2} g_1(x_1,y_1) e^{-jk(\rho_1+\rho_2)} dx_1 dy_1 \equiv I_3 + I_4 \end{aligned} \tag{5.49}$$

wherein ρ_2 is the distance from the scatter point to the reception point as shown in Fig. 5.2. It should be noted that ρ_2 depends on θ_1 and can be small. Thus, the assumption of *slowly varying* in the stationary phase approximation method might be violated. By rotating the axes by θ, a shift of the origin to a position halfway along ρ and converting the Cartesian coordinate to the elliptic coordinate system, the integrals can be calculated using the stationary phase approximation method since the product $\rho_1\rho_2$ in the denominator is eliminated. According to Fig. 5.3, x_1 and y_1 in the new coordinate system become

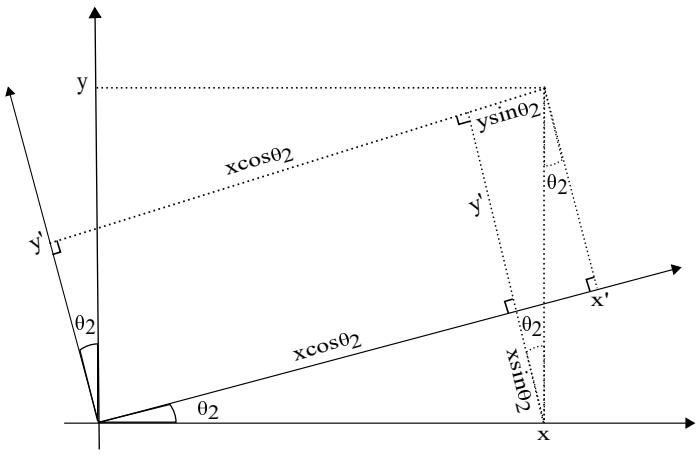

Fig. 5.3: Rotation of coordinate axes by θ_2

$$x_1 = (x_1'' + \frac{\rho}{2})\cos\theta - y_1''\sin\theta,\ y_1 = (x_1'' + \frac{\rho}{2})\sin\theta - y_1''\cos\theta. \tag{5.50}$$

By converting the Cartesian coordinate to the elliptic coordinate (μ, δ), x_1'' and y_1'' are expressed as

$$x_1'' = \frac{\rho}{2}\cosh\mu\,\cos\delta,\ y_1'' = \frac{\rho}{2}\sinh\mu\,\sin\delta \tag{5.51}$$

By substituting (5.51) into (5.50), ρ_1 and ρ_2 become

$$\rho_1 = \frac{\rho}{2}\left(\cosh\mu + \cos\delta\right),\ \rho_2 = \frac{\rho}{2}\left(\cosh\mu - \cos\delta\right). \tag{5.52}$$

Thus, I_3 in the elliptic coordinate system can be acquired by inserting (5.52) into (5.51). Thus, we have

$$I_3 = \frac{jk}{\pi^2}\int_\mu\int_\delta \frac{F(\rho_1)F_n(\rho_2)e^{-jk\rho\cosh\mu}J(\mu,\delta)}{\rho^2(\cosh\mu+\cos\delta)(\cosh\mu-\cos\delta)}\,d\delta\,d\mu \tag{5.53}$$

where $J(\mu, \delta)$ denotes the Jacobian determinant [109] and can be calculated as follows

$$J(\mu,\delta) = \begin{vmatrix} \dfrac{\partial x_1}{\partial \mu} & \dfrac{\partial x_1}{\partial \delta} \\ \dfrac{\partial y_1}{\partial \mu} & \dfrac{\partial y_1}{\partial \delta} \end{vmatrix} = \frac{\rho^2}{4}\left(\sin^2\delta + \sinh^2\mu\right). \tag{5.54}$$

By inserting the Jacobian determinant (5.54) into (5.53), I_3 can be expressed as

$$I_3 = \frac{jk}{4\pi^2}\int_{\mu}\int_{\delta} F(\rho_1)F_n(\rho_2)e^{-jk\rho\cosh\mu}\,d\delta\,d\mu. \tag{5.55}$$

Now, the stationary phase integration method is applied to (5.55) and I_3 becomes

$$I_3 = \frac{jk\sqrt{2\pi}e^{-j\pi/4}}{8\pi^2\sqrt{k\rho}}\int_0^{\pi} F\big(\frac{\rho}{2}(1+\cos\delta)\big)F_n\big(\frac{\rho}{2}(1-\cos\delta)\big)d\delta. \tag{5.56}$$

In order to further simplify I_3, the Sommerfeld attenuation function F and F_n in (5.46) should be substituted into (5.56). By using the stationary phase integration method along with small and large argument approximations of the error function, this integral can be calculated. The details concerning this integral calculation are shown in Appendix B.

The next integral that requires calculation is I_4 in (5.49). By inserting $g_1(x, y)$ as presented in (5.28) and converting the Cartesian coordinates to elliptic coordinates,

I_4 becomes

$$I_4 = \frac{-j}{4\pi^2}\sum_{m,n} P_{mn}k_{mn}\sqrt{k_{mn}^2-k^2}\int_\delta\int_\mu \cos(\theta_{mn}-\theta_1)e^{j\rho_1 k_{mn}\cos(\theta_{mn}-\theta_1)}e^{-jk\rho\cosh\mu}$$
$$F(\rho_1)F_n(\rho_2)\,d\mu\,d\delta + \frac{-j}{4\pi^2}\sum_{p,q}\sum_{m,n} P_{mn}P_{pq}k_{pq}\sqrt{(k_{mn}^2-k^2)(k_{pq}^2-k^2)}\int_\delta\int_\mu \cos(\theta_{pq}-\theta_1)$$
$$e^{j\rho_1[k_{mn}\cos(\theta_{mn}-\theta_1)+k_{pq}\cos(\theta_{pq}-\theta_1)]}e^{-jk\rho\cosh\mu}F(\rho_1)F_n(\rho_2)\,d\mu\,d\delta \equiv I_5 + I_6 \tag{5.57}$$

in which $\theta_1 = \tan^{-1}(y_1/x_1)$. By considering the first integral term in (5.57) (i.e., I_5) and using (5.52), I_5 can be simplified as

$$I_5 = \sum_{m,n} S_0 \int_\delta\int_\mu F(\rho_1)F_n(\rho_2)\cos(\theta_{mn}-\theta_1)e^{j\frac{\rho}{2}\psi}d\delta\,d\mu \tag{5.58}$$

wherein S_0 and ψ can be written as

$$\begin{aligned} S_0 &= \frac{-j}{4\pi^2}P_{mn}k_{mn}\sqrt{k_{mn}^2-k^2} \\ \psi &= -2k\cosh\mu + k_{mn}\cos(\theta_{mn}-\theta_1)(\cosh\mu+\cos\delta). \end{aligned} \tag{5.59}$$

In order to represent a closed-form solution for I_5, the two-dimensional stationary phase integration method should be employed. Thus, the determinant of the Hessian matrix [109] should be calculated, which can be represented as follows

$$\det\big(H(\mu,\delta)\big) = \begin{vmatrix} \dfrac{\partial^2\psi}{\partial\mu^2} & \dfrac{\partial^2\psi}{\partial\delta\partial\mu} \\ \dfrac{\partial^2\psi}{\partial\delta\partial\mu} & \dfrac{\partial^2\psi}{\partial\delta^2} \end{vmatrix} = 2kk_{mn}\cos(\theta_{mn}-\theta) - k_{mn}^2. \tag{5.60}$$

By employing (5.60) along with the two-dimensional stationary phase integration method, I_5 can be approximated as

$$I_5 \simeq \frac{2\pi}{\rho}\sum_{m,n} S_0 F(\rho)\frac{\cos(\theta_{mn}-\theta)e^{j\rho(k_{mn}\cos(\theta_{mn}-\theta)-k)}}{\sqrt{k_{mn}^2-2kk_{mn}\cos(\theta_{mn}-\theta)}}. \tag{5.61}$$

Similar to I_5, two-dimensional stationary phase integration method is used for the calculation of I_6 in (5.57), resulting in

$$I_6 = \frac{2\pi F(\rho)}{\rho}\sum_{m,n}\sum_{p,q} S_1 e^{j\rho[k_{mn}\cos(\theta_{mn}-\theta)+k_{pq}\cos(\theta_{pq}-\theta)-k]}\,\frac{\cos(\theta_{pq}-\theta)}{R_1} \tag{5.62}$$

wherein S_1 and R_1 are written as

$$\begin{aligned} S_1 &= \frac{-j}{4\pi^2}P_{mn}k_{pq}P_{pq}\sqrt{(k_{mn}^2-k^2)(k_{pq}^2-k^2)} \\ R_1 &= \sqrt{|\vec{\boldsymbol{k}}_{mn}+\vec{\boldsymbol{k}}_{pq}|^2-2k\big(k_{mn}\cos(\theta_{mn}-\theta)+k_{pq}\cos(\theta_{pq}-\theta)\big)}. \end{aligned} \tag{5.63}$$

By adding I_5 and I_6, I_4 in (5.57) can be calculated. Notably, I_2 is similar to I_4 except for the cosine functions: by changing $\cos(\theta_{pq}-\theta)$ and $\cos(\theta_{mn}-\theta)$ respectively to $\sin(\theta_{pq}-\theta)$ and $\sin(\theta_{mn}-\theta)$, I_2 in (5.48) is acquired. By inserting I_1 and I_2 into (5.37), Term 2 is simplified as

$$\text{Term 2} = -\frac{jk}{D_t}(\eta_1-\Delta)C_0\vec{n}\cdot\left[\frac{F(\rho)e^{-jk\rho}}{2\pi\rho}\overset{xy}{*}T\left(I_1\hat{\rho}+I_2\hat{\theta}\right)\right]. \tag{5.64}$$

By calculating $\vec{n}\cdot\hat{\rho}\equiv A_1$ and $\vec{n}\cdot\hat{\theta}\equiv A_2$ in which $\vec{n}=\hat{z}-\nabla\xi$ and applying the T

operator, Term 2 in (5.64) becomes

$$\text{Term 2} = \frac{-jk}{D_t}(\eta_1 - \Delta)C_0 \Bigg[\left(\frac{F(\rho)e^{-jk\rho}}{2\pi\rho} \overset{xy}{*} I_1 \right) A_1 + \left(\frac{F(\rho)e^{-jk\rho}}{2\pi\rho} \overset{xy}{*} I_2 \right) A_2 - \frac{F(\rho)e^{-jk\rho}}{2\pi\rho} \overset{xy}{*} (A_1 I_1 + A_2 I_2) \Bigg] \equiv \frac{-jk}{D_t}(\eta_1 - \Delta)C_0 \left(T_{11}A_1 + T_{12}A_2 - T_{13} - T_{14} \right) \tag{5.65}$$

in which $T_{11} - T_{14}$ respectively correspond to each additive term inside the bracket of Term 2. According to (5.49), I_1 in T_{11} consists of two terms (i.e., I_3 and I_4). By considering these two terms, calculating the spatial convolution, using the stationary phase integration method and considering a monostatic configuration (i.e., $\rho_1 = \rho_2$), T_{11} can be expressed as

$$\begin{aligned} T_{11} = & \frac{G}{2\pi} \int_{\rho_1} F(\rho_1) e^{-jk\rho_1} I_3(\rho_1) d\rho_1 + \sum_{m,n} S_0 \sqrt{2\pi} e^{-j\pi/4} \int_{\rho_1} \frac{F^2(\rho_1) g(\theta_{mn}) e^{j\rho_1(k_{mn}-2k)}}{\rho_1^{1.5}\sqrt{k_{mn}(k_{mn}^2 - 2kk_{mn})}} d\rho_1 \\ & - \sum_{m,n} S_0 \sqrt{2\pi} \int_{\rho_1} \frac{F^2(\rho_1)}{e^{-j\pi/4}} \frac{g(\theta_{mn}+\pi) e^{-j\rho_1(k_{mn}+2k)}}{\rho_1^{1.5}\sqrt{k_{mn}(k_{mn}^2 + 2kk_{mn})}} d\rho_1 + \sum_{m,n} \sum_{p,q} S_1 \sqrt{2\pi} \int_{\rho_1} \frac{F^2(\rho_1)}{e^{j\pi/4}} \\ & \frac{g(\theta_s) e^{j\rho_1(|\vec{\boldsymbol{k}}_{mn} + \vec{\boldsymbol{k}}_{pq}| - 2k)} \cos(\theta_{pq} - \theta_s)}{\rho_1^{1.5}\sqrt{|\vec{\boldsymbol{k}}_{mn} + \vec{\boldsymbol{k}}_{pq}|}\; R_1\big|_{\theta=\theta_s}} d\rho_1 - \sum_{m,n} \sum_{p,q} S_1 \sqrt{2\pi} \int_{\rho_1} \frac{F^2(\rho_1) g(\theta_s + \pi)}{e^{-j\pi/4}\rho_1^{1.5}} \\ & \frac{e^{-j\rho_1(|\vec{\boldsymbol{k}}_{mn} + \vec{\boldsymbol{k}}_{pq}| + 2k)}}{\sqrt{|\vec{\boldsymbol{k}}_{mn} + \vec{\boldsymbol{k}}_{pq}|}\; R_1\big|_{\theta=\theta_s+\pi}} \cos(\theta_{pq} - \theta_s)\, d\rho_1. \end{aligned} \tag{5.66}$$

The same procedure is followed for calculating T_{12} since the only difference between I_4 and I_2 is the cosine functions (i.e., $\cos(\theta_{mn} - \theta)$ and $\cos(\theta_{pq} - \theta)$). Notably, the integrals containing $\sin(\theta_{mn} - \theta)$ become zero since the saddle points are located at

θ_{mn} and $\theta_{mn}+\pi$. Thus, T_{12} becomes

$$T_{12}=\sum_{m,n}\sum_{p,q}S_1\sqrt{2\pi}e^{-j\pi/4}\int_{\rho_1}\frac{e^{j\rho_1(|\vec{\boldsymbol{k}}_{mn}+\vec{\boldsymbol{k}}_{pq}|-2k)}}{\rho_1^{1.5}\sqrt{|\vec{\boldsymbol{k}}_{mn}+\vec{\boldsymbol{k}}_{pq}|}\;R_1\big|_{\theta=\theta_s}}\frac{F^2(\rho_1)g(\theta_s)}{\rho_1^{1.5}}\sin(\theta_{pq}-\theta_s)\,d\rho_1$$
$$-\sum_{m,n}\sum_{p,q}S_1\sqrt{2\pi}e^{j\pi/4}\int_{\rho_1}\frac{F^2(\rho_1)g(\theta_s+\pi)e^{-j\rho_1(|\vec{\boldsymbol{k}}_{mn}+\vec{\boldsymbol{k}}_{pq}|+2k)}}{\rho_1^{1.5}\sqrt{|\vec{\boldsymbol{k}}_{mn}+\vec{\boldsymbol{k}}_{pq}|}\;R_1\big|_{\theta=\theta_s+\pi}}\sin(\theta_{pq}-\theta_s)\,d\rho_1. \tag{5.67}$$

To calculate T_{13}, the spatial convolution in the cylindrical coordinate system is considered. Using the stationary phase method, the saddle points are located at θ_z, $\theta_z+\pi$, θ_u and $\theta_u+\pi$. θ_u is obtained by changing pq to rs in (5.35), while θ_z is acquired by adding $k_{rs}\sin\theta_{rs}$ and $k_{rs}\cos\theta_{rs}$ to the numerator and denominator of (5.35), respectively. Consequently,

$$T_{13}=\frac{-j}{\sqrt{2\pi}}\sum_{m,n}P_{mn}\sqrt{k_{mn}}\Bigg[g(\theta_{mn})e^{-j\pi/4}\int_{\rho_1}\frac{F(\rho_1)}{\sqrt{\rho_1}}I_3(\rho_1)e^{-j\rho_1(k-k_{mn})}d\rho_1$$
$$-g(\theta_{mn}+\pi)e^{j\pi/4}\int_{\rho_1}\frac{F(\rho_1)e^{-j\rho_1(k+k_{mn})}}{\sqrt{\rho_1}}I_3(\rho_1)\,d\rho_1\Bigg]+\sum_{r,s}\sum_{m,n}\sum_{p,q}\frac{P_{rs}k_{rs}S_1\sqrt{2\pi}}{\sqrt{|\vec{\boldsymbol{k}}_{rs}+\vec{\boldsymbol{k}}_{mn}+\vec{\boldsymbol{k}}_{pq}|}}$$
$$\cdot\Bigg[\int_{\rho_1}\frac{F^2(\rho_1)}{\rho_1^{1.5}}\frac{e^{j\rho_1(|\vec{\boldsymbol{k}}_{rs}+\vec{\boldsymbol{k}}_{mn}+\vec{\boldsymbol{k}}_{pq}|-2k)}g(\theta_z)}{e^{j3\pi/4}R_1\big|_{\theta=\theta_z}}\sin(\theta_{rs}-\theta_z)\cos(\theta_{pq}-\theta_z)$$

$$+\int_{\rho_1}\frac{F^2(\rho_1)e^{-j\rho_1(|\vec{\boldsymbol{k}}_{rs}+\vec{\boldsymbol{k}}_{mn}+\vec{\boldsymbol{k}}_{pq}|+2k)}}{\rho_1^{1.5}e^{-j3\pi/4}R_1\big|_{\theta=\theta_z+\pi}}\sin(\theta_z-\theta_{rs})g(\theta_z+\pi)\cos(\theta_{pq}-\theta_z)\Bigg]$$
$$+\sum_{r,s}\sum_{m,n}\frac{P_{rs}k_{rs}S_0\sqrt{2\pi}}{\sqrt{|\vec{\boldsymbol{k}}_{rs}+\vec{\boldsymbol{k}}_{mn}|}}\Bigg[\int_{\rho_1}\frac{F^2(\rho_1)}{\rho_1^{1.5}}g(\theta_u)\frac{e^{j\rho_1(|\vec{\boldsymbol{k}}_{rs}+\vec{\boldsymbol{k}}_{mn}|-2k)}\sin(\theta_{rs}-\theta_u)\cos(\theta_{mn}-\theta_u)}{e^{j3\pi/4}\sqrt{k_{mn}^2-2kk_{mn}\cos(\theta_{mn}-\theta_u)}}$$
$$+\int_{\rho_1}\frac{F^2(\rho_1)}{\rho_1^{1.5}}\frac{e^{-j\rho_1(|\vec{\boldsymbol{k}}_{rs}+\vec{\boldsymbol{k}}_{mn}|+2k)}\sin(\theta_u-\theta_{rs})\cos(\theta_{mn}-\theta_u)}{e^{-j3\pi/4}\sqrt{k_{mn}^2+2kk_{mn}\cos(\theta_{mn}-\theta_u)}}g(\theta_u+\pi)\Bigg]. \tag{5.68}$$

In Term 2, the last term that requires calculation is T_{14}. By applying the spatial

convolution in $x-y$ plane, changing the Cartesian coordinate to the cylindrical coordinate and using the stationary phase integration technique, T_{14} is calculated, which is similar to the terms containing sine and cosine functions in T_{13} such that changing all the cosine functions to the sine functions yield to T_{14}. After calculating all subordinate terms in (5.65) (i.e., $T_{11}-T_{14}$), Term 2 can be calculated.

5.2.3 Term 3

In this section, Term 3 in (5.20) is further simplified. In the first step, Λ is substituted into (5.20) and the T operator is applied to the inner bracket. By assuming the small slope approximation, Term 3 can be simplified as

$$\begin{aligned}\text{Term 3} = AC_0k^2(\eta_1-\Delta)^2\hat{n}\cdot\Bigg[\frac{F(\rho)e^{-jk\rho}}{2\pi\rho}\overset{xy}{*}\Bigg[T_{15}\hat{z}-A_1\overset{xy}{*}A_2\nabla\xi \\ -\hat{n}\Big[\nabla\xi\cdot(A_1\overset{xy}{*}A_2\nabla\xi)+T_{15}\Big]\Bigg]\Bigg]\end{aligned} \tag{5.69}$$

wherein $T_{15}=\frac{F(\rho)e^{-jk\rho}}{2\pi\rho}\overset{xy}{*}\frac{F_n(\rho)e^{-jk\rho}}{2\pi\rho}$. It is easy to show that by applying the normal vector $\hat{n}$, each term will cancel the other and Term 3 becomes zero.

5.3 First-order Backscattered E-field Calculation in the Time Domain

In this section, the backscattered fields derived in Section 5.2 are adapted by imposing a particular source excitation (here, a pulsed dipole source) to develop a proper expression for the backscattered E-field. For finding the backscattered E-field in the time domain, the inverse temporal Fourier transform is applied to each remaining term (i.e., Term 1 and Term 2), while ω is the transformed time variable and kC_0 is a function of ω. Afterwards, the first-order backscattered E-field will be the summation of Term 1 and Term 2 transformed into the time domain.

5.3.1 Backscattered E-field Derived From Term 1

By applying the inverse Fourier transform to Term 1 in (5.27) we have

$$\mathcal{F}_t^{-1}\{\text{Term 1}\}=-\mathcal{F}_t^{-1}\left(C_0 A\right) \overset{t}{*} \left(\mathcal{F}_t^{-1}(T_4)\nabla_\xi \cdot \hat{\rho} + \mathcal{F}_t^{-1}(T_5)\nabla_\xi \cdot \hat{\theta}\right) \tag{5.70}$$

in which $\overset{t}{*}$ represents time convolution and $\mathcal{F}_t^{-1}$ denotes the inverse temporal Fourier transform. Therefore, the inverse temporal Fourier transform should be applied to T_4 and T_5 by assuming that [69]

$$\mathcal{F}_t^{-1}\left[F^2(\rho,\omega)e^{-2jk\rho}\right] \simeq F^2(\rho,\omega_0)\delta(t-\frac{2\rho}{c}) \tag{5.71}$$

where ω_0 is the dominant or representative frequency of excitation and c is the speed of light. By applying the inverse Fourier transform to T_4 in (5.31) we have

$$\begin{aligned}\mathcal{F}_t^{-1}\{T_4\} &= -\frac{j\sqrt{2\pi}}{4\pi^2}\int_{\rho_1}\frac{F^2(\rho_1,\omega_0)\delta(t-\frac{2\rho_1}{c})}{\rho_1^{1.5}}(T_6+T_7+T_8)\big|_{k=k_0}\,d\rho_1 \\ &+ \frac{jG}{4\pi^2}\mathcal{F}_t^{-1}(k)\overset{t}{*}\int_{\rho_1}\frac{F^2(\rho_1)}{\rho_1}\delta(t-\frac{2\rho_1}{c})\,d\rho_1.\end{aligned} \tag{5.72}$$

The variation of $\sqrt{k_{mn}(k_{mn}^2-k^2)}$ in T_6 with respect to ω is quite small at different frequencies for Rayleigh, non-selective and Mie scatters excluding the case of $k_{mn} = \omega/c$. Consequently, its inverse temporal Fourier transform can be assumed constant, while ω is the angular frequency of the radar [46]. By the same logic, the variation of T_7 and T_8 with respect to ω is small. Therefore, only the frequency should be changed to the radar frequency in T_7 and T_8. Using the sifting property of the Dirac delta function [110], the integration over ρ_1 can be performed without difficulty, resulting in

$$\begin{aligned}\mathcal{F}_t^{-1}\{T_4\} &= -\frac{j\sqrt{2\pi}}{4\pi^2}\frac{c}{2}\frac{F^2(ct/2,\omega_0)}{(ct/2)^{1.5}}(T_6+T_7+T_8)\big|_{k=k_0,\rho_1=ct/2} \\ &+ \frac{jG}{4\pi^2}\mathcal{F}_t^{-1}(k)\overset{t}{*}\frac{F^2(ct/2,\omega_0)}{t}.\end{aligned} \tag{5.73}$$

Using the properties of the continuous-time Fourier transform, the convolution in (5.73) can be changed to multiplication and (5.73) becomes

$$\begin{aligned}\mathcal{F}_t^{-1}\{T_4\} &= -\frac{j\sqrt{2\pi}}{4\pi^2}\frac{c}{2}\frac{F^2(ct/2,\omega_0)}{(ct/2)^{1.5}}(T_6+T_7+T_8)\big|_{k=k_0,\rho_1=ct/2} \\ &+ \frac{G}{4\pi^2 c}\frac{\partial}{\partial t}\left[\frac{F^2(ct/2,\omega_0)}{t}\right].\end{aligned} \tag{5.74}$$

The next inverse Fourier transform that requires calculation is $\mathcal{F}_t^{-1}(T_5)$. By applying the inverse Fourier transform to (5.36) and employing (5.71) we have

$$\mathcal{F}_t^{-1}\{T_5\}=-\frac{j\sqrt{2\pi}}{4\pi^2}\int_{\rho_1}\frac{F^2(\rho_1,\omega_0)\delta(t-\frac{2\rho}{c})}{\rho_1^{1.5}}(T_9+T_{10})\big|_{k=k_0}d\rho_1 \tag{5.75}$$

while the variations in T_9 and T_{10} are quite small with respect to the frequency. By utilizing the sifting property of the Dirac delta function, the integration over ρ_1 can be performed as

$$\mathcal{F}_t^{-1}\left\{T_5\right\}=-\frac{j\sqrt{2\pi}}{4\pi^2}\frac{c}{2}\frac{F^2(ct/2,\omega_0)}{(ct/2)^{1.5}}(T_9+T_{10})\big|_{k=k_0,\rho_1=ct/2}. \tag{5.76}$$

In order to represent a closed-form solution for Term 1 in (5.70), the inverse Fourier transform of C_0A should be calculated. As the variation of A with respect to frequency is small, A can be taken out of the integral and only the inverse Fourier transform of C_0 should be calculated. By considering (5.8) along with the properties of Fourier transform, the inverse Fourier transform of C_0A can be written as

$$\mathcal{F}_t^{-1}\left\{C_0A\right\}=-jA\frac{\eta_0\Delta l}{c}\mathcal{F}_t^{-1}\left[\omega I(\omega)\right]=-A\frac{\eta_0\Delta l}{c}\frac{\partial}{\partial t}\left[i(t)\right] \tag{5.77}$$

in which η_0 is the intrinsic impedance of the vacuum. In the present discussion, a pulsed radar has been considered. Therefore, the antenna current can be modeled as

$$i(t)=I_0e^{j\omega_0t}\left[h(t)-h(t-\tau_0)\right] \tag{5.78}$$

wherein h represents the Heaviside function, I_0 is the magnitude of the current and τ_0 is the pulse width. By substituting (5.78) into (5.77) and neglecting the trailing edge terms, the inverse Fourier transform of $C_0 A$ can be simplified as

$$\mathcal{F}_t^{-1}\left\{C_0 A\right\} = -jkA\eta_0\,\Delta l\, I_0 e^{j\omega_0 t}\left[h(t) - h(t-\tau_0)\right]. \tag{5.79}$$

Thus, all inverse Fourier transform terms in (5.70) have been calculated. In the next step, time convolution for finding an approximate closed-form expression for the backscattered E-field derived from Term 1 should be calculated. T_4 consists of four terms and the convolution should be applied to each of them. By considering T_4 in (5.70) and splitting the convolution into four terms (i.e., $M_1 - M_4$), we have

$$\mathcal{F}_t^{-1}\left(C_0 A\right) \overset{t}{*} \left[\mathcal{F}_t^{-1}(T_4)\right] \equiv \sum_{i=1}^{4} M_i. \tag{5.80}$$

By taking the convolution in (5.80), M_1 can be obtained as

$$\begin{aligned} M_1 = L_1 \int_{t-\tau_0}^{t} \frac{F^2(ct'/2, \omega_0)}{t'\sqrt{t'c/2}} e^{j\omega_0(t-t')} \sum_{m,n} P_{mn} \sqrt{k_{mn}^3 - k^2 k_{mn}} \\ \left[g(\theta_{mn}) e^{j(c/2k_{mn}t' - \pi/4)} - g(\theta_{mn}+\pi) e^{-j(c/2k_{mn}t' - \pi/4)}\right] dt' \end{aligned} \tag{5.81}$$

wherein $L_1 = -\frac{\sqrt{2\pi}}{4\pi^2} k_0 \eta_0 \Delta l I_0 A$. Using the fact that the Sommerfeld attenuation function varies slowly over the integration range, M_1 can be calculated as

$$M_1 = \frac{c\tau_0}{2} L_1 e^{j\omega_0 t} \frac{F^2(r_0,\omega_0)}{r_0^{1.5}} \sum_{m,n} P_{mn} \sqrt{k_{mn}(k_{mn}^2 - k^2)}$$
$$\left[g(\theta_{mn}) e^{-j\pi/4} e^{-jr_0(2k_0 - k_{mn})} \operatorname{sinc}\left[\frac{\Delta\rho}{2}(2k_0 - k_{mn}) \right] \right. \tag{5.82}$$
$$\left. - g(\theta_{mn}+\pi) e^{j\pi/4} e^{-jr_0(2k_0 + k_{mn})} \operatorname{sinc}\left[\frac{\Delta\rho}{2}(2k_0 + k_{mn}) \right] \right]$$

in which $r_0 = \frac{c}{2}(t - \frac{\tau_0}{2})$ and $\Delta\rho = \frac{c\tau_0}{2}$. By applying the convolution to other terms of T_4 in (5.73), M_2 to M_4 can be calculated as follows

$$M_2 = \frac{c\tau_0}{2} L_1 e^{j(\omega_0 t - \pi/4)} \frac{F^2(r_0,\omega_0)}{r_0^{1.5}} \sum_{m,n} \sum_{p,q} P_{mn} P_{pq} k_{pq} g(\theta_s) \sqrt{(k_{mn}^2 - k_0^2)(k_{pq}^2 - k_0^2)}$$
$$\cdot \frac{e^{-j(2k_0 - |\vec{\boldsymbol{k}}_{mn} + \vec{\boldsymbol{k}}_{pq}|) r_0}}{\sqrt{|\vec{\boldsymbol{k}}_{mn} + \vec{\boldsymbol{k}}_{pq}|}} \cos(\theta_{pq} - \theta_s) \operatorname{sinc}\left[\frac{\Delta\rho}{2}(2k_0 - |\vec{\boldsymbol{k}}_{mn} + \vec{\boldsymbol{k}}_{pq}|) \right] \tag{5.83}$$

$$M_3 = -\frac{c\tau_0}{2} L_1 e^{j(\omega_0 t + \pi/4)} \frac{F^2(r_0,\omega_0)}{r_0^{1.5}} \sum_{m,n} \sum_{p,q} P_{mn} P_{pq} k_{pq} \sqrt{(k_{mn}^2 - k_0^2)(k_{pq}^2 - k_0^2)}$$
$$\frac{e^{-j(2k_0 + |\vec{\boldsymbol{k}}_{mn} + \vec{\boldsymbol{k}}_{pq}|) r_0}}{\sqrt{|\vec{\boldsymbol{k}}_{mn} + \vec{\boldsymbol{k}}_{pq}|}} g(\theta_s + \pi) \cos(\theta_{pq} - \theta_s) \operatorname{sinc}\left[\frac{\Delta\rho}{2}(2k_0 + |\vec{\boldsymbol{k}}_{mn} + \vec{\boldsymbol{k}}_{pq}|) \right] \tag{5.84}$$

$$M_4 = \frac{c\tau_0}{2} L_1 \frac{k_0 G}{\sqrt{2\pi}} e^{j\frac{\omega_0\tau_0}{2}} \frac{F^2(r_0,\omega_0)}{r_0} \operatorname{sinc}\left(\frac{\omega_0\tau_0}{2}\right). \tag{5.85}$$

The last term that should be calculated in (5.70) for finding an approximate closed-form solution for Term 1 is $\mathcal{F}_t^{-1}(C_0 A) \overset{t}{*} \left[\mathcal{F}_t^{-1}(T_5)\right]$, which can be obtained as

$$\mathcal{F}_t^{-1}\left(C_0 A\right) \overset{t}{*} \left[\mathcal{F}_t^{-1}(T_5)\right] = L_1 \frac{c\tau_0}{2} e^{j(\omega_0 t - \pi/4)} \frac{F^2(r_0,\omega_0)}{r_0^{1.5}} \sum_{m,n} \sum_{p,q} P_{mn} P_{pq} k_{pq}$$
$$\cdot \sqrt{(k_{mn}^2 - k_0^2)(k_{pq}^2 - k_0^2)} \Bigg[g(\theta_s) \frac{e^{-j(2k_0 - |\vec{\boldsymbol{k}}_{mn} + \vec{\boldsymbol{k}}_{pq}|)r_0} \operatorname{sinc}\left[\frac{\Delta\rho}{2}(2k_0 - |\vec{\boldsymbol{k}}_{mn} + \vec{\boldsymbol{k}}_{pq}|)\right]}{\sqrt{|\vec{\boldsymbol{k}}_{mn} + \vec{\boldsymbol{k}}_{pq}|}}$$
$$. \sin(\theta_{pq} - \theta_s) - g(\theta_s + \pi) \sin(\theta_{pq} - \theta_s) e^{-j(2k_0 + |\vec{\boldsymbol{k}}_{mn} + \vec{\boldsymbol{k}}_{pq}|)r_0} \frac{e^{j\pi/4}}{\sqrt{|\vec{\boldsymbol{k}}_{mn} + \vec{\boldsymbol{k}}_{pq}|}}$$
$$. \operatorname{sinc}\left[\frac{\Delta\rho}{2}(2k_0 + |\vec{\boldsymbol{k}}_{mn} + \vec{\boldsymbol{k}}_{pq}|)\right] \Bigg]. \tag{5.86}$$

By substituting (5.80) and (5.86) into (5.70), the inverse Fourier transform of Term 1 is calculated in the time domain. This term along with Term 2 constructs the first-order backscattered E-field.

5.3.2 Backscattered E-field Derived From Term 2

In order to represent a closed-form solution for Term 2, the inverse temporal Fourier transform is applied to Term 2 presented in (5.65). Therefore, we have

$$\mathcal{F}_t^{-1}\left\{\text{Term 2}\right\} = -j(\eta_1 - \Delta)\mathcal{F}_t^{-1}\left(\frac{C_0 k}{D_t}\right) \overset{t}{*} \mathcal{F}_t^{-1}\big(T_{11}A_1 + T_{12}A_2 - T_{13} - T_{14}\big). \tag{5.87}$$

Similar to (5.77), $\mathcal{F}_t^{-1}\left(\frac{C_0 k}{D_t}\right)$ can be calculated as

$$\mathcal{F}_t^{-1}\left(\frac{C_0 k}{D_t}\right) = -jk_0^2 A\big|_{k=k_0} \eta_0 \Delta l I_0 e^{j\omega_0 t}\left[h(t) - h(t-\tau_0)\right]. \tag{5.88}$$

In the next step, the inverse Fourier transform is applied to $T_{11}A_1 + T_{12}A_2 - T_{13} - T_{14}$ in (5.87).

For finding the inverse Fourier transform of $T_{11}A_1$, all the dominant terms of I_3 presented in Appendix B are substituted in T_{11} and then the inverse Fourier transform is applied to each term. After performing some derivations, the inverse Fourier transform of $T_{11}A_1$ can be expressed as

$$\mathcal{F}_t^{-1}\left(T_{11}A_1\right) = jA_1\frac{G\eta_1^4 e^{-j\pi/4}\sqrt{2\pi}}{16\pi^3(\eta_1^4-1)}\mathcal{F}_t^{-1}\sum_{i=5}^{10}M_i \tag{5.89}$$

in which

$$M_5{=}\pi c\sqrt{\frac{k_0}{ct}}F(ct,\omega_0) - \sqrt{\frac{j\pi}{1-\eta_1}}\left[\frac{F(ct,\omega_0)}{t} - j\frac{F(\frac{ct}{2},\omega_0)}{t}\right] \tag{5.90}$$

$$M_6{=}\frac{\pi c}{\eta_1^{2.5}}\sqrt{\frac{k_0}{ct}}F(\frac{ct}{\eta_1},\omega_0) - \frac{\sqrt{j\pi}}{\sqrt{1-\eta_1}}\left[\frac{F(ct,\omega_0){-}jF(\frac{ct}{\eta_1},\omega_0)}{t\eta_1^2}\right] \tag{5.91}$$

$$\begin{aligned} M_7 = {} & \frac{\pi\sqrt{ck_0}}{\sqrt{2n_u\eta_1(\eta_1-n_u)\sqrt{1+\eta_1^2}}}\frac{F(ct/n_u,\omega_0)}{\sqrt{t}}\left[\operatorname{erf}\left(e^{j\pi/4}\sqrt{\frac{k_0ct(\eta_1-n_u)}{n_u}}\right)\right. \\ & \left. - \operatorname{erf}\left(\sqrt{\frac{jk_0ct(1-n_u)}{n_u}}\right)\right] - \frac{\pi\sqrt{ck_0}}{\eta_1\sqrt{2t(\eta_1-n_u)\sqrt{1+\eta_1^2}}}F(ct/\eta_1,\omega_0) \end{aligned} \tag{5.92}$$

$$\begin{aligned} M_8 = {} & -\frac{\delta_0\sqrt{k_0}F(ct,\omega_0)}{t\sqrt{2\eta_1(1-n_u)\sqrt{1+\eta_1^2}}} - \frac{(ck_0)^{2.5}(t-tn_u)^{1.5}}{6\sqrt{2\eta_1\sqrt{1+\eta_1^2}}}F(ct,\omega_0)\big[3\pi - 3\delta_0 \\ & - \sin\delta_0(4+\cos\delta_0)\big]\Big|_{k=k_0,\rho=ct} \end{aligned} \tag{5.93}$$

$$M_9 = -j\frac{8(ck_0)^{3.5}t^{2.5}}{15\sqrt{2\eta_1\sqrt{1+\eta_1^2}}}(1-n_u)^{2.5}F(ct,\omega_0)\Bigg[\frac{5\pi}{16}-\frac{5\delta_0}{16}-\frac{\sin\delta_0}{2}+\frac{\sin^3\delta_0}{24}$$
$$-\frac{3\sin 2\delta_0}{32}\Bigg]+\frac{j(ck_0)^{1.5}\sqrt{t}}{\sqrt{2\eta_1\sqrt{1+\eta_1^2}}}\sqrt{1+n_u^2}F(ct,\omega_0)(\pi-\delta_0-\sin\delta_0)\big|_{k=k_0,\rho=ct} \tag{5.94}$$

$$\begin{aligned}
M_{10} &= \sqrt{2\pi}\sum_{m,n} S_0\big|_{k=k_0}\frac{cF^2(ct/2,\omega_0)g(\theta_{mn})e^{j(ct/2k_{mn}-\pi/4)}}{2(\frac{ct}{2})^{1.5}\sqrt{k_{mn}(k_{mn}^2-2k_0k_{mn})}}\\
&-\sqrt{2\pi}\sum_{m,n} S_0\big|_{k=k_0}\frac{cF^2(ct/2,\omega_0)g(\theta_{mn}+\pi)e^{-j(ct/2k_{mn}-\pi/4)}}{2(\frac{ct}{2})^{1.5}\sqrt{k_{mn}(k_{mn}^2+2k_0k_{mn})}}\\
&+\sqrt{2\pi}\sum_{m,n}\sum_{p,q} S_1\frac{cF^2(ct/2,\omega_0)g(\theta_s)e^{j(ct/2|\vec{\boldsymbol{k}}_{mn}+\vec{\boldsymbol{k}}_{pq}|-\pi/4)}}{2(\frac{ct}{2})^{1.5}\sqrt{|\vec{\boldsymbol{k}}_{mn}+\vec{\boldsymbol{k}}_{pq}|}\ R_1\big|_{\theta=\theta_s,k=k_0}}\cos(\theta_{pq}-\theta_s)\\
&-\sqrt{2\pi}\sum_{m,n}\sum_{p,q} S_1\frac{cF^2(ct/2,\omega_0)g(\theta_s+\pi)}{2(\frac{ct}{2})^{1.5}\sqrt{|\vec{\boldsymbol{k}}_{mn}+\vec{\boldsymbol{k}}_{pq}|}}\frac{e^{-j(ct/2|\vec{\boldsymbol{k}}_{mn}+\vec{\boldsymbol{k}}_{pq}|-\pi/4)}}{R_1\big|_{\theta=\theta_s+\pi,k=k_0}}
\end{aligned} \tag{5.95}$$

After applying the inverse Fourier transform to A_2T_{12}, $\mathcal{F}_t^{-1}\left(T_{12}A_2\right) = A_2M_{11}$ wherein M_{11} is calculated as

$$\begin{aligned}
M_{11} &= \sum_{m,n}\sum_{p,q}\frac{S_1\big|_{k=k_0}\sqrt{2\pi}e^{-j\pi/4}}{\sqrt{|\vec{\boldsymbol{k}}_{mn}+\vec{\boldsymbol{k}}_{pq}|}}\frac{e^{jct/2(|\vec{\boldsymbol{k}}_{mn}+\vec{\boldsymbol{k}}_{pq}|)}}{R_1\big|_{\theta=\theta_s,k=k_0}}\frac{F^2(ct/2,\omega_0)g(\theta_s)}{(\frac{ct}{2})^{1.5}}\sin(\theta_{pq}-\theta_s)\\
&-\sum_{m,n}\sum_{p,q} S_1\sqrt{2\pi}g(\theta_s+\pi)\frac{e^{-jct/2(|\vec{\boldsymbol{k}}_{mn}+\vec{\boldsymbol{k}}_{pq}|)}e^{j\pi/4}}{\sqrt{|\vec{\boldsymbol{k}}_{mn}+\vec{\boldsymbol{k}}_{pq}|}R_1\big|_{\theta=\theta_s+\pi,k=k_0}}\frac{F^2(ct/2,\omega_0)}{(\frac{ct}{2})^{1.5}}\sin(\theta_{pq}-\theta_s).
\end{aligned} \tag{5.96}$$

After applying the inverse Fourier transform to the first integral of T_{13} in (5.68), which is

$$\frac{e^{-j\frac{3\pi}{4}}}{\sqrt{2\pi}}\sum_{m,n}P_{mn}\sqrt{k_{mn}}g(\theta_{mn})\int_{\rho_1}\frac{F(\rho_1)}{\sqrt{\rho_1}}I_3(\rho_1)e^{-j\rho_1(k-k_{mn})}d\rho_1, \tag{5.97}$$

M_{12} is obtained. By substituting I_3 from (A.10) mentioned in Appendix B into (5.97)

and taking the inverse Fourier transform, M_{12} can be approximated as

$$M_{12}\simeq \frac{e^{-j\frac{3\pi}{4}}}{2\pi}\sum_{m,n}P_{mn}\sqrt{k_{mn}}g(\theta_{mn})\Bigg[e^{jctk_{mn}}F(ct,\omega_0)\left[\frac{\pi c}{\sqrt{ct}}-\frac{1}{t}\sqrt{\frac{j\pi}{k_0(1-\eta_1)}}\right] + e^{j\frac{ct}{\eta_1}k_{mn}}F(\frac{ct}{\eta_1},\omega_0)\left[\frac{\pi c}{\eta_1^3}\sqrt{\frac{\eta_1}{ct}}+\frac{1}{t}\sqrt{\frac{j\pi}{k_0(1-\eta_1)}}\right]+\frac{M_7}{\sqrt{k_0}}e^{j\frac{ct}{n_u}k_{mn}}+\frac{M_8+M_9}{\sqrt{k_0}}e^{jctk_{mn}}\Bigg] \tag{5.98}$$

By applying the inverse Fourier transform to the rest of T_{13}, M_{13} is acquired as follows

$$M_{13}=\sum_{r,s}\sum_{m,n}\sum_{p,q}S_1\big|_{k=k_0}\frac{cF^2(ct/2,\omega_0)}{2(\frac{ct}{2})^{1.5}}\sin(\theta_{rs}-\theta_z)\cos(\theta_{pq}-\theta_z)\frac{e^{jct/2(|\vec{\boldsymbol{k}}_{rs}+\vec{\boldsymbol{k}}_{mn}+\vec{\boldsymbol{k}}_{pq}|)}}{R_1\big|_{\theta=\theta_z,k=k_0}}$$
$$\frac{g(\theta_z)\sqrt{2\pi}e^{-j3\pi/4}}{\sqrt{|\vec{\boldsymbol{k}}_{rs}+\vec{\boldsymbol{k}}_{mn}+\vec{\boldsymbol{k}}_{pq}|}}+\sum_{r,s}\sum_{m,n}\sum_{p,q}S_1\big|_{k=k_0}\frac{cF^2(ct/2,\omega_0)}{2(\frac{ct}{2})^{1.5}}\sin(\theta_{rs}-\theta_z)e^{j3\pi/4}\cos(\theta_{pq}-\theta_z)$$
$$\frac{e^{-jct/2(|\vec{\boldsymbol{k}}_{rs}+\vec{\boldsymbol{k}}_{mn}+\vec{\boldsymbol{k}}_{pq}|)}}{R_1\big|_{\theta=\theta_z+\pi,k=k_0}}\frac{g(\theta_z+\pi)\sqrt{2\pi}}{\sqrt{|\vec{\boldsymbol{k}}_{rs}+\vec{\boldsymbol{k}}_{mn}+\vec{\boldsymbol{k}}_{pq}|}}-j\sum_{r,s}\sum_{m,n}\frac{P_{rs}k_{rs}S_0\big|_{k=k_0}\sqrt{2\pi}}{\sqrt{|\vec{\boldsymbol{k}}_{rs}+\vec{\boldsymbol{k}}_{mn}|}}\frac{cF^2(ct/2,\omega_0)}{2(\frac{ct}{2})^{1.5}}$$

$$\Bigg[g(\theta_u)e^{-j\pi/4}\frac{e^{jct/2|\vec{\boldsymbol{k}}_{rs}+\vec{\boldsymbol{k}}_{mn}|}\sin(\theta_{rs}-\theta_u)\cos(\theta_{mn}-\theta_u)}{\sqrt{k_{mn}^2-2k_0k_{mn}\cos(\theta_{mn}-\theta_u)}}+g(\theta_u+\pi)e^{j\pi/4} \frac{e^{jct/2|\vec{\boldsymbol{k}}_{rs}+\vec{\boldsymbol{k}}_{mn}|}\sin(\theta_u-\theta_{rs})\cos(\theta_{mn}-\theta_u)}{\sqrt{k_{mn}^2+2k_0k_{mn}\cos(\theta_{mn}-\theta_u)}}\Bigg]. \tag{5.99}$$

The last term that requires calculation before taking the temporal convolution in (5.87) is the inverse Fourier transform of T_{14}, which can be presented as M_{14}. The inverse Fourier transform of this term is quite similar to M_{13} except the cosine functions. In other words, by replacing the cosine functions in M_{13} with sine functions, M_{14} is acquired. After applying the inverse Fourier transform to all the terms in (5.87), the temporal convolution should be considered.

By applying the convolution and considering (5.88), the first term of Term 2 in the time domain derived from A_1T_{11} can be expressed as

$$-j(\eta_1-\Delta)\mathcal{F}_t^{-1}\left(\frac{C_0k}{D_t}\right)\overset{t}{*}\mathcal{F}_t^{-1}\left(T_{11}A_1\right)\equiv\sum_{i=15}^{20}M_i. \tag{5.100}$$

By substituting (5.88) and (5.89) into (5.100) and calculating the temporal convolution, $M_{15}-M_{19}$ are calculated as

$$\begin{aligned}M_{15}=c\tau_0M_0e^{j\omega_0t}\,\mathrm{sinc}\left(\frac{\omega_0\tau_0}{2}\right)\Bigg[\pi\sqrt{k_0}\frac{F(r_1,\omega_0)}{\sqrt{r_1}}-\frac{1}{r_1}\sqrt{\frac{\pi}{1-\eta_1}}e^{-j\omega_0\frac{r_1}{c}}\\ .\left[F(r_1,\omega_0)+F(\frac{r_1}{\eta_1},\omega_0)\right]\Bigg]\end{aligned} \tag{5.101}$$

$$\begin{aligned}M_{16}=\frac{M_0c\tau_0}{\eta_1^3}e^{j\omega_0(t-\frac{r_1}{c})}\,\mathrm{sinc}\left(\frac{\omega_0\tau_0}{2}\right).\Bigg[\pi\sqrt{k_0\eta_1}\frac{F(r_1,\omega_0)}{\sqrt{r_1}}-\sqrt{\frac{j\pi}{1-\eta_1}}\frac{\eta_1}{r_1}\\ .\left[F(r_1,\omega_0)-jF(\frac{r_1}{\eta_1},\omega_0)\right]\Bigg]\end{aligned} \tag{5.102}$$

$$\begin{aligned}M_{17}=M_0\frac{\pi c\sqrt{k_0}\,\mathrm{sinc}\left(\frac{\omega_0\tau_0}{2}\right)}{\sqrt{2n_u\eta_1(\eta_1-n_u)\sqrt{1+\eta_1^2}}}\frac{\tau_0}{\sqrt{r_1}}e^{-j\omega_0(\frac{r_1}{c}-t)}\Bigg[F(r_1/n_u,\omega_0)\\ .\,\mathrm{erf}\left(e^{j\pi/4}\sqrt{\frac{k_0r_1(\eta_1-n_u)}{n_u}}\right)-F(r_1/n_u,\omega_0)\,\mathrm{erf}\left(\sqrt{\frac{jk_0r_1(1-n_u)}{n_u}}\right)-F(r_1/\eta_1,\omega_0)\Bigg]\end{aligned} \tag{5.103}$$

$$\begin{aligned}M_{18}=-\frac{M_0c\tau_0e^{j\omega_0(t-\frac{r_1}{c})}}{\sqrt{2\eta_1\sqrt{1+\eta_1^2}}}\,\mathrm{sinc}\left(\frac{\omega_0\tau_0}{2}\right)\frac{F(r_1,\omega_0)}{r_1}\Bigg[\frac{\delta_0\sqrt{k_0}}{\sqrt{(1-n_u)}}+\frac{(r_1k_0)^{2.5}(1-n_u)}{6}\\ \left[3\pi-3\delta_0-\sin\delta_0(4+\cos\delta_0)\right]\Bigg]_{k=k_0,ct=r_1}\end{aligned} \tag{5.104}$$

$$M_{19} = -j\frac{M_0 c\tau_0 k_0^{1.5}\sqrt{r_1}}{\sqrt{2\eta_1\sqrt{1+\eta_1^2}}} e^{j\omega_0(t-\frac{r_1}{c})}\,\mathrm{sinc}\left(\frac{\omega_0\tau_0}{2}\right) F(r_1,\omega_0)\Bigg[r_1 k_0^2\Bigg(\frac{5\pi}{16} - \frac{5\delta_0}{16} - \frac{\sin\delta_0}{2} + \frac{\sin^3\delta_0}{24} - \frac{3\sin 2\delta_0}{32}\Bigg) - \sqrt{1-n_u}\,(\pi - \delta_0 - \sin\delta_0)\Bigg]_{k=k_0, ct=r_1} \tag{5.105}$$

wherein $M_0 = (jA_1 G\eta_1^4 e^{-j\pi/4}\sqrt{2\pi})/(16\pi^3(\eta_1^4-1))$ and $r_1 = r_0/2$. By taking the temporal convolution between (5.88) and the last term of $\mathcal{F}_t^{-1}(T_{11}A_1)$, which is M_{10}, M_{20} is acquired. M_{20} is obtained by applying some changes in M_{10}. By multiplying M_{10} by $A_1\tau_0 e^{j(\omega_0 t - 2r_0k_0)}$, changing $\frac{ct}{2}$ to r_0 and considering the sinc functions derived from the convolution, M_{20} is obtained.

The second term of Term 2 in the time domain, which is represented by M_{21}, is calculated by taking the temporal convolution between (5.88) and M_{11}. M_{21} is obtained by applying some changes in M_{11}. By multiplying M_{11} to $A_2\tau_0 e^{j(\omega_0 t - 2r_0k_0)}$, changing $\frac{ct}{2}$ to r_0 and multiplying $\mathrm{sinc}\left(\frac{\Delta\rho}{2}(2k_0 - |\vec{\boldsymbol{k}}_{mn} + \vec{\boldsymbol{k}}_{pq}|)\right)$ and $\mathrm{sinc}\left(\frac{\Delta\rho}{2}(2k_0 + |\vec{\boldsymbol{k}}_{mn} + \vec{\boldsymbol{k}}_{pq}|)\right)$, respectively, by the first and the second term of M_{11}, M_{20} is obtained, while $\Delta\rho = c\tau_0/2$. The third term of Term 2 in the time domain, which is denoted by M_{22}, is calculated by taking the temporal convolution between (5.88) and both M_{12} and M_{13}. By multiplying M_{12} and M_{13} by $\tau_0 e^{j(\omega_0 t - 2r_0k_0)}$, changing $\frac{ct}{2}$ to r_0 and considering the sinc functions derived from the convolution, M_{22} is obtained.

The last term of Term 2 in the time domain, which is represented by M_{23}, is quite similar to the terms containing cosine and sine functions in M_{22}. In other words, by replacing the cosine functions in M_{22} with the sine functions, M_{23} is attained. Consequently, the scattered E-field derived from Term 2 in the time domain can be

calculated from the summation of all the calculated terms as

$$\text{Term } 2(t) = -(\eta_1 - \Delta)k_0^2\eta_0\Delta l I_0 A\big|_{k=k_0} \sum_{i=15}^{23} M_i. \tag{5.106}$$

The polarization of the incident and scattered E-field is assumed to be similar in our derivations. In other words, cross-polarized scattered fields are approximately neglected. Therefore, the summation of Term 1 and Term 2 corresponds to the co-polarized backscattered E-field. The radar cross-section can be calculated from the received power in the receiver antenna by considering the Gaussian distribution [108] for the random rough surface as [69]

$$P_r = \frac{A_r}{2\eta_0} < (E_n^+)_1(t)\ (E_n^+)_1^*(t) > \tag{5.107}$$

where $A_r = k_0^2 G_r$ is the effective aperture of the receiving antenna and can be calculated using the free space gain of the receiving antenna (G_r). By considering the received and transmitted power along with the radar equation [1], the incoherent co-polarized radar cross-section for the time-invariant rough surface can be calculated

as

$$\sigma_s = \frac{32\pi^3 l^2 h^2}{\eta_0^2 k_0^2}\Bigg[\frac{3k_0^6}{\alpha^4}\eta_0^2 F^4(r_0,\omega_0)W(2\beta_3)+\frac{k_0\eta_0^2\gamma}{16\pi\alpha^4}F^4(r_0,\omega_0)+\frac{\gamma F^4(r_0,\omega_0)}{32k_0\alpha^4}$$
$$+4\pi^2 r_0^2 F^2(r_1,\omega_0)k_0^2 W(\beta_3)+\frac{8\pi k_0 r_0}{1-\eta_1}W(\beta_3)F^2(r_1,\omega_0)+\frac{4\pi k_0 r_0^2}{1-\eta_1}\eta_1^3 W(\beta_3\eta_1)F^2(\frac{r_1}{\eta_1},\omega_0)$$
$$+\frac{4r_0^2}{\eta_1^2}\pi^2 k_0^2 W(\beta_3\eta_1)F^2(\frac{r_1}{\eta_1},\omega_0)+\frac{2\eta_1 r_0^2}{n_u(\eta_1-n_u)}\pi^2 k_0 F^2(\frac{r_1}{\eta_1},\omega_0)\Big[n_u+|\operatorname{erf}(\beta_1)|^2$$
$$+|\operatorname{erf}(\beta_2)|^2\Big]+\frac{2k_0^2}{\eta_1^2}r_0^3 W(\beta_3)F^2(r_1,\omega_0)\Big[\frac{\delta_0^2}{2r_1^2(1-n_u)}+\frac{k_0^4}{72}r_1^3(1-n_u)^3\big(3\pi-3\delta_0$$
$$-\sin\delta_0(4+\cos\delta_0)^2\big)\Big]+\frac{\pi}{\eta_1^2}k_0^4 F^2(r_1,\omega_0)W(\beta_3)\Big[r_1^5 k_0^4(1-n_u)^5(\frac{5\pi}{16}-\frac{5\delta_0}{16}-\frac{\sin\delta_0}{2}$$
$$+\frac{\sin^3\delta_0}{24}-\frac{3\sin 2\delta_0}{32})^2+\pi r_1(1+n_u)(\pi-\delta_0-\sin\delta_0)^2\Big]\Bigg] \tag{5.108}$$

where $W(\cdot)$ is the surface spectral density for the stationary Gaussian height distribution with correlation length l and RMS height h, $\alpha = l\sin\theta_i$, $\beta_1 = \sqrt{\frac{jk_0 r_1(\eta_1-n_u)}{n_u}}$, $\beta_2 = \sqrt{\frac{jk_0 r_1(1-n_u)}{n_u}}$, $\beta_3 = k_0 l\sin\theta_i$ and θ_i is the incident angle.

It is important to note that only specular reflection can be considered for the coherent wave scattering. Therefore, it is expected to have a significant co-polarized backscattered fields at zero angle for the monostatic configuration.

5.4 Results

In this section, the new development for the first-order backscattered E-field is evaluated by comparing the first-order radar cross-section with three analytical solutions (i.e., the SPM, KA and SSA solutions). The MoM as a numerical method is employed

Table 5.1: Media characteristics

Parameters	Seawater	Sea ice
σ (S/m)	4.00	10^{-3}
ϵ_r	80.00	4.00
$\lvert\eta_1^2\rvert$	2399.15	4.04
$\tan\delta$	29.97	0.15
f (MHz)	30	30

to show the accuracy of the proposed solution for the first-order backscattered E-field. In order to validate the proposed solution, two different media with different permittivities and conductivities listed in Table 5.1 as high and moderate contrast media at 30 MHz are selected for Region 1. As is obvious in this table, the refractive index and loss tangent ($\tan\delta_1$) of seawater are relatively high while they are quite small for sea ice at 30 MHz. Therefore, seawater and sea ice can be assumed as high and moderate contrast media with respect to air, respectively.

It is also worth noting that the proposed scattering solution does not have a frequency constraint since the band-limited assumption ($|k_x^2 + k_y^2| < k^2$) has not been retained in the derivation of the scattered E-field. In order to assess the proposed solution for different roughness heights, various Gaussian random rough surfaces with different RMS heights (h_{RMS}), correlation lengths and roughness scales (kh_{RMS}) are considered. Table 5.2 illustrates all the parameters associated with the defined Gaussian random rough surfaces. The length and the width of all the random rough surfaces have been assumed as 10λ (to be sizable in terms of the wavelength), while the sampling rate of the surface has been set to 5 points per square wavelength. For

instance, Fig. 5.4(a) shows a generated random rough surface with the parameters listed in Table 5.2 for the second defined rough surface in only one-dimension. In order to evaluate the distribution of this surface, the probability density function (PDF) of the generated surface has been obtained and compared with the theoretical PDF. As can be seen in this figure, the probability density of the generated random rough surface is close to the theoretical PDF. In order to show the robustness of the results

Table 5.2: Random rough surface parameters

Surface	RMS height (m)	Correlation length (m)	kh_{RMS}
1	0.40	5.50	0.25
2	1.25	5.00	0.79
3	2.20	5.20	1.38
4	3.00	7.20	1.90

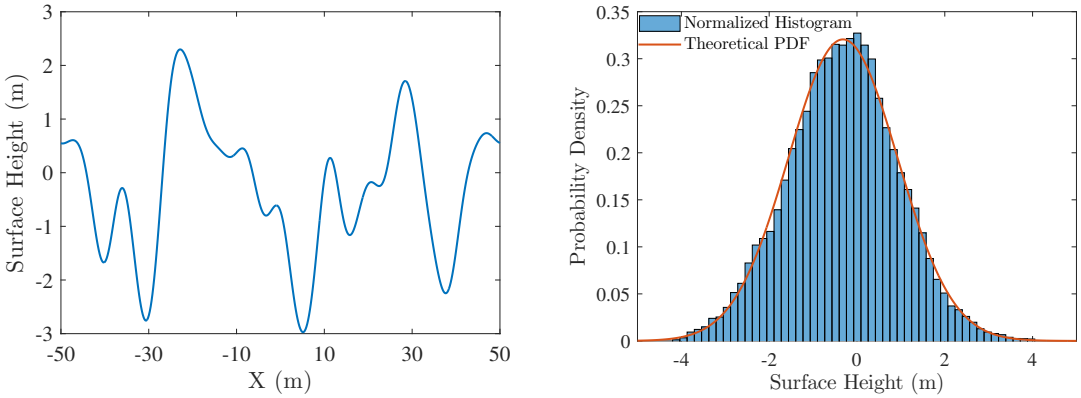

(a) (b)

Fig. 5.4: (a) Surface realization with RMS height of 1.25 m and correlation length 5 m as defined for the second rough surface. (b) The probability density of the generated random rough surface and its comparison with the theoretical probability density.

against media characteristics, the electromagnetic properties of the selected random

rough surfaces in Table 5.2 are changed to seawater as high contrast and sea ice as moderate contrast media. Subsequently, the radar cross-section is calculated at different incident angles and compared with the analytical solutions, while the numerical solution obtained by the MoM is considered as reference. Monte Carlo simulation over 100 sample rough surfaces is performed for finding the radar cross-section using the MoM. It should be pointed out that all the defined random rough surfaces have a finite extent. Therefore, edge diffraction occurs due to the edge of the surface. In order to reduce the edge diffraction for the scattering from rough surfaces, a tapered incident wave [111] with tapering parameter g is utilized in the numerical analysis. In this investigation, the tapering parameter g has been set to 25 m at 30 MHz in the numerical analysis.

5.4.1 Seawater

To evaluate the performance of the proposed solution at different incident angles over high contrast media, the solution is applied to two-dimensional random rough seawater surfaces listed in Table 5.2. Fig. 5.5 depicts the radar cross-section of four selected random rough surfaces at different incident angles. In this figure, the SPM, KA and SSA solutions are referred to as the first-order radar cross sections acquired by SPM, KA and SSA methods, respectively. Although higher-order scattering of SPM [112], KA [56] and SSA [113] may improve their accuracy compared to the MoM method, only the first-order scattering has been considered in this study to be comparable with

the proposed solution derived from the first-order scattering. As can be seen in this figure, the proposed solution can follow the numerical and more accurate solution (i.e., the MoM) at different incident angles, while the RMS heights are increased. It should be noted that the solutions acquired by the MoM consider both coherent and incoherent scattered fields, in which coherent scattering corresponds to the specular reflection around zero incident angles. However, in the other solutions, only incoherent wave scattering phenomenon has been considered. On the other hand, in remote sensing and radar applications, the matched polarization (i.e., considering only co-polarized scattered fields) in the receiver is one of the ways to increase the signal-to-noise ratio (SNR). Consequently, the scattered fields possessing the TM polarization [72] were considered in this study for the calculation of the radar cross section. Accordingly, the co-polarized radar cross-section is obtained for the all defined random rough surfaces listed in Table 5.2. Fig. 5.5(a) shows the radar cross-section of the first random rough surface listed in Table 5.2. As can be seen in this figure, the proposed solution along with other approximate solutions is close to each other and follow the MoM solution at various incident angles except for near $\theta = 0$. For this surface, the RMS height is much smaller than the source wavelength, while the radius of curvature is relatively greater than the source wavelength. As a result, the SPM, KA and SSA solutions are close to the MoM solution. By increasing the RMS height to 1.25 m in the second random rough surface mentioned in Table 5.2, discrepancies between the SPM and MoM solution increase as shown in Fig. 5.5(b). The KA and SSA solutions

remain credible at various incident angles. Nonetheless, the proposed solution for this surface is better than the KA and SSA solutions at different incident angles and has a good agreement with the MoM solution. By increasing the roughness height, as we defined in the third random rough surface, the discrepancies between SPM and the KA and SSA solutions increase, while the proposed solution can follow the numerical solution at various incident angles. For the last random rough surface listed in Table 5.2, the RMS height has been increased to 3 m. As can be seen in Fig. 5.5(d), the proposed solution agrees well with the MoM solution at various incident angles and outperforms the SPM, KA and SSA solutions for the large roughness height.

5.4.2 Sea Ice

In order to assess the performance of the proposed solution for the backscattered E-field over moderate contrast media, the new development is applied to different random rough sea ice surfaces with the parameters listed in Table 5.1, while only co-polarized scattered fields are considered in the calculation of the radar cross section. Similar to seawater, the SPM, KA, SSA and MoM solutions are used to show the accuracy of the proposed solution at different incident angles. As is obvious in this figure, the proposed solution follows the numerical solution at various incident angles and RMS heights. Fig. 5.6(a) depicts the radar cross-section over the first defined random rough surface mentioned in Table 5.2. The proposed and other analytical solutions follow the numerical solution at different incident angles, particularly below

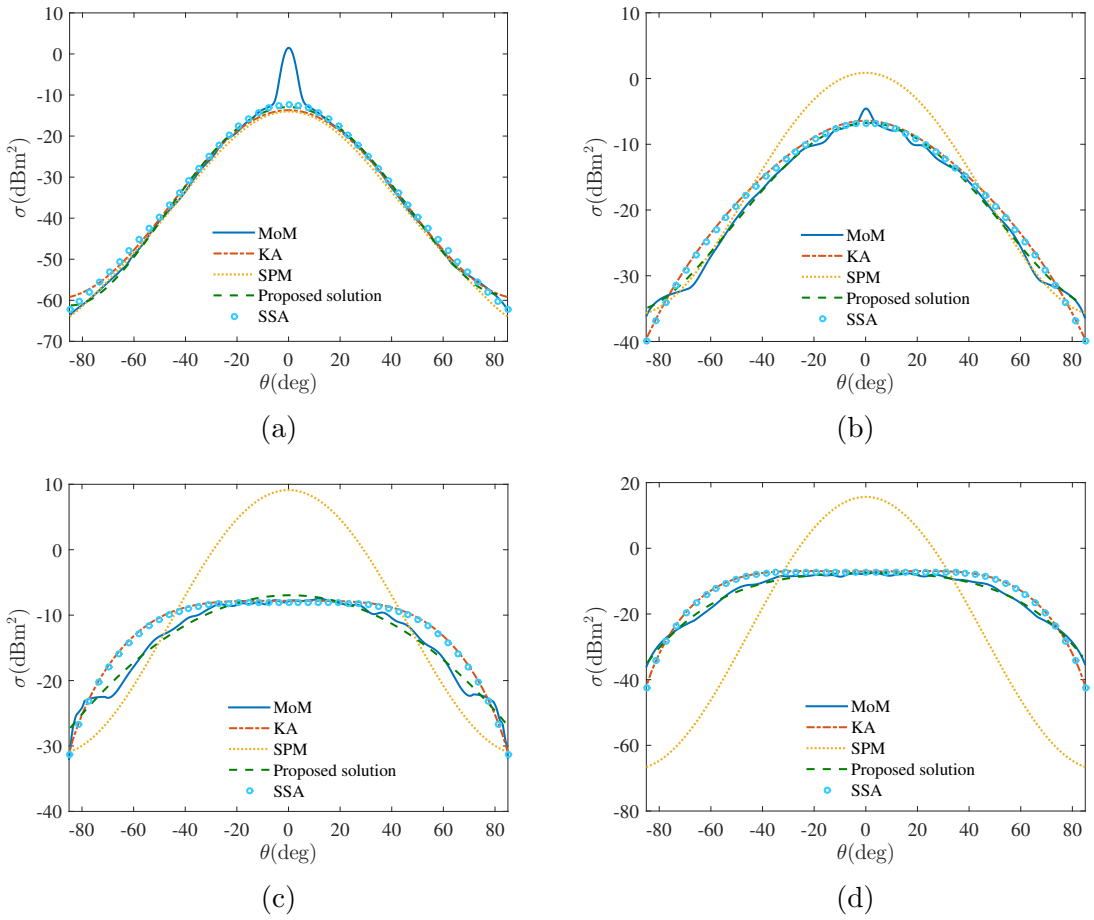

Fig. 5.5: The radar cross-section and its comparison with the other solutions over seawater with a) $kh_{RMS} = 0.25$ b) $kh_{RMS} = 0.79$ c) $kh_{RMS} = 1.38$ d) $kh_{RMS} = 1.9$.

40 degrees. The SPM, KA and SSA solutions are reasonably good at different incident angles since the RMS height of this surface is small, and the radius of curvature is greater than the source wavelength for this random rough surface. For the second random rough surface, the RMS height is increased to 1.25 m. Fig. 5.6(b) shows the radar cross-section of this surface at various incident angles. The discrepancies between the numerical and other analytical solutions have increased in this figure. Nevertheless, the proposed solution agrees well with the MoM solution and outper-

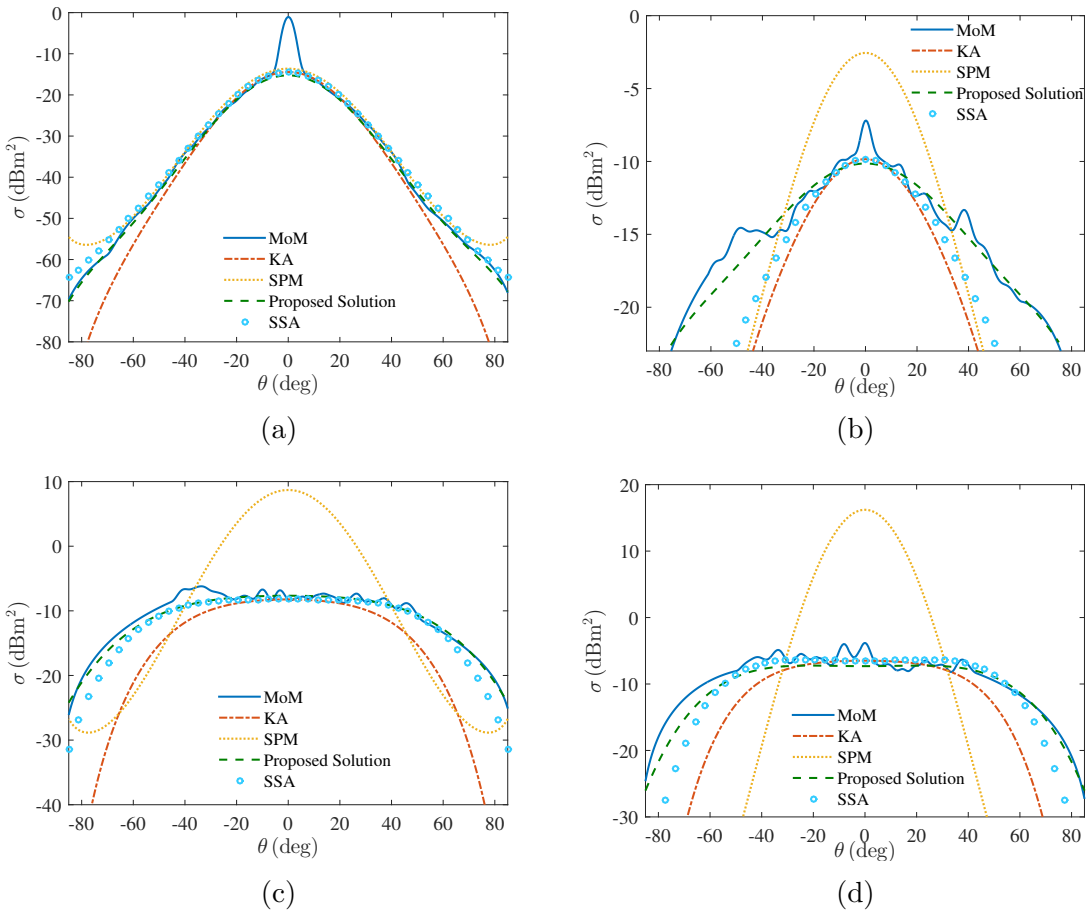

Fig. 5.6: The radar cross-section and its comparison with the other solutions over sea ice with a) $kh_{RMS} = 0.25$ b) $kh_{RMS} = 0.79$ c) $kh_{RMS} = 1.38$ d) $kh_{RMS} = 1.9$.

forms the conventional solutions at different incident angles. Fig. 5.6(c) demonstrates the radar-cross section and its comparison for the third defined random rough surface characterized in Table 5.2. As is obvious, the proposed solution follows the MoM solution at various incident angles, and the SSA solution remains credible for low incident angles. On the other hand, the SPM and KA solutions cannot follow the numerical solution due to the large value of RMS height. The radar cross-section over the last random rough surface with the RMS height of 3 m has been depicted in Fig.

5.6(d). In this figure, the proposed solution outperforms other analytical solutions (SPM, KA and SSA) and can follow the numerical solution at various incident angles.

It should be noted that the computation time of the MoM solution for each random rough surface is almost constant with respect to the roughness scale (kh_{RMS}), and it only varies by changing the electromagnetic properties of the surface. For rough seawater surfaces, the computation time using a computer equipped with a core i7-4700MQ CPU clocked at 2.40 GHz and 16 GB RAM memory is around 52 min, while it is about 2 h 42 min for rough sea ice surfaces. It is important to note that 5 points per square wavelength have been used for the rough surface in our investigation. The computation time for the numerical calculations considerably increases if we increase this amount. For instance, if the sampling rate is increased to 20 to have a better rough surface resolution, it takes around a day to compute the results for the rough sea ice surfaces.

5.5 Chapter Summary

The scattered E-field is derived from a general operator equation and represented in the form of an integral equation containing the normal component of the E-field for arbitrary radiation source and rough surface profile. By representing a new formulation for the terms associated with the moderate contrast media and incorporating large RMS height factor, the backscattered E-field by assuming a vertical dipole antenna located above the scattering surface is obtained. By utilizing the Fourier series solution

of the scattering surface, the first-order backscattered E-field and incoherent radar cross section are calculated. A numerical evaluation of the proposed solution and its comparison with three alternative analytical solutions(i.e., the SPM, KA and SSA methods) indicate that the proposed solution outperforms the conventional solutions for large roughness height and a verity media characteristics.

Chapter 6

Conclusion

6.1 Summary

The objectives of this thesis have been: 1) to develop approximate analytical solutions for the scattered EM fields radiated by a VED in the presence of a lossy half-space with a smooth interface at various frequencies and distances from the antenna for plasmonic and non-plasmonic structures; and 2) to develop an approximate analytical solution for EM scattering over two-dimensional random rough surfaces with large roughness height and different contrast media.

First of all, the intermediate Hertz potential and scattered fields are derived for frequencies below the VHF band above a lossy half-space with a smooth interface. By decomposing the intermediate Hertz potential into three terms and proposing approximate solutions for each term at various distances from the antenna, the solution for the intermediate Hertz potential associated with the Sommerfeld-type integral is

acquired. A numerical evaluation of the integrals that constitute the formal result of the problem validates the accuracy and efficiency of the proposed solution at various frequencies and distances from the antenna. Furthermore, the overall behavior of the solution is illustrated for the particular case of ocean surface scattering in the HF frequency band in the near and far field regions.

Secondly, the Sommerfeld half-space problem with a smooth interface is revisited and accurate solutions for the intermediate Hertz potential and scattered electric field are derived for higher frequencies (up to 10 GHz) in the near and far field regions. The intermediate Hertz potential is decomposed into two Sommerfeld-type integrals and accurate solutions are proposed for good dielectric and conductor media by employing the small and large argument approximation of the Bessel function of the first kind in the Sommerfeld-type integrals. By finding an approximate closed-form solution for the intermediate Hertz potential, the scattered electric field in the near and far field regions is calculated. To evaluate the accuracy of the theoretical development, the scattered electric field over different lossy half-spaces (i.e., seawater, wet earth, dry earth and lake water) is obtained and compared with two alternative state of the art solutions at various frequencies and distances from the antenna in terms of the normalized root-mean-square error (NRMSE) and mean absolute error (MAE), while the numerical solution is considered as a reference.

Following this work, new approximate solutions for the scattered electric and magnetic field components for plasmonic and non-plasmonic media over a lossy half-space

with a smooth interface have been proposed. The modified saddle-point method is utilized to represent an approximate closed-form solution for the intermediate Hertz potential expressed in terms of the Fourier-Bessel transforms associated with the Sommerfeld-type integral. The scattered fields including surface waves in the far field region are calculated from the intermediate Hertz potential. To assess the efficiency of the developed formulations, radiation patterns of different impedance half-planes are obtained for plasmonic (e.g., silver and gold) and non-plasmonic (e.g., seawater, silty clay soil, silty loam soil and lake water) media. In terms of accuracy, the proposed solutions for the scattered fields are evaluated by the NRMSE and normalized maximum absolute error (NMAE) using the numerical solution and compared with two alternative state of the art solutions for plasmonic and ordinary structures.

Finally, random roughness is added to the problem and the formulations for EM wave scattering over a two-dimensional random rough surface with different roughness heights and contrast media are derived based on the generalized functions approach. The scattered electric field is derived for an arbitrary radiation source, and surface profile and incorporates all scattering orders obtained from the Neumann series solution. Afterwards, the first-order scattered electric field and radar-cross section are calculated for a Gaussian random rough surface distribution with different RMS heights and correlation lengths. The proposed solutions for the backscattered E-field and the radar cross-section do not have a constraint over the roughness height and can be applied to surfaces with large roughness heights. However, the other analytical

solutions, such as the SPM, KA and SSA methods are unable to accurately calculate scattered fields. In addition, the proposed solution is applicable for rough surfaces with moderate contrasts, while the other alternative analytical solutions (i.e., the SPM, KA and SSA methods) are well accurate only for high contrast media. In order to show the efficiency of the proposed solution, a numerical evaluation of the solution and its comparison with three alternative analytical solutions (i.e., the SPM, KA and SSA methods) are acquired. The comparisons indicate that the proposed solution outperforms the conventional solutions for large roughness height and a verity media characteristics.

The main contribution of this work is the development of various approximate analytical solutions for the scattered EM fields over a lossy half-space including smooth and rough interfaces at various frequencies and distances from the antenna in the near and far field regions. These solutions can be used in a verity of forward and inverse scattering problems, such as ocean remote sensing, GPR applications, medical imaging, wireless communication link design, retrieving soil moisture and vegetation biomass. Moreover, the proposed solutions for the scattered fields from rough surfaces are valid for high roughness height and different contrast media for which the refractive index is greater than one. Therefore, scattered EM fields can be acquired not only for high but also for moderate contrast media such as sea ice and soil.

6.2 Suggestions for Future Works

Based on the work presented in this thesis, several remaining problems are discussed here with suggestions for future theoretical work.

First, approximate analytical solutions over half-spaces have been obtained for homogeneous and isotropic media. These solutions can be developed for inhomogeneous anisotropic media when the source is a vertical or horizontal dipole antenna. For isotropic media, the electric and magnetic flux density are respectively related to the electric and magnetic field by a number. However, for anisotropic media, they are related through dielectric permittivity and permeability tensors. Therefore, dyadic analysis [114] is required in the derivation of scattered EM fields. Also, for inhomogeneous media, the EM properties are a function of position and depend on x, y or z in the Cartesian coordinate system and should be considered in the derivation of the scattered EM fields.

Second, for the EM scattering by random rough surfaces, higher-order scattered E-fields and radar-cross sections can be developed. Higher order fields may increase the accuracy of the solution compared with the numerical solutions. In this case, a higher-order Neumann series solution for the scattered E-field should be considered.

Third, in the calculation of the scattered E-field by random surfaces, the small slope condition has been considered. By removing this constraint, the scattered E-field can be calculated for general rough surface profiles with different slopes.

Fourth, the scattered electric field has been obtained over a time-invariant random rough surface. The existing derivations for the scattered electric field can be developed for time- and space-variant random rough surfaces. In order to consider a time-variant random surface, an exponential function $e^{j\omega_k t}$, in which ω_k is the angular frequency of the surface variation, needs to be integrated with the Fourier series representation of the scattering surface.

Finally, scattered EM fields can be developed for layered media with rough interfaces since most real structures, such as soil, can be modeled as layered media. Also, developing high-order (e.g., the second and the third order scattering) scattered fields for large scale and moderate contrast random rough surfaces and comparing with other unifying methods such as the advanced integral equation method (AIEM) can be considered as possible future work.

References

[1] M. E. Nazari and A. Ghorbani, "Predicting a three-dimensional radar coverage area : Introducing a new method based on propagation of radio waves." *IEEE Antennas Propag. Mag.*, vol. 58, no. 1, pp. 28–34, Feb 2016.

[2] K. A. Michalski and J. R. Mosig, "Multilayered media Green's functions in integral equation formulations," *IEEE Trans. Antennas Propag.*, vol. 45, no. 3, pp. 508–519, March 1997.

[3] D. H. Werner, *Broadband Metamaterials in Electromagnetics: Technology and Applications*. Florida, United States: CRC Press, 2017.

[4] M. E. Nazari, W. Huang, and C. Zhao, "Radio frequency interference suppression for HF surface wave radar using CEMD and temporal windowing methods," *IEEE Geosci. Remote Sens. Lett.*, vol. 17, no. 2, pp. 212–216, Feb 2020.

[5] H. Liu, K. Takahashi, and M. Sato, "Measurement of dielectric permittivity and thickness of snow and ice on a brackish lagoon using GPR," *IEEE J. Sel. Topics Appl. Earth Observ.*, vol. 7, no. 3, pp. 820–827, March 2014.

[6] L. Novotny, "Allowed and forbidden light in near-field optics. i. a single dipolar light source," *J. Opt. Soc. Am. A*, vol. 14, no. 1, pp. 91–104, Jan 1997.

[7] T.-I. Jeon and D. Grischkowsky, "THz zenneck surface wave (THz surface plasmon) propagation on a metal sheet," *Appl. Phys. Lett.*, vol. 88, no. 6, pp. 061 113–1–061 113–3, 2006.

[8] B. Ung and Y. Sheng, "Optical surface waves over metallo-dielectric nanostructures: Sommerfeld integrals revisited," *Opt. Exp.*, vol. 16, no. 12, pp. 9073–9086, Jun 2008.

[9] A. Y. Nikitin, S. G. Rodrigo, F. J. Garcia-Vidal, and L. Martin-Moreno, "In the diffraction shadow: Norton waves versus surface plasmon polaritons in the optical region," *New J. Phys.*, vol. 11, no. 12, p. 123020, Dec 2009.

[10] E. Pettinelli, P. Burghignoli, A. R. Pisani, F. Ticconi, A. Galli, G. Vannaroni, and F. Bella, "Electromagnetic propagation of GPR signals in martian subsurface scenarios including material losses and scattering," *IEEE Trans. Geosci. Remote Sens.*, vol. 45, no. 5, pp. 1271–1281, 2007.

[11] R. W. P. King, B. H. Sandler, and L. C. Shen, "A comprehensive study of subsurface propagation from horizontal electric dipoles," *IEEE Trans. Geosci. Remote Sens.*, vol. GE-18, no. 3, pp. 225–233, 1980.

[12] Y. Du, *Electromagnetic scattering: A remote sensing perspective.* World scientific, 2017.

[13] D. Zahn, K. Sarabandi, K. F. Sabet, and J. F. Harvey, "Numerical simulation of scattering from rough surfaces: a wavelet-based approach," *IEEE Trans. Antennas Propag.*, vol. 48, no. 2, pp. 246–253, 2000.

[14] K. Li and Y. Lu, "Electromagnetic field generated by a horizontal electric dipole near the surface of a planar perfect conductor coated with a uniaxial layer," *IEEE Trans. Antennas Propag.*, vol. 53, no. 10, pp. 3191–3200, Oct 2005.

[15] K. A. Michalski and J. R. Mosig, "On the surface fields excited by a Hertzian dipole over a layered halfspace: From radio to optical wavelengths," *IEEE Trans. Antennas Propag.*, vol. 63, no. 12, pp. 5741–5752, Dec 2015.

[16] M. E. Nazari and W. Huang, "An analytical solution of electromagnetic radiation of a vertical dipole over a layered half-space," *IEEE Trans. Antennas Propag.*, vol. 68, no. 2, pp. 1181–1185, Feb 2020.

[17] M. Eslami Nazari and W. Huang, "An analytical solution of the electric field excited by a vertical electric dipole above a lossy half-space: From radio to microwave frequencies," *IEEE Trans. Antennas Propag.*, vol. 68, no. 11, pp. 7517–7529, 2020.

[18] M. E. Nazari and W. Huang, "Asymptotic solution for the electromagnetic scattering of a vertical dipole over plasmonic and non-plasmonic half-spaces," *IET Microw. Antennas Propag.*, vol. 15, no. 7, pp. 704–717, 2021.

[19] A. Sommerfeld, "Propagation of waves in wireless telegraphy," *Ann. Phys.*, vol. 28, pp. 665–736, March 1909.

[20] A. Ishimaru, J. D. Rockway, and S. W. Lee, "Sommerfeld and zenneck wave propagation for a finitely conducting one-dimensional rough surface," *IEEE Trans. Antennas Propag.*, vol. 48, no. 9, pp. 1475–1484, Sep. 2000.

[21] W. H. Wise, "Sommerfeld and zenneck wave propagation for a finitely conducting one-dimensional rough surface," *Bell Syst. Tech. J.*, vol. 8, no. 4, pp. 662–671, Oct. 1929.

[22] B. Van Der Pol, "Theory of the reflection of the light from a point source by a finitely conducting flat mirror, with an application to radiotelegraphy," *Physica*, vol. 2, no. 1, pp. 843–853, 1935.

[23] K. A. Norton, "The propagation of radio waves over the surface of the earth and in the upper atmosphere," *Proc. IRE*, vol. 25, no. 9, pp. 1203–1236, Sep. 1937.

[24] J. R. Wait, "The ancient and modern history of EM ground-wave propagation," *IEEE Trans. Antennas Propag.*, vol. 40, no. 5, pp. 7–24, Oct. 1998.

[25] P. R. Bannister, "New formulas that extend Norton's farfield elementary dipole equations to the quasi-nearfield range," Naval Underwater Syst. Center, New London, CT, USA, Tech. Rep. 6883, Tech. Rep., Jan. 1984.

[26] B. L. Van Der Waerden, "On the method of saddle points," *Appl. Sci. Res. B*, vol. 2, no. 1, pp. 33–45, Dec 1952.

[27] G. Bernard and A. Ishimaru, "On complex waves," *Electrical Engineers, Proceedings of the Institution of*, vol. 114, pp. 43–49, 02 1967.

[28] R. E. Collin, "Hertzian dipole radiating over a lossy earth or sea: some early and late 20th-century controversies," *IEEE Trans. Antennas Propag.*, vol. 46, no. 2, pp. 64–79, April 2004.

[29] J. R. Wait, "Radiation from a vertical electric dipole over a stratified ground," *IRE Trans. Antennas Propag.*, vol. AP-1, pp. 9–12, 1953.

[30] ——, "Electromagnetic surface waves," *in Advances in Radio Research*, vol. 1, J. A. Saxton, Ed. San Diego, CA, USA: Academic, pp. 157–217, 1964.

[31] R. J. King and G. A. Schlak, "Groundwave attenuation function for propagation over a highly inductive earth," *Radio Sci.*, vol. 2, no. 7, pp. 687–693, 1967.

[32] R. J. King, "Electromagnetic wave propagation over a constant impedance plane," *Radio Science*, vol. 4, no. 3, pp. 255–268, 1969.

[33] H. E. Green, "Derivation of the Norton surface wave using the compensation theorem," *IEEE Antennas Propag. Mag.*, vol. 49, no. 6, pp. 47–57, 2007.

[34] R. W. P. King and S. S. Sandler, "The electromagnetic field of a vertical electric

dipole over the earth or sea," *IEEE Trans. Antennas Propag.*, vol. 42, no. 3, pp. 382–389, 1994.

[35] ——, "The electromagnetic field of a vertical electric dipole in the presence of a three-layered region," *Radio Sci.*, vol. 29, no. 1, pp. 97–113, 1994.

[36] R. W. P. King, "Electromagnetic field of a vertical dipole over an imperfectly conducting half-space," *Radio Sci.*, vol. 25, pp. 149–160, 1990.

[37] R. E. Collin, "Some observations about the near zone electric field of a Hertzian dipole above a lossy earth," *IEEE Trans. Antennas Propag.*, vol. 52, no. 11, pp. 3133–3137, Nov 2004.

[38] S. F. Mahmoud, R. W. P. King, and S. S. Sandler, "Remarks on "the electromagnetic field of a vertical electric dipole over the earth or sea" [and reply]," *IEEE Trans. Antennas Propag.*, vol. 47, no. 11, pp. 1745–1747, Nov 1999.

[39] H. Q. Zhang and W. Y. Pan, "Electromagnetic field of a vertical electric dipole on a perfect conductor coated with a dielectric layer," *Radio Sci.*, vol. 37, no. 4, pp. 13–1–13–7, 2002.

[40] H. Q. Zhang, K. Li, and W. Y. Pan, "The electromagnetic field of a vertical dipole on the dielectric-coated imperfect conductor," *J. Electromagn. Waves Appl.*, vol. 18, no. 10, pp. 1305–1320, 2004.

[41] K. Sarabandi, M. D. Casciato, and I. S. Koh, "Efficient calculation of the fields of

a dipole radiating above an impedance surface," *IEEE Trans. Antennas Propag.*, vol. 50, no. 9, pp. 1222–1235, 2002.

[42] P. Parhami, Y. Rahmat-Samii, and R. Mittra, "An efficient approach for evaluating Sommerfeld integrals encountered in the problem of a current element radiating over lossy ground," *IEEE Trans. Antennas Propag.*, vol. 28, no. 1, pp. 100–104, January 1980.

[43] K. A. Michalski, "On the efficient evaluation of integral arising in the Sommerfeld halfspace problem," *IEE Proc. Part H-Microwaves, Antennas and Propagat.*, vol. 132, pp. 312–318, August 1985.

[44] W. A. Johnson and D. G. Dudley, "Real axis integration of Sommerfeld integrals: Source and observation points in air," *Radio Sci.*, vol. 18, no. 02, pp. 175–186, March 1983.

[45] I. Lindell and E. Alanen, "Exact image theory for the Sommerfeld half-space problem, part II: Vertical electrical dipole," *IEEE Trans. Antennas Propag.*, vol. 32, no. 8, pp. 841–847, 1984.

[46] M. T. Silva, W. Huang, and E. W. Gill, "High-frequency radar cross section of the ocean surface with arbitrary roughness scales: A generalized functions approach," *IEEE Trans. Antennas Propag.*, vol. 69, no. 3, pp. 1643–1657, 2021.

[47] M. El-Shenawee, C. Rappaport, E. L. Miller, and M. B. Silevitch, "Three-dimensional subsurface analysis of electromagnetic scattering from penetra-

ble/PEC objects buried under rough surfaces: use of the steepest descent fast multipole method," *IEEE Trans. Geosci. Remote Sens*, vol. 39, no. 6, pp. 1174–1182, 2001.

[48] C. Kuo and M. Moghaddam, "Electromagnetic scattering from multilayer rough surfaces with arbitrary dielectric profiles for remote sensing of subsurface soil moisture," *IEEE Trans. Geosci. Remote Sens*, vol. 45, no. 2, pp. 349–366, 2007.

[49] J. Strutt, *The Theory of Sound*. Dover, New York, 1945, vol. 2.

[50] S. O. Rice, "Reflection of electromagnetic waves from slightly rough surfaces," *Commun. Pure Appl. Math.*, vol. 4, no. 2-3, pp. 351–378, 1951.

[51] J. R. Wait, "Perturbation analysis for reflection from two-dimensional periodic sea waves," *Radio Sci.*, vol. 6, no. 3, pp. 387–391, 1971.

[52] D. Barrick, "First-order theory and analysis of MF/HF/VHF scatter from the sea," *IEEE Trans. Antennas Propag.*, vol. 20, no. 1, pp. 2–10, 1972.

[53] A. Tabatabaeenejad and M. Moghaddam, "Study of validity region of small perturbation method for two-layer rough surfaces," *IEEE Geosci. Remote Sens. Lett.*, vol. 7, no. 2, pp. 319–323, 2010.

[54] H. Zamani, A. Tavakoli, and M. Dehmollaian, "Scattering from two rough surfaces with inhomogeneous dielectric profiles," *IEEE Trans. Antennas Propag.*, vol. 63, no. 12, pp. 5753–5766, 2015.

[55] J. Stratton, *Electromagnetic Theory*. McGraw-Hill, New York, 1941, vol. 2.

[56] P. Beckmann and A. Spizzichino, *The Scattering of Electromagnetic Waves from Rough Surfaces*. Artech House, Norwood, MA, 1987.

[57] R. Kodis, "A note on the theory of scattering from an irregular surface," *IEEE Trans. Antennas Propag.*, vol. 14, no. 1, pp. 77–82, 1966.

[58] D. Barrick, "Rough surface scattering based on the specular point theory," *IEEE Trans. Antennas Propag.*, vol. 16, no. 4, pp. 449–454, 1968.

[59] ——, "Wind dependence of quasi-specular microwave sea scatter," *IEEE Trans. Antennas Propag.*, vol. 22, no. 1, pp. 135–136, 1974.

[60] C. Bourlier, N. Pinel, and G. Kubické, *Method of Moments for 2D Scattering Problems: Basic Concepts and Applications*. John Wiley & Sons, Inc., USA, 2013.

[61] Z. Lai, J. Kiang, and R. Mittra, "A domain decomposition finite difference time domain (FDTD) method for scattering problem from very large rough surfaces," *IEEE Trans. Antennas Propag.*, vol. 63, no. 10, pp. 4468–4476, 2015.

[62] E. M. Nassar, J. T. Johnson, and R. Lee, "A numerical model for electromagnetic scattering from sea ice," *IEEE Trans. Geosci. Remote Sens*, vol. 38, no. 3, pp. 1309–1319, 2000.

[63] U. K. Khankhoje and S. Padhy, "Stochastic solutions to rough surface scattering using the finite element method," *IEEE Trans. Antennas Propag.*, vol. 65, no. 8, pp. 4170–4180, 2017.

[64] P. Liu and Y. Jin, "Numerical simulation of bistatic scattering from a target at low altitude above rough sea surface under an EM-wave incidence at low grazing angle by using the finite element method," *IEEE Trans. Antennas Propag.*, vol. 52, no. 5, pp. 1205–1210, 2004.

[65] J. Walsh, "On the theory of electromagnetic propagation across a rough surface and calculations in the VHF region," in *Department of National Defence, Government of Canada, St. John's, Newfoundland and Labrador, Tech. Rep.,*, 1980, pp. 159–160.

[66] J. Walsh and R. Donnelly, "Consolidated approach to two-body electromagnetic scattering," *Phys. Rev. A*, vol. 36, no. 9, p. 4474–4485, 1987.

[67] ——, "A general theory of the interaction of electromagnetic waves with isotropic, horizontally layered media1 (summary)," *Radio Sci.*, vol. 22, no. 4, pp. 545–547, 1987.

[68] J. Walsh and S. K. Srivastava, "Rough surface propagation and scatter 1. general formulation and solution for periodic surfaces," *Radio Sci.*, vol. 22, no. 02, pp. 193–208, 1987.

[69] J. Walsh and E. W. Gill, "An analysis of the scattering of high-frequency electromagnetic radiation from rough surfaces with application to pulse radar operating in backscatter mode," *Radio Sci.*, vol. 35, no. 6, pp. 1337–1359, 2000.

[70] M. T. Silva, W. Huang, and E. W. Gill, "High-frequency radar cross-section of the ocean surface with arbitrary roughness scales: Higher-order corrections and general form," *IEEE Trans. Antennas Propag.*, vol. 69, no. 10, pp. 6723–6738, 2021.

[71] M. Yuan and T. K. Sarkar, "Computation of the Sommerfeld integral tails using the matrix pencil method," *IEEE Trans. Antennas Propag.*, vol. 54, no. 4, pp. 1358–1362, April 2006.

[72] L. Tsang, J. A. Kong, and K. H. Ding, *Scattering of Electromagnetic Waves*. New York: John Wiley & Sons, Inc., 2001.

[73] J. Walsh and R. Donnelly, "Consolidated approach to two-body electromagnetic scattering," *Phys. Rev. A*, vol. 36, pp. 4474–4485, Nov 1987.

[74] B. Wu and L. Tsang, "Fast computation of layered medium green's functions of multilayers and lossy media using fast all-modes method and numerical modified steepest descent path method," *IEEE Trans. Microw. Theory Tech.*, vol. 56, no. 6, pp. 1446–1454, Jun. 2008.

[75] M. Abramowitz and I. A. Stegun, *Handbook of mathematical functions with formulas, graphs and mathematical tables*. New York: Wiley, 1972.

[76] A. Hochman and Y. Leviatan, "A numerical methodology for efficient evaluation of 2D Sommerfeld integrals in the dielectric half-space problem," *IEEE Trans. Antennas Propag.*, vol. 58, no. 2, pp. 413–431, Feb 2010.

[77] D. Barrick, "First-order theory and analysis of MF/HF/VHF scatter from the sea," *IEEE Trans. Antennas Propag.*, vol. 20, no. 1, pp. 2–10, 1972.

[78] J. Walsh, W. Huang, and E. Gill, "The first-order high frequency radar ocean surface cross section for an antenna on a floating platform," *IEEE Trans. Antennas Propag.*, vol. 58, no. 9, pp. 2994–3003, Sept 2010.

[79] W. Huang, S. Wu, E. Gill, B. Wen, and J. Hou, "HF radar wave and wind measurement over the eastern China sea," *IEEE Trans. Geosci. Remote Sens.*, vol. 40, no. 9, pp. 1950–1955, 2002.

[80] R. Golubovic, A. G. Polimeridis, and J. R. Mosig, "Efficient algorithms for computing Sommerfeld integral tails," *IEEE Trans. Antennas Propag.*, vol. 60, no. 5, pp. 2409–2417, May 2012.

[81] M. E. Nazari and W. Huang, "An analytical solution of the electric field radiated by a dipole over a layered half-space," in *2020 IEEE International Symposium on Antennas and Propagation and North American Radio Science Meeting*, 2020, pp. 943–944.

[82] M. E. Nazari, W. Huang, and Z. Alavizadeh, "Return loss-bandwidth evaluation

for electrically small microstrip antennas," *J. Electromagn. Waves Appl.*, vol. 34, no. 16, pp. 2220–2235, 2020.

[83] S. J. Radzevicius, C. Chen, L. Peters, and J. J. Daniels, "Near-field dipole radiation dynamics through FDTD modeling," *J. Appl. Phys.*, vol. 52, no. 2, pp. 75–91, 2003.

[84] N. N. Qaddoumi, W. M. Saleh, and M. Abou-Khousa, "Innovative near-field microwave nondestructive testing of corroded metallic structures utilizing open-ended rectangular waveguide probes," *IEEE Trans. Instrum. Meas*, vol. 56, no. 5, pp. 1961–1966, Oct 2007.

[85] A. T. Mobashsher, K. S. Bialkowski, and A. M. Abbosh, "Design of compact cross-fed three-dimensional slot-loaded antenna and its application in wideband head imaging system," *IEEE Antennas Wireless Propag. Lett.*, vol. 15, pp. 1856–1860, 2016.

[86] J. D. Cross and P. R. Atkins, "Electromagnetic propagation in four-layered media due to a vertical electric dipole: A clarification," *IEEE Trans. Antennas Propag.*, vol. 63, no. 2, pp. 866–870, Feb 2015.

[87] S. F. Mahmoud and Y. M. M. Antar, "High frequency ground wave propagation," *IEEE Trans. Antennas Propag.*, vol. 62, no. 11, pp. 5841–5846, Nov 2014.

[88] D. Hughes and R. Zoughi, "A novel method for determination of dielectric

properties of materials using a combined embedded modulated scattering and near-field microwave techniques-part ii: dielectric property recalculation," *IEEE Trans. Instrum. Meas.*, vol. 54, no. 6, pp. 2398–2401, 2005.

[89] A. I. Khuri, *Advanced Calculus with Applications in Statistics*. Wiley, New Jersy, 2003.

[90] W. H. Press, S. A. Teukolsky, W. T. Vetterling, and B. P. Flannery, *Numerical Recipes 3rd Edition: The Art of Scientific Computing*, 3rd ed. USA: Cambridge University Press, 2007.

[91] T. Meissner and F. J. Wentz, "The complex dielectric constant of pure and sea water from microwave satellite observations," *IEEE Trans. Geosci. Remote Sens.*, vol. 42, no. 9, pp. 1836–1849, 2004.

[92] R. Van Dam, "Calibration functions for estimating soil moisture from GPR dielectric constant measurements," *Commun. in Soil Sci. Plant Anal.*, vol. 45, 01 2014.

[93] M. C. Dobson, F. T. Ulaby, M. T. Hallikainen, and M. A. El-rayes, "Microwave dielectric behavior of wet soil-part ii: Dielectric mixing models," *IEEE Trans. Geosci. Remote Sens.*, vol. GE-23, no. 1, pp. 35–46, 1985.

[94] D. E. Barrick, "Theory of HF and VHF propagation across the rough sea, 2, application to HF and VHF propagation above the sea," *Radio Sci.*, vol. 6, no. 5, pp. 527–533, 1971.

[95] T. Kurner and A. Meier, "Prediction of outdoor and outdoor-to-indoor coverage in urban areas at 1.8 GHz," *IEEE J. Sel. Areas Commun.*, vol. 20, no. 3, pp. 496–506, April 2002.

[96] W. C. Barott and B. Himed, "Simulation model for wide-area multi-service passive radar coverage predictions," in *2013 IEEE Radar Conf.*, April 2013, pp. 1–4.

[97] X. Chen, W. Huang, C. Zhao, and Y. Tian, "Rain detection from X-band marine radar images: A support vector machine-based approach," *IEEE Trans. Geosci. Remote Sens.*, vol. 58, no. 3, pp. 2115–2123, 2020.

[98] K. A. Michalski and D. Jackson, "Equivalence of the King and Norton-Bannister theories of dipole radiation over ground with extensions to plasmonics," *IEEE Trans. Antennas Propag.*, vol. 64, no. 12, pp. 5251–5261, 12 2016.

[99] R. Somaraju and J. Trumpf, "Frequency, temperature and salinity variation of the permittivity of seawater," *IEEE Trans. Antennas Propag.*, vol. 54, no. 11, pp. 3441–3448, Nov 2006.

[100] D. Wobschall, "A theory of the complex dielectric permittivity of soil containing water: The semidisperse model," *IEEE Trans. Geosci. Electron.*, vol. 15, no. 1, pp. 49–58, Jan 1977.

[101] C. Geddes, *Reviews in Plasmonics 2016*. Switzerland: Springer, 01 2017, vol. 2016.

[102] L. Nickelson, *Electromagnetic Theory and Plasmonics for Engineers.* Springer, 01 2019.

[103] N. Pinel, C. Bastard, C. Bourlier, and M. Sun, "Asymptotic modeling of coherent scattering from random rough layers: Application to road survey by gpr at nadir," *Int. J. Antennas Propag.*, vol. 2012, pp. 1–9, 2012.

[104] J. Walsh, "Model developement for evaluation studies of ground wave radar," Center for Cold Ocean Resources Engineering (C-Core), Memorial Univeristy of Newfoundland, St. John's, Canada, Tech. Rep., 1990.

[105] ——, "Asymptotic expansion of a Sommerfeld integral," *Electron. Lett.*, vol. 20, no. 18, p. 746, 1984.

[106] M. E. Nazari and W. Huang, "Scattering of EM waves from random surfaces with different contrast and surface roughness," in *2021 International Applied Computational Electromagnetics Society Symposium (ACES), Online-Live*, 2021, pp. 1–3.

[107] M. Eslami Nazari and W. Huang, "EM wave scattering by random surfaces with different contrast and large roughness heights," *IEEE J. Multiscale Multiphys. Comput. Tech.*, vol. 7, pp. 252–267, 2022.

[108] A. Ishimaru, *Electromagnetic wave propagation, radiation, and scattering.* Wiley, New Jersey, USA, 2017.

[109] I. Bronshtein, K. Semendyayev, G. Musiol, and H. Muehlig, *Handbook of mathematics*. Springer, Berlin, 2005.

[110] G. B. Arfken, H. J. Weber, and F. E. Harris, *Mathematical Methods for Physicists: A Comprehensive Guide*. Elsevier Science, Oxford, UK, 2013.

[111] H. Ye and Y.-Q. Jin, "Parameterization of the tapered incident wave for numerical simulation of electromagnetic scattering from rough surface," *IEEE Trans. Antennas Propag.*, vol. 53, no. 3, pp. 1234–1237, 2005.

[112] J. T. Johnson, "Third-order small-perturbation method for scattering from dielectric rough surfaces," *J. Opt. Soc. Am. A*, vol. 16, no. 11, pp. 2720–2736, Nov 1999.

[113] C.-A. Guérin and M. Saillard, "On the high-frequency limit of the second-order small-slope approximation," *Waves Random Media*, vol. 13, pp. 75 – 88, 2003.

[114] C.-T. Tai, *General Vector and Dyadic Analysis: Applied Mathematics in Field Theory*. Wiley-IEEE Press, USA, 1997.

Appendix A

Approximation of I_6 Coefficients in (3.32)

An approximate solution for each coefficient in (3.32) is obtained using curve fitting, while the frequency changes between 10 MHz to 10 GHz. In other words, the proposed approximate solution is fitted to the numerical solution in the whole frequency range for a selected a value for finding each coefficient. This process is repeated for different z coordinates of the observation points and antenna heights corresponding to a values to find each coefficient. Finally, a approximate formulation for each coefficient is obtained using curve fitting in terms of a value as follows.

$$a_1 \simeq 11.5\sin(0.4\,a+3)+8.3\sin(0.4\,a-0.5)+0.7\sin(2.4\,a-0.6)$$

$$b_1 \simeq -0.97-0.03\cos(2\,a)-0.05\sin(2\,a)$$

$$c_1 \simeq 33.7\sin(0.5\,a+1.8)+0.9\sin(2\,a+0.8)+31\sin(0.6\,a-1.5)$$

$$
\begin{aligned}
a_2 \simeq & 37.7\sin(0.5\,a + 2.2) + 34.9\sin(0.5\,a - 1.1) + 1.1\sin(2.4\,a - 0.4) \\
b_2 \simeq & 2.7\sin(0.1\,a + 3.6) + 1.8\sin(0.2\,a + 0.1) \\
c_2 \simeq & 0.1 - 0.4\cos(1.2\,a) + 0.5\sin(1.2\,a) - 0.6\cos(2.4\,a) + 1.2\sin(2.4\,a) \\
a_3 \simeq & 7.9 + 7.7\sin(0.3\,a - 1.4) + 1.6\sin(2.5\,a + 0.6) \\
b_3 \simeq & 2.6\sin(0.1\,a + 3) + 0.9\sin(0.3\,a - 1.5) - 0.1\sin(0.9\,a - 1.6) \\
c_3 \simeq & -2.4 - 0.3\cos(0.5\,a) + 0.2\sin(0.5\,a) + 1.4\cos(a) - 2\sin(a) - \cos(1.5\,a) \\
& - 0.2\sin(1.5\,a) \\
a_4 \simeq & 121\sin(0.1\,a - 0.2) + 870.9\sin(0.01\,a - 3.2) + 1.5\sin(2.8\,a - 1.2),\ b_4 \simeq -1 \\
c_4 \simeq & 10^8\big[2.09 - 3.2\cos(0.06\,a) - 1.2\sin(0.06\,a) + 1.3\cos(0.12\,a) + 1.1\sin(0.12\,a) \\
& - 0.24\cos(0.18\,a) - 0.43\sin(0.18\,a) + 0.0097\cos(0.24\,a) + 0.062\sin(0.24\,a)\big]
\end{aligned}
\tag{A.1}
$$

As can be seen in (A.1), the sum of sinusoidal functions has been used for finding an approximate expression for each coefficient since it provides higher accuracy at various a values and frequencies.

Appendix B

Approximate Closed-form solution of I_3 in (5.56)

In this section, an approximate closed-form solution for the integral of I_3 in (5.56) obtained from (5.49) is proposed. By multiplying the Sommerfeld attenuation function $F(\rho)$ to $F_n(\rho)$ presented in (5.46), the integral of I_3 in (5.55) can be formed. To avoid confusion, the integral is split up into five additive terms and an approximate closed-form solution is obtained for each term. The first integral presented in (A.2) is calculated using the stationary phase integration method as

$$T_1' = \int_0^{\pi} \left(1 - e^{-jk(\eta_1 - 1)(1-\cos\delta)\rho/2}\right) d\delta \simeq \pi - \sqrt{\frac{\pi}{2C_1}} \left(e^{j\pi/4} - e^{-jk\rho(\eta_1 - 1)} e^{-j\pi/4}\right) \tag{A.2}$$

wherein $C_1 = -k(\eta_1 - 1)\rho/2$. T_2' is the next integral mentioned in (A.3). The stationary phase integration method is also used for the calculation of this integral.

Thus, we have

$$\begin{aligned} T_2' &= \frac{1}{\eta_1}\left[\int_0^{\pi} e^{-jk(\eta_1-1)\rho}d\delta - \int_0^{\pi} e^{-jk(\eta_1-1)(1+\cos\delta)\rho/2}d\delta\right] \\ &\simeq \frac{-1}{\eta_1^2}\sqrt{\frac{\pi}{2C_1}}\left(e^{-jk\rho(\eta_1-1)}e^{-j\pi/4}+e^{j\pi/4}\right)+\frac{\pi}{\eta_1^2}e^{-jk\rho(\eta_1-1)}. \end{aligned} \tag{A.3}$$

T_3', which contains the error function, can be calculated using the same procedure accomplished for T_2'. Thus, we have

$$\begin{aligned} T_3' &= j\sqrt{\frac{k\pi}{2n_p}}\int_0^{\pi}\sqrt{C_2}e^{kC_2(j-n_p)}\Big(\sqrt{1+n_p^2}\,\mathrm{erf}(\sqrt{C_3}) - \sqrt{\eta_1^2+n_p^2}\,\mathrm{erf}(\sqrt{C_4})\Big)d\delta \\ &\simeq \frac{j\pi}{2}\sqrt{\frac{k\rho}{n_pC_5}}e^{j(2C_5-\pi/4)}\left[\eta_1\,\mathrm{erf}\left(\sqrt{k\rho(j-n_p)}\right) - \eta_1\sqrt{2}\,\mathrm{erf}\left(\sqrt{k\rho(j\eta_1-n_p)}\right)\right] \end{aligned} \tag{A.4}$$

in which $C_2 = \rho(1-\cos\delta)/2$, $C_3 = k\rho(j-n_p)(1-\cos\delta)/2$, $C_4 = k\rho(j\eta_1-n_p)(1-\cos\delta)/2$ and $C_5 = k\rho(1+jn_p)/2$. The next integral is T_4', which can be expressed as

$$T_4' = j\sqrt{\frac{-jk\pi\rho}{2\eta_1\sqrt{1+\eta_1^2}}}e^{-jk\rho(\eta_1+n_u-2)/2}\int_0^{\pi}e^{jC_6\cos\delta}\cos\frac{\delta}{2}\left[\mathrm{erfc}(\sqrt{C_7}) - \mathrm{erfc}(\sqrt{C_8})\right]d\delta \tag{A.5}$$

wherein $C_6 = k\rho(\eta_1-n_u)/2$, $C_7 = jk\rho(1+\cos\delta)(1-n_u)/2$, $C_8 = jk\rho(1+\cos\delta)(\eta_1-n_u)/2$ and $n_u = \sqrt{\frac{\eta_1^2}{\eta_1^2+1}}$. In order to find an approximate closed-form solution for this integral, the stationary phase integration method along with an asymptotic expansion of the error function [75] is employed. It should be noted that the stationary phase integration method is not applicable for the calculation of the second part of the integral consisting $\mathrm{erfc}(\sqrt{C_8})$ since the error function has an impact on the stationary

phase part $C_6 \cos\delta$. By using the asymptotic expansion of the complementary error function for the second part and the stationary phase integration technique for the first part of the integral in (A.5), T_4' can be approximated as

$$T_4' \simeq j\sqrt{\frac{-jk\pi\rho}{2\eta_1\sqrt{1+\eta_1^2}}}e^{-jk\rho(\eta_1+n_u-2)/2}\left[\sqrt{\frac{\pi}{2C_6}}e^{j(C_6-\pi/4)}\left[\operatorname{erf}\left(e^{j\pi/4}\sqrt{2C_6}\right)\right.\right.$$
$$\left.\left. - \operatorname{erf}\left(\sqrt{2jC_9}\right)\right] - \frac{\pi e^{-jC_6}}{\sqrt{2j\pi C_6}}\right] \tag{A.6}$$

where $C_9 = k\rho(1-n_u)/2$. T_5' is the next integral that needs to be calculated. After doing some simplification, this integral can be represented as

$$T_5' = -j\sqrt{\frac{-jk\pi\rho}{2\eta_1\sqrt{1+\eta_1^2}}}\int_0^{\pi}\cos\frac{\delta}{2}\,e^{C_7}\operatorname{erfc}\left(\sqrt{C_7}\right). \tag{A.7}$$

To calculate this integral, the small and large argument approximations of the complementary error function are used. The stationary phase integration approach is not applicable for the calculation of T_5' since the complementary error function has an impact on the stationary phase part C_7. Therefore, the Taylor series is used for the small argument (i.e., less than one) approximation of the complementary error function while the asymptotic expansion is utilized when the argument is greater than one. By splitting the bound of the integral (A.7) at $\delta_0 = \cos^{-1}(1/|C_9| - 1)$ due to the criteria of the large and small argument approximation of the complementary error

function, T_5' can be approximated as

$$T_5' \simeq -j\sqrt{\frac{-jk\pi\rho}{2\eta_1\sqrt{1+\eta_1^2}}}\left(\frac{\delta_0}{\sqrt{j2\pi C_9}}+\sum_{i=1}^{4}N_i\right) \tag{A.8}$$

in which

$$\begin{aligned}
N_1 &= \sqrt{\frac{\pi}{2jC_9}}e^{2jC_9}\left[\operatorname{erf}\left(\sqrt{2jC_9}\right)-\operatorname{erf}\left(\sqrt{2jC_9}\sin\frac{\delta_0}{2}\right)\right]\\
N_2 &= \frac{-\sqrt{2}}{3\sqrt{\pi}}(jC_9)^{1.5}\left[3\pi-3\delta_0-(4+\cos\delta_0)\sin\delta_0\right]\\
N_3 &= \frac{-3(jC_9)^{2.5}}{\sqrt{\pi}}\left[\frac{\pi-\delta_0}{3.2}-\frac{\sin\delta_0}{2}+\frac{\sin^3\delta_0}{24}-\frac{\sin 2\delta_0}{10.7}\right]\\
N_4 &= -\sqrt{\frac{2jC_9}{\pi}}\left(\pi-\delta_0-\sin\delta_0\right).
\end{aligned} \tag{A.9}$$

Finally, I_3 is obtained by adding all the dominant terms as

$$I_3 = \frac{jk\sqrt{2\pi}e^{-j\pi/4}}{8\pi^2\sqrt{k\rho}}\sum_{i=1}^{5}T_i'. \tag{A.10}$$